# Numerical and experimental study of the electric arc and its interaction with the electrodes, including heating, melting and evaporation of the metal and its impact on the arc properties

Oswaldo Ojeda Mena

Université Fédérale
Toulouse Midi-Pyrénées

# THÈSE

## En vue de l'obtention du
## DOCTORAT DE L'UNIVERSITÉ DE TOULOUSE

**Délivré par l'Université Toulouse 3 - Paul Sabatier**

---

**Présentée et soutenue par**

**Oswaldo OJEDA MENA**

Le 23 novembre 2023

# Étude numérique et expérimentale de l'arc électrique et de son interaction avec les électrodes, y compris le chauffage, la fusion et l'évaporation du métal et son impact sur les propriétés de l'arc.

---

Ecole doctorale : **GEETS - Génie Electrique Electronique,Télécommunications et Santé : du système au nanosystème**

Spécialité : **Génie Electrique**

Unité de recherche :
**LAPLACE - Laboratoire PLAsma et Conversion d'Énergie**

Thèse dirigée par
**Yann CRESSAULT et Philippe TEULET**

Jury

**M. Jean-Marc BAUCHIRE,** Rapporteur
**Mme Margarita BAEVA,** Rapporteure
**M. Yann CRESSAULT,** Directeur de thèse
**M. Philippe TEULET,** Co-directeur de thèse
**M. Vandad ROHANI,** Président

**ABSTRACT**

The objective of this thesis is to deliver a numerical model which will consider the interaction between the arc and metallic parts within low voltage switching devices. The work is the result of a collaboration between Schneider Electric Industries SAS (France), the LAPLACE laboratory from the Paul Sabatier University (France), and the University of Madeira (Portugal).

Numerical simulations of low voltage switching devices have become increasingly available with the growth of computational processing power. They are used to describe the electric arc, that is formed after the contacts separate, and how it interacts with the surrounding elements inside the switching device. One of the aspects that requires especial consideration is the treatment of the near-electrode layers since they define the energy and current transfer between the arc and the electrodes. In particular, existing models describing the arc – cathode interaction have been adapted to the low-voltage switching applications, where the electrodes are made mostly of non-thermionic materials. As the arc interacts with the electrodes, it will cause heating, melting, and vaporization of the metal. The presence of metal vapors in the arc will affect its properties and global behavior in the device. The present work studies how the metal vaporization effects are included in the electric arc model. For this purpose, property databases for different air-metal mixtures are used, in addition to an ablation model to estimate the mass losses in the electrodes.

The models are applied in low voltage switching applications, such as the opening of contacts under an electric load, where the numerical results were compared to data obtained experimentally. The comparison shows good agreement of the arc voltage and arc current. High-speed images of the arc are also compared with the calculated temperature and metal distribution. Finally, a study of the impact of the electrode material on the numerical simulations was also performed.

**Keywords:** Electrode heating, electric arc, thermodynamic properties, thermal plasma, metal evaporation, MHD, numerical simulation.

**RESUME**

L'objectif de cette thèse est de fournir un modèle numérique qui prend en compte l'interaction entre l'arc et les parties métalliques à l'intérieur des dispositifs de coupure basse tension. Ce travail est le résultat d'une collaboration scientifique entre Schneider Electric Industries SAS (France), le laboratoire LAPLACE de l'Université Paul Sabatier (France) et l'Université de Madère (Portugal).

Les simulations numériques des dispositifs de coupure à basse tension sont devenues de plus en plus disponibles avec la croissance de la puissance de traitement informatique. Elles sont utilisées pour décrire l'arc électrique, qui se forme après la séparation des contacts, et comment il interagit avec les éléments environnants à l'intérieur du dispositif. L'un des aspects qui nécessite une considération particulière est le traitement des gaines proches des électrodes, car elles sont le siège le transfert d'énergie et de courant entre l'arc et les électrodes. En particulier, les modèles existants décrivant l'interaction arc-cathode ont été adaptés aux applications de coupure à basse tension, où les électrodes sont principalement constituées de matériaux non thermoïoniques. Lorsque l'arc interagit avec les électrodes, il provoque le chauffage, la fusion et la vaporisation du métal. La présence de vapeurs métalliques dans l'arc affecte ses propriétés et son comportement global dans le dispositif. Le présent travail porte donc notamment sur les effets de cette vaporisation de métal et son incorporation dans le modèle de l'arc électrique. À cette fin, des bases de données de propriétés pour différents mélanges air-métal sont utilisées, en plus d'un modèle d'ablation pour estimer les pertes de masse dans les électrodes.

Les modèles portent sur des applications de commutation à basse tension, telles que l'ouverture de contacts. Les résultats numériques ont été comparés aux données obtenues expérimentalement. La comparaison montre une bonne concordance de la tension et du courant de l'arc. Des images à haute vitesse de l'arc sont également comparées à la température et à la distribution du métal calculées. Enfin, une étude de l'impact du matériau des électrodes sur les simulations numériques a également été réalisée.

**Mots clés :** chauffage des électrodes, arc électrique, propriétés thermodynamiques plasma thermique, évaporation du metal, MHD, simulation numérique.

**TABLE OF CONTENTS**

## INTRODUCTION

The electric arc is a key element of the current interruption process in low voltage switching devices, such as circuit breakers and contactors. However, during the breaking operation the arc can caused severe damage to the electrodes, including surface changes, melting and metal vaporization. As most electrodes in low voltage devices are made of non-refractory metals with low boiling temperatures, metal vapors resulting from vaporization of the electrodes can affect the properties of the medium and therefore the behavior of the arc.

For those reasons, companies rely more and more on numerical models of the arc to describe its behavior and how it interacts with the surrounding elements inside the device. Usually arc models are based on a set of assumptions that allows to simplify the task, and in the case of industrial applications the LTE bulk assumption is a widely used approach.

The thesis main goal is focused on developing a simplified description of the arc-electrode interaction to be used in an LTE arc model for low voltage switching applications. The model therefore has to consider both the energy and current transfer between arc and the electrodes, and the effects of metal vaporization on the arc.

Initially, a chapter is dedicated to a general description of the electric arc and the characteristics that separate it from other electrical discharges. It is followed by a description of the several regions in which the arc can be divided: the arc column and the near-electrode regions. Then, some examples of electric arc applications are presented. Since the focus of this work is on low voltage switching applications, a brief presentation of these devices is given with especial emphasis of the role that the electric arc plays on the current interruption process, the consequences of the electric arc on the electrodes, and the interest of developing numerical models to simulate the arc in switching devices. The last part is devoted to the motivation behind this work.

The next chapter describes the modelling of the electric arc. It begins explaining the physical modelling of the arc versus black box models, and the different level of model complexity used to describe the different regions in the arc. Then, it presents the equations used to model the arc column under the magnetohydrodynamic approach, as well as the equations for the electrodes. A section is dedicated to the approach followed to couple the arc-column and the electrodes, both for the anode and the cathode. It concludes with a test case of a free-burning arc where a recently developed model for non-thermionic cathodes is implemented.

Chapter 3 describes the model used to include the ablation of the electrodes in the global arc model and its effects on the arc plasma properties. First, it presents the source terms necessary to include the electrode ablation in the governing equations. Next, it introduces the species transport equation and the combined diffusion coefficients, necessary to describe the metal vapors in the plasma gas. The equation used to estimate the amount of vaporized mass is also shown in his chapter. Finally, it discusses the impact of metal vapors on the plasma properties.

Another chapter is devoted to application cases on low voltage switching devices. The case of study corresponds to an arc after the separation of two contacts, which is typical of industrial contactors. An experimental study is performed on this configuration, and then it is modelled using the magnetohydrodynamic approach.

Finally, conclusions from this thesis are described in the last chapter, along with the perspectives for future work. A list of references used for the realization of this work is also given.

This work was done as an industrial collaboration between Schneider Electric (Eybens, France), LAPLACE Laboratory (Toulouse, France), and the University of Madeira (Portugal). The recent arc-electrode models and the free-burning arc case presented in Chapter 2 were implemented with the support of the University of Madeira. The thermodynamic properties, transport coefficients, and combined diffusion coefficients used were calculated by the ScIPRA team from LAPLACE. The electrode ablation model described in Chapter 3 was also developed in Laplace. Meanwhile, the experimental and numerical studies of the application case (Chapter 4) were performed in the Schneider Electric facilities in Eybens.

# CHAPTER 1. THE ELECTRIC ARC AND ITS APPLICATIONS

## 1.1. THE ELECTRIC ARC

An electric arc can be simply defined as a plasma channel between two electrical contacts that is formed after a gas discharge [1]. In this work the focus is on arcs where the plasma is on the thermal regime, although non-thermal arcs also exist, for example at low pressures ($p < 0.1\ atm$). In the thermal regime, the plasma in the arc is close to the local thermal equilibrium (LTE) state, which will be explained below. The electric arc is not the only type of electrical discharge, other discharges include corona discharge, glow discharge, and spark discharge. However, the electric arc is differentiated from other discharges by three main features [2]:

a. High current densities, which can reach values higher than $10^6$ A/m$^2$ compared to the characteristic values of 10 – 100 A/m$^2$ in other discharges, such as glow discharge.
b. A low cathode voltage drop ($U_c$). It is usually around 10 V in electric arcs against a much higher value in glow discharges ($U_c > 100\ V$), due to a more efficient mechanism of electron emission in the arcs.
c. High luminosity in the arc column, especially at high pressures ($p \geq 1\ atm$).

The ranges for other characteristic parameters of thermal arcs are presented in Table 1.

Table 1. Typical ranges of thermal arc parameters. Source: [3]

| Parameter | Range |
|---|---|
| Gas pressure | 0.1 – 100 atm |
| Arc current | 30 – 30000 A |
| Electron density | $10^{21}$ – $10^{25}$ 1/m$^3$ |
| Gas temperature | 11600 – 116000 K |
| Electron temperature | 11600 – 116000 K |

### 1.1.1. Regions of the electric arc

The spatial distribution of the electric potential in the electric arc shows a particular behavior: it presents strong potential gradients in the plasma very close to the electrodes, while potential changes in the rest of the arc are rather small. Based on this phenomenon, the plasma in the arc is usually divided in three main regions: the arc column, the near-cathode region, and the near-anode region [4]. This is illustrated in Figure 1.

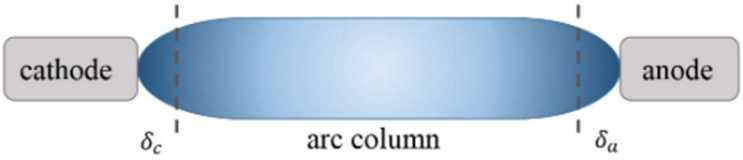


Figure 1. Schematic of the electric arc. Source: [5]

The total arc voltage in the electric arc ($U_{arc}$) is then the sum of the voltage drops in the arc column ($U_{column}$), and the near-electrodes regions ($U_{cath}$, $U_{anod}$):

$$U_{arc} = U_{cath} + U_{column} + U_{anod} \, . \tag{1}$$

***Arc column***

The arc column is the region that occupies most of the space between the electrodes, and it is much larger than both near-electrode regions. The length of the arc column will depend on the specific configuration, and it could vary as the arc moves or as the distance between electrodes changes (e.g., in the case of contact opening), but it is often in the order of $10^{-3}$ - $10^{-2}$ m. On the opposite side, the near-electrode regions have a length of ~ $10^{-4}$ m [5].

The potential gradient along the electric arc depends on the arc current, energy exchanges with the surroundings, the gas nature, pressure, among others. The cross section of the arc at a given point self-adjusts so the potential gradient required to drive the current is minimized [1], [2].

The column region in thermal arcs is considered to be close to the local thermal equilibrium (LTE), where the kinetic and chemical equilibrium are realized. The LTE exists when the following conditions are fulfilled in the plasma [6]:

a. The species that form the plasma have a Maxwellian velocity distribution.

b. The parameter $E/p$, that summarized the field strength and pressure requirements, is small and the temperature is high enough that the electron and heavy particle temperatures are equal ($T_e = T_h$).
c. Collisions are the dominant mechanisms for excitation and ionization.
d. Spatial variations of the plasma properties are small.
e. The quasi-neutrality condition is also satisfied in the arc column, meaning that negative and positive charges are in balance with each other.

It is important to note that the approximation of local thermal equilibrium is justified in the arc column where the plasma is dense, dominated by collisions, and with high temperatures. However, in other regions of the arc the plasma deviates from the local thermal equilibrium. This is especially true in the regions close to the electrodes and in the arc fringes.

***Near electrode regions***

The thin plasma regions that separate the arc column from the electrodes are called the near-electrode layers. As mentioned before, these regions are much smaller than the arc column, and they also present strong gradients of electrical potential and temperature. For example, typical values of the electric field in the cathode region are $10^8 - 10^9\ V/m$, while $10^7 - 10^8\ V/m$ in the anode region [7].

The presence of the electrodes causes perturbations in the plasma that lead to deviations from the local thermal equilibrium state. Three main perturbations occur in the near-electrode layers [5], [8], as illustrated in Figure 2.

a. Violation of the thermal equilibrium, where the temperature of electrons and heavy particles are different ($T_e \neq T_h$).
b. Violation of the ionization equilibrium, where the number density of charge particles is different to the number density predicted by the Saha equation ($n_e \neq n_{Saha}$)
c. Violation of the charge balance, where the number densities of positive and negative charges are not the same ($n_e \neq \sum Z n_i$).

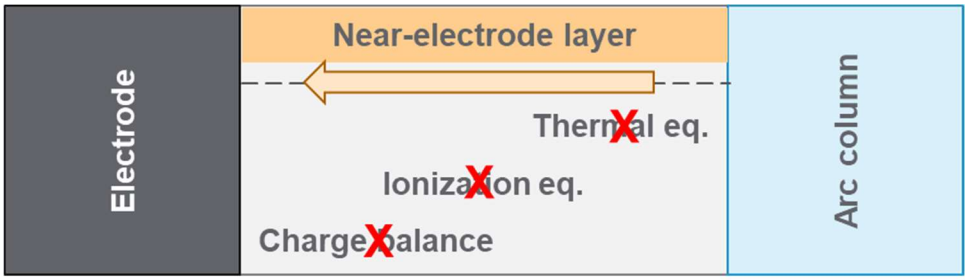


Figure 2. Schematic of the near-electrode layer.

As can be seen, the near-electrode regions are genuinely complex zones, with different physics taking place at different length scales. Moreover, the mechanisms present in the near-cathode layer and the near-anode layer are different and they must be described separately.

*The near-cathode region*

The main function of the cathode is to provide current-carrying electrons to the arc column [9]. The cathodes are usually divided in two categories depending on how they operate [10]: thermionic and non-thermionic cathodes.

The first category corresponds to thermionic cathodes, also called “hot cathodes” since the surface temperatures reach values higher than 3500 K. These are cathodes made of refractory metals with high boiling temperatures, such as tungsten, carbon, and molybdenum. They are typically found in discharge lamps and gas tungsten arc welding applications. The mechanism of current transfer is well known in this case, where the thermionic emitted electrons is dominant, and the current of ions coming from the plasma is small but non-negligible.

On the other side, non-thermionic or “cold cathodes” are made of materials with low boiling temperatures, e.g., silver, copper, and steel. Surface temperatures in this case do not usually exceed 3000 K. Examples of applications include low voltage switching devices and steelwork pieces operating as cathode in gas metal arc welding. Contrary to the thermionic case, the understanding of the current transfer mechanisms remains poor. Some of the proposed mechanisms are: thermos-field emission; explosive, evaporative and field emission; and electron emission due to excited atoms impacting the surface. Experimental studies have not been able to clarify the current transfer mechanisms in cold electrode, and it remains a subject of great interest and dispute. As an alternative, cold cathodes can be studied by means of numerical models based on first principles without any assumptions on the mechanisms of

current transfer. This was recently done in [10], where the ignition of an AC arc between cold electrodes was modelled using the unified modelling approach (explained in Chapter 2). This study showed that high ion currents (in the order of $10^7\ A/m^2$) can be reached in cold cathodes for high values of discharge gap width and/or secondary electron emission coefficients. This in turn requires high sheath voltage drops to provide enough energy for ionization. Moreover, the results indicated that the ignition of the arc with cold electrodes is initially led by displacement current, after which the ion current is dominant with the secondary electron emission playing an important role providing the ionization energy in the near-cathode region. Finally, the electron emission surpasses the ion current when the thermionic emission comes into play.

*Near-anode region*

According to [6], the anode plays a more passive role in the electric arc compared to the cathode. The main role of the near-anode layers is to electrically connect the high-temperature plasma in the arc column and the anode surface. It has been understood that the anode can operate in two regimes: passive and active [1]. In the passive mode, the anode only serves to collect the electrons from the arc column. When the anode is in the active mode, the anode material can vaporize and be ionized in the near-anode region to supply ions to the arc column.

Similarly, passive and active regimes were investigated by means of an unified modelling approach in [11] without considering metal vaporization. It was observed that at low and moderate surface temperatures the anode is in the passive regime, where the heating of the anode is mainly due to electron condensation. The contribution of the near-anode layer to the anode heating is then insignificant. An active anode regime was found for surface temperature higher than 3000 K when thermionic electron emission comes into play, which may occur in refractory anodes, for example in high-intensity discharge lamps. The thermionic emission does not seem to affect the current transfer to the anode, in fact most of the electrons return to the surface. Where the active regime has considerable effects is in the energy flux to the anode due to an increase of the electron density in the near-electrode layer. As the electron density increases, the electron thermal conductivity (and therefore the electron heat conduction transfer) will also increase, and a positive near-anode voltage is formed. This explains the increase of the heat flux to the anode. Because the thermionic electron emission depends on the surface temperature, an increase of the anode heating will further increase the effects of the active regime, creating a thermal instability with a positive feedback. This is illustrated in Figure 3:

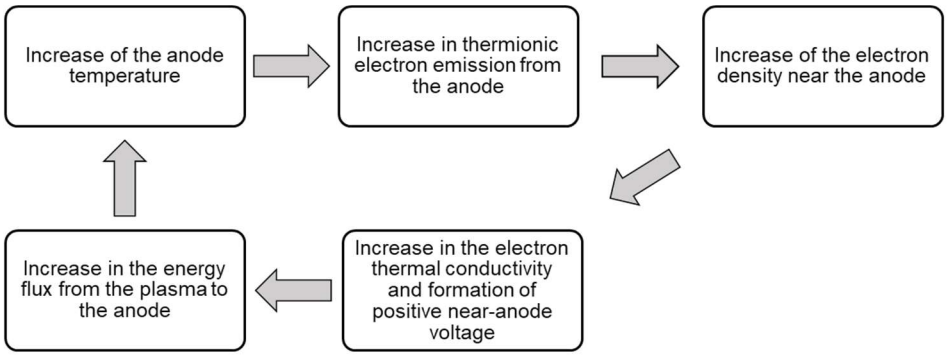


Figure 3. Thermal instability in the active anode regime. Adapted from [11].

### 1.1.2. Applications

The electric arc is present in a variety of industrial applications for a wide range of discharge powers and discharge pressures [12].

High intensity discharge (HID) lamps have been one of the main applications of electric arcs [5]. They are compact gas discharges that usually operate at pressures of 1 atm or higher and are more efficient and brighter than incandescent lamps. There exist three main types of HID lamps: high-pressure mercury, high-pressure sodium, and metal halide. Each of them consists of an inner arc tube containing the gas or vapor enclosed in an outer envelope [13]. The principal uses of HID lamps are the illumination of public places, projecting applications, car headlights, among others.

The electric arc is also used for thermal plasma processing applications. The main advantages of the thermal plasmas as a processing medium are the high energy densities and a controlled environment. Some examples of this application are: metal melting and remelting, plasma and in wire arc spraying, plasma synthesis of nanoparticles, and plasma waste treatment [14].

Electric arc furnace (EAF) is another application of electric arcs, they are widely use in steelmaking and smelting of nonferrous metals [15]. The energy is mainly supplied by electricity and turned into heat by the electric arc. The EAF represents one third of the crude steel produced worldwide, although it is also very energy-intensive accounting for 3% of the global electrical energy consumption in industry [16].

Common applications of electric arcs also include arc welding processes. They are used to join metal pieces and consist of an arc between two electrodes, one of which is the workpiece. The two main automated welding processes are gas-metal arc welding (GMAW)

and gas-tungsten arc welding (GTAW). In GMAW, the upper electrode is metal wire that acts as anode, while the workpiece is the cathode. The metal wire is melted, and the droplets fall to the weld pool. Therefore, the wire has to be fed continuously to maintain a constant arc length, For GTAW processes, the upper electrode is made of a refractory material that does not melt, usually tungsten. In this case, the workpiece is the anode, and the upper electrode is the cathode [17]. Some application fields of welding process include: construction of buildings, vehicles, ships, pipelines, and pressure vessels [18].

Finally, the electric arc is an essential element in switching applications. Low voltage switching devices, such as circuit breakers and contactors, are the main focus of the present work, they are described in the next section.

## 1.2. THE ARC IN LOW VOLTAGE SWITCHING DEVICES

Low voltage switching devices are electro-mechanical appliances used in electrical circuits up to 1000 V AC or 1500 V DC. There are two major categories of low voltage switching devices: contactors and circuit breakers. Their main functions are the making, carrying, and breaking of current under normal circuit conditions. They also must be capable to clear fault currents to protect both humans and equipment against prolonged overloads. Circuit breakers are additionally required to switch short-circuit currents [7], [19].

Contactors are remote controlled switches and are usually operated with a magnetic actuator. They have a long operational life that can go from a few thousand switching operations to over a million, depending on the electrical load. The contact materials vary according to the operation current: contactors with switching currents to 200 A use pure silver, silver-nickel compound, or silver with small alloying additions. For higher currents, silver-metal oxide materials have been the standard for several decades and are still the preferred choice.

As previously mentioned, circuit breakers have to perform their operations under normal and overload currents, but they must also be able to switch short-circuit currents on and off. The number of operations expected in circuit breakers is lower compared to that of contactors. In fact, they are only required to make and break the full short-circuit currents a few times, while the number of operations under normal loads is between 500 and 30000. AgC is often used as contact material due to its good anti-weld properties, although it may lead to long dwell times. This may be improved by using non-symmetrical configurations with other materials, such as AgNi, copper or WAg.

### 1.2.1. The electric arc and the current interruption process

The electric arc has the key role in the current interruption process in both contactors and circuit breakers [1]. When the contacts separate under a load current flowing, the arc is formed acting as a nonlinear resistor in the electric circuit. The arc will remain until it is extinguished, usually at the passing through the first current zero in an AC circuit. Once the arc extinguishes and does not reignite, the circuit is interrupted [7].

DC switching devices follow the same current interruption principle, although they need to develop their own current zero. This is achieved by increasing the arc voltage (by lengthening the arc or cooling it) to be at least equal to the system voltage.

A similar technique is used in AC switching devices when a limitation in the current is desired. This method allows one to reduce the magnitude and duration of the current during the breaking operation. After the contacts separate and the arc forms, the arc is forced into metal plates where it is stretched and cooled, resulting in a considerable increase in the arc voltage. Since this voltage is higher than the system voltage, the current decreases rapidly to zero, the arc extinguishes, and the current is interrupted. The design of the switching device is therefore utterly important to assure the arc motion into the chamber and the limitation effect of the metal plates.

### 1.2.2. Impact of the arc-electrode interaction on the devices

Although the arc is a necessary element to interrupt the current, it also has important consequences in low voltage switching devices.

A subject of great attention when designing circuit breakers and contactors is the erosion caused on the contacts by the electric arc. The erosion occurs when the arc remains stationary on the electrodes heating its surface to the boiling temperature of the contact material. Even if the arc moves on the electrode surface, the arc still melt the surface in contact with its roots. As described in [7], the erosion at each operation depends on several parameters, such as: the circuit current and its characteristics, the time the arc is present, the contact configuration (material, shape, size), the motion of the arc on the contacts, the device design, among others. The total mass loss in the contacts is then a combination of the metal evaporated from the roots, metal droplets ejected from the surface, metal vapor re-deposited back to the contacts, and metal that is deposited from the opposite contact. To illustrate the magnitude of the impact that the arc has on the contacts during the lifetime of a switching

devices, Figure 4 shows a comparison between a brand-new contact of a low-voltage contactor (a), and a similar contact that has performed tens of thousands of switching operations (b).

a) new contact | b) worn contact

Figure 4. Comparison between a new electrical contact and a worn one. Source: [20].

In addition to the strong gradients of potential and temperature that are found near the electrodes, the arc is also affected by vapors coming from the metal. This is especially true in circuit breakers under short-circuit condition, where the electrodes melt and vaporize due to the high currents carried in the devices. In general, the presence of vapors in the gas plasma has an impact on the thermophysical properties of the arc plasma. The main consequences are higher radiation losses leading to lower arc temperatures, and a decrease of the ionization temperatures that results in higher electrical conductivities at low temperatures. In a circuit breaker this translates into a longer time needed by the arc to transfer from the contacts to the runners, due to the higher density of metal vapors compared to air, and into a decrease of the total arc voltage caused by higher electrical conductivities [21]. Strong jets of metal vapor can appear when the vaporization of the electrodes occurs rapidly. In this case, the arc will follow the direction of the jets for a small distance and then it will bridge between the two jets to complete the current path [22].

### 1.2.3. Modelling of switching devices

Nowadays, the use of numerical models to simulate the arc in switching devices is of great interest in the industry, it allows the designers to better understand the current interruption process and gives valuable information to improve the performance of the devices [23]. In industrial applications, the arc is usually modelled as fluid following the magnetohydrodynamic (MHD) approach (detailed in Chapter 2) and solved using commercial or in-house computational fluid dynamic (CFD) packages. This is not an easy task since the problem has a strongly coupled multiphysics nature. Figure 5 describes the processes interacting with the arc column.

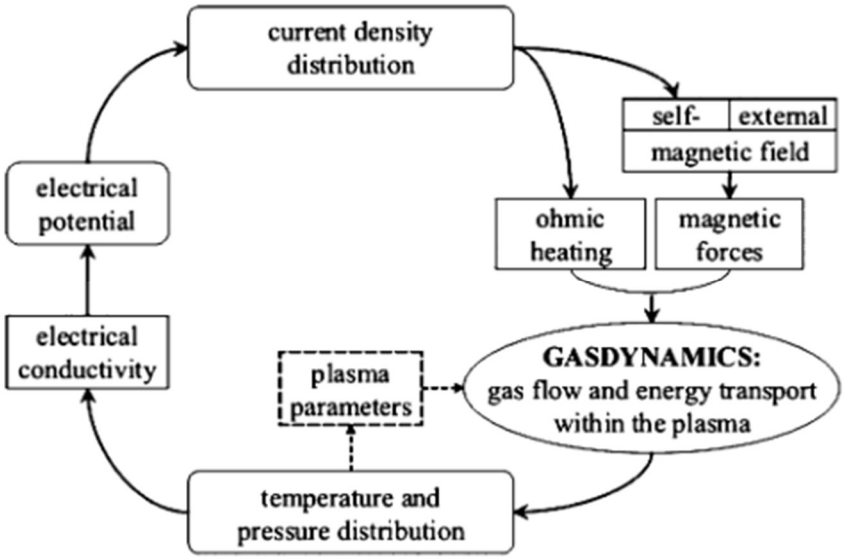


Figure 5. Interaction of processes in the arc column. Source: [24].

A typical simulation in low voltage switching devices implies a following the current interruption process from the arc ignition after the contact separation, to the commutation from the contacts to the arc runners, then the arc movement along the runners due to electromagnetic forces and pressure gradients, until it enters the arc chamber where the arc is split by multiple metal plates and eventually extinguishes [25].

Examples of these simulations can be found in the literature. In [26], a 3D simulation of a miniature circuit breaker was performed following the MHD approach, where phenomena such as arc root jumps, formation of arc roots at the splitting plates, or arc going across the splitter plates in the chamber were observed in the numerical results. Also [27] and [28] present results of switching device simulations to study the impact of the arc motion in a molded case circuit breaker, and out-gassing polymers in a miniature circuit breaker, respectively. Another

case is presented in [29], where the arc was studied in an industrial miniature circuit breaker from its ignition place to the extinguishing chamber.

## 1.3. MOTIVATION

As shown in the previous section, numerical simulations of low voltage switching devices have become increasingly available with the growth of computational processing power. Companies that work on the research and development of these devices rely more and more on numerical tools to better understand the phenomena involved, and to improve the design and performance of contactors and circuit breakers. By means of numerical models it is possible answer the most important question concerning switching devices: will the device interrupt the current as intended or not? Additionally, analysis can be performed to optimize its geometry, materials, costs, etc.

The goal of the numerical simulation is to describe the electric arc, that is formed after the contacts separate, and how it interacts with the surrounding elements inside the switching device. Since this modelling of the electric arc is a rather complex matter involving multiple physical phenomena in complicated 3D geometries, assumptions are often made to simplify the problem.

One of the aspects that requires particular consideration is the treatment of the near-electrode layers since they define the energy and current transfer between the arc and the electrodes. In fact, any accurate modelling of the arc must include a good description of the arc-electrode phenomena. As of this moment, numerous models have been proposed to describe the interactions between the arc and the electrodes, but there is not a universally accepted one. They mainly respond to the specific applications on which they are used.

The purpose of these work is firstly to develop a simplified description of the arc-electrode interaction to be used in the entire magnetohydrodynamic model of the arc. The treatment of the arc-electrode layers must be adapted to the case of low-voltage switching devices, where the electrodes are made mostly of non-thermionic materials. It must also account for the heating, melting and vaporization of the electrodes. As the presence of metal vapors in the arc will affect its properties and global behavior in the device, the present work also studies how the metal vaporization effects are included in the electric arc model.

The second goal of this thesis is to implement the arc-electrode description and the effects of metal vapors in an in-house magnetohydrodynamic model of the arc developed at Schneider Electric. As of the beginning of this work, the Schneider Electric code does not

include the effects of the arc on the electrodes, such as heating or ablation of the metal. Similarly, it only considers pure air as the plasma gas, with no account of the metal vapors that may be present in the medium. Once the code is improved with the work performed in this thesis, the Schneider Electric model of the arc should be able to better represent the phenomena present in their switching devices, and therefore, allow the designing team to improve the decision process during the development of their products.

## CHAPTER 2. MODELLING OF THE ELECTRIC ARC

### 2.1. INTRODUCTION

There are several approaches used to model the electric arc. They are classified in three categories: the black-box models, the parameter models, and the physical models [1].

The black box models are common in applications such as switchgear devices to study the interaction between the arc and the electric circuit [30], [31], [32]. In these models, mathematical expressions are used to relate the arc conductance with measurable parameters (e.g., arc voltage, arc current). Parameters models are variations of black box models where more complex functions and tables are used for the parameters in the black box models. Black box models includes the classical Cassie and Mayr models and some variations based on them, which are solutions of the general arc equation [1]:

$$\frac{d\ln(g)}{dt} = \frac{F'(Q)}{F(Q)}(P_{in} - P_{out}), \tag{2}$$

where $P_{in}$ is the power supplied to the plasma, $P_{out}$ is the power transported from the plasma, and $g$ is the momentary arc conductance:

$$g = F(Q) = F\left[\int_0^t (P_{in} - P_{out})dt\right]. \tag{3}$$

On the other side, physical models seek to represent in detail the physical processes that are present in the arc. The fluid approach is a common method to model the arc by considering fluid dynamics equations, thermodynamics laws and Maxwell's equations. They take into account the chemical reactivity of the arc plasma, the electromagnetic forces, resistive heat dissipations, radiation losses, and thermodynamic equations of state for each plasma component. The advantage of using fluid models is that they describe the macroscopic behavior of the plasma instead of following each individual species.

A key aspect of the arc modelling is the correct description of the plasma in the vicinity of the electrodes since it defines the energy and current transfer between the plasma and the electrodes [5]. However, implementing realistic models of the plasma-electrode interaction is not an easy task. As discussed in [33], even though numerous publications work on the treatment of the physical mechanism of current transfer to the electrodes to obtain feasible

numerical models, there is not a universally accepted model. This can be attributed to two main reasons: the physics describing the phenomena in the near-electrode layers is more complex than that of the arc column, and secondly, arbitrary descriptions that correlate with experiments are sometimes preferred over physical ones in application fields.

Several approaches exist to model the interaction between the arc and the electrodes, varying greatly on their complexity level. Table 2 contains a summary of these approaches from the complex unified modelling to the simpler LTE bulk plasma.

Table 2.Summary of the different approaches to model high-pressure arc discharges and their interaction with solid surfaces. Source: [33].

| **Approach** | **Approximations and/or effects accounted for in the arc bulk** | **Boundary conditions at the arc-solid interfaces describe** | **Complexity** |
|---|---|---|---|
| Unified modelling | $n_e \neq n_i$<br>$n_e \neq n_S$<br>$T_e \neq T_h$ | Contact with the solid | Very difficult |
| Quasi-neutral description of the arc bulk plasma | $n_e = n_i$<br>$n_e \neq n_S$<br>$T_e \neq T_h$ | Separation of charges | Difficult |
| Two temperatures description of the arc bulk plasma | $n_e = n_i$<br>$n_e = n_S$<br>$T_e \neq T_h$ | Separation of charges<br>Ionization non-equilibrium | Moderately difficult |
| LTE description of the arc bulk plasma | $n_e = n_i$<br>$n_e = n_S$<br>$T_e = T_h$ | Separation of charges<br>Ionization non-equilibrium<br>Thermal non-equilibrium | Reasonably straightforward |

Where $n_e$ and $n_i$ are the number densities of electrons and ions, respectively. $T_e$ is the temperature of electrons, and $T_h$ the temperature of the heavy particles (ions and neutrals, i.e., $T_h = T_i = T_a$). $n_S$ is the total number density calculated with the Saha equation.

The unified modelling is the most general and complex of the approaches presented in Table 2, since it models all the interelectrode gap up to the electrode surfaces. It consists of a set of equations including the conservation and transport equations for each plasma species, energy equations for electrons and heavy particles, and the Poisson equation. Its main advantage lies in the fact that no assumptions are made as to what mechanisms dominate in the different regions, i.e., the plasma in the arc column and the near-electrode layers are modelled with the same set of equations. Therefore, the information obtained with this kind of modeling allows to clarify the mechanism of current transfer in the discharge. On the downside, its complexity makes the unified modelling extremely demanding from the computational point of view and its applications is mostly limited to one-dimensional and low-current two-dimensional configurations [10].

In the simplest approach, the LTE or magnetohydrodynamic description, the arc bulk is assumed to be in the state of local thermal equilibrium, and it is separated from the near-electrode layers. In fact, only the arc column and the electrodes are modelled, while the phenomena taking place between these regions are introduced as appropriate conditions for the energy and current transfer in the electrodes and the arc column. This is the approach followed in this work given its accessible complexity, reasonable computational requirements, and calculation times; all of which makes the LTE approach suitable for industrial applications.

In this chapter, the general considerations of the modelling of the electric arc and its interaction with the electrodes are presented. The chapter describes the set of equations used to model the electric arc column under the magnetohydrodynamic approach, the electrodes, as well as the treatment of the near-electrode layers. Also, a classic test case of a free-burning arc is presented, where a novel arc-electrode model is implemented in initial cold electrodes, to study how the arc characteristics evolve as the electrodes heat.

## 2.2. MATHEMATICAL MODEL

### 2.2.1. The arc column

The plasma in the arc column is described following a fluid approach. The equations to solve correspond to the magnetohydrodynamics set of equations, which include the classic fluid dynamics equations (mass conservation, momentum conservation), the energy conservation equation, and the electromagnetic equations (current conservation, magnetic field).

For simplification purposes, some assumptions are made:

- the plasma in the arc column is assumed to be in a local thermal equilibrium state;
- gravity effects are neglected;
- the plasma is considered as a Newtonian fluid;
- the flow regime is laminar.

***Mass conservation equation***

The equation for mass conservation is given by:

$$\frac{\partial \rho}{\partial t} + \nabla \cdot (\rho \vec{v}) = S_m \,, \tag{4}$$

where $\rho$ is the plasma mass density and $\vec{v}$ is the average plasma velocity. The term on the right-hand side ($S_m$) corresponds to the mass injection into the plasma, for example due to vaporization of the electrode material. This is further explained in Chapter 3.

***Momentum conservation equation***

The conservation of momentum is described by equation (5):

$$\frac{\partial}{\partial t}(\rho \vec{v}) + \nabla \cdot (\rho \vec{v}\vec{v}) = -\nabla p + \nabla \cdot (\bar{\bar{\tau}}) + \vec{F} \,, \tag{5}$$

where $p$ is the plasma pressure. $\vec{F}$ are the external body forces acting on the fluid and include the Lorentz forces ($\overrightarrow{F_L}$):

$$\overrightarrow{F_L} = \vec{j} \times \vec{B} \,, \tag{6}$$

with $\vec{j}$ representing the current density and $\vec{B}$ the magnetic field. The term $\bar{\bar{\tau}}$ in equation (5) is the stress tensor:

$$\bar{\bar{t}} = \mu \left[ (\nabla \vec{v} + \nabla \vec{v}^T) - \frac{2}{3} \nabla \cdot \vec{v} I \right] , \tag{7}$$

where $\mu$ is the plasma viscosity and $I$ is the unit tensor.

***Energy equation***

The energy equation to be solved in the arc column, from which the temperature is obtained, can be expressed as:

$$\frac{\partial}{\partial t}\left(\rho\left(e_{int}+\frac{v^2}{2}\right)\right)+\nabla\cdot\left(\rho\vec{v}\left(h_T+\frac{v^2}{2}\right)\right)=\nabla\cdot\left(\lambda_T\nabla T-\sum_{j=1}^{N}h_{T\,j}\overrightarrow{J_j}+\bar{\bar{\tau}}\cdot\vec{v}\right)+S_h\,, \qquad (8)$$

where $e_{int}$ represents the fluid internal energy, $\lambda_T$ is the thermal conductivity and $h_T$ is the plasma enthalpy. The internal energy and the enthalpy are related by:

$$e_{int}=h_T-\frac{p}{\rho}\,.$$

The term $S_h$ contains the different source terms in the energy equation. In the modeling of electric arcs, this includes the heating due to Joule's effect, radiation losses, and the enthalpy transported to the plasma by the metal vaporized from the electrode surface.

The Joule heating ($S_{jou}$) is calculated with equation (9), where $\sigma$ is the electrical conductivity.

$$S_{jou}=\frac{1}{\sigma}|\vec{j}|^2\,. \qquad (9)$$

Other terms that are commonly added as source terms in the energy equation are the enthalpy transport due to electrons and the effects of the thermal diffusion ratio ($S_e$):

$$S_e=\nabla\cdot\left(\left(\frac{5}{2}+k_T\right)\frac{k_BT}{e}\vec{j}\right)\,, \qquad (10)$$

where $k_T$ is the so-called thermal diffusion ratio, $k_B$ is the Boltzmann constant, and $e$ is the elementary charge.

Regarding the radiation losses ($S_{rad}$), there exists several approaches to include them in the energy equation. In general, the modeling of the radiation is governed by the radiative transfer equation, which is a balance of the radiative energy. In an absorbing, emitting and scattering medium at position $\vec{r}$ and direction $\vec{s}$, it can be written as [34]:

$$\frac{d}{ds}I(\vec{r},\vec{s}) + (a+\sigma_s)I(\vec{r},\vec{s}) = an^2\frac{\sigma_{SB}T^4}{\pi} + \frac{\sigma_s}{4\pi}\int_0^{4\pi} I(\vec{r},\vec{s}')\,\Phi(\vec{s}\cdot\vec{s}')d\Omega' \,, \qquad (11)$$

where $a$ is the absorption coefficient, $n$ is the refractive index, $\sigma_s$ is the scattering coefficient, and $\sigma_{SB}$ is the Stefan-Boltzmann constant. $I$ represents the radiation intensity, $s$ is path length, $\vec{s}'$ is the scattering direction vector, $\Phi$ is the phase function, $\Omega'$ is the solid angle, and $T$ is the local temperature.

Equation $(11)$ can be simplified for the case of a linear light beam traveling through a non-scattering plasma with a refractive index equal to 1 [35]:

$$\frac{d}{dr}I_v(\vec{r},\vec{s}) = a_v\big(B_v - I_v(\vec{r},\vec{s})\big) \,, \qquad (12)$$

Where $I_v$, $a_v$, and $B_v$ are the radiation intensity, absorption coefficient, and black body radiation respectively, each of these quantities are local functions of the frequency (or wavelength). As explained by [36], the use of the apparently simple equation $(12)$ to calculate total radiation transfer can be complicated. It is due to the three-dimensional nature of radiation, and the fact that the radiative intensity and its divergence vary rapidly with the frequency. Therefore, geometrical simplifications (NEC), spectral simplifications (e.g. use of mean absorption coefficients), and radiative models are needed to model the radiation transfer in plasmas [36].

The most commonly used model for radiation treatment in plasma modeling are the discrete ordinates method, the P-1 method, and the net emission coefficient method.

*Discrete ordinates method*

The discrete ordinates method is a tool that allows to transform the radiative transfer equation into a set of transport equations. It discretizes the entire solid angle into a number of discrete solid angles elements and then solves a transport equation for each of these discrete angles. The integrals over solid angle are obtained by numerical quadrature [35]. Among its advantages are the capability to be used over the entire range of optical thickness, semi-transparent walls, surface-to-surface radiation, and participating medium radiation [34]. However, in comparison with the other methods, the discrete ordinate is associated with higher computational requirements [37].

*P-1 method*

Another model used to treat radiation in plasmas is the P-1 method. As the discrete ordinate method, the P-1 approach consists of the transformation of the radiative transfer equation into a set of relatively simple partial differential equations. This model is based on the expansion of the radiation intensity into an orthogonal series of first-order spherical harmonics (P-N -> P-1). Since the P-1 model discretize the radiative transfer equation into a diffusion equation, it is easy to solve with low computational demand. A disadvantage of this model is that there may be a loss of accuracy if the optical thickness is small [34].

*Net emission coefficient method*

The third approach is the net emission coefficient method, it is the simplest model since the radiative transfer equation is not solved. This model is based on the calculation of the difference between the emission and the absorption in the center of an isothermal and homogeneous sphere [36]. It is determined according to:

$$\epsilon_N = \int_0^\infty a_v B_v \, e^{-a_v R_p} \, d_v \,, \tag{13}$$

where $a_v$ is the spectral absorption coefficient, $\epsilon_N$ is the net emission coefficient expressed in W/m$^3$/sr, $R_p$ is the radius of the isothermal sphere, and $v$ is the frequency. For the conditions found in low voltage switching applications, a typical choice of $R_p$ is 1 mm.

Higher values of $R_p$ will not be likely to change the radiation losses, since most of the radiation reabsorption occurs in the first millimeter. Once the net emission coefficient is known, it can be directly used to calculate the radiation losses:

$$S_{rad} = -4\pi\epsilon_N \,. \tag{14}$$

As explained in [5], the use of net emission coefficients to treat the radiation losses has its disadvantages: the model gives accurate results in the region where the plasma temperature is high, but it does not take into account the reabsorption in the arc fringes where the temperature is lower. Similarly, it does not allow to estimate the radiation losses leaving the plasma.

Despites its limitations, the net emission coefficient method is the approach used to model the radiation losses in this work, since it is widely used in electric arc simulations, it is easy to implement, and the data is readily available in the literature for different gas mixtures and operating conditions. Similarly, the interest of this work in on the arc at high temperatures, where the net emission coefficient method is known to be fairly accurate.

***Current continuity equation***

If one assumes that the plasma is a highly conductive fluid, where there is not accumulation of space charges in the fluid and the main contributor to the electric current is conduction due to electric field [6, 7]; then, it is possible to express the current density as:

$$\vec{j} = \sigma\vec{E} \,, \tag{15}$$

where $\vec{E}$ is the electric field, and the current continuity equation in the plasma as:

$$\nabla \cdot \vec{j} = 0 \,. \tag{16}$$

***Maxwell's equations***

The magnetic field is calculated based on Maxwell's equation without eddy or displacement currents [5]:

$$\nabla \times \vec{B} = \mu_0 \vec{j}\,, \tag{17}$$

$$\nabla \times \vec{E} = 0\,, \tag{18}$$

$$\nabla \cdot \vec{B} = 0\,, \tag{19}$$

where $\vec{B}$ is the magnetic field, and $\mu_0$ is the vacuum permeability. To solve Maxwell's equations, it is common to use the vector potential approach:

$$\vec{B} = \nabla \times \vec{A}\,, \tag{20}$$

which relates the magnetic field $\vec{B}$ to a potential vector $\vec{A}$. Another method consists of calculating the magnetic field using the Biot-Savart law:

$$\vec{B} = \frac{\mu_0}{4\pi} \iiint_V \frac{(\vec{j}\, dV) \times \vec{r}'}{|\vec{r}'|^3}\,, \tag{21}$$

where $V$ is the volume, and $\vec{r}'$ is the distance vector to the observation point. The advantage of the using Biot-Savart law over vector potential is that it can be used in complicated geometries, although it comes with a higher computation time [23]. Therefore, in this work the potential vector method is used due to relatively simple axisymmetric geometries, in more complicated three-dimensional geometries the magnetic field should be calculated using the Biot-Savart law.

***Thermodynamic properties and transport coefficients***

In order to solve the equations governing the electric arc in the column, one must first know the thermodynamic properties and the transport coefficients in the plasma gas and how they vary with the operating conditions. The properties needed include the gas density, specific heat, thermal conductivity, electrical conductivity, viscosity, radiation losses, among others. Details of how theses quantities are calculated can be found in [39] and [40] for argon, and in [41] for air.

An example of the density for two different gases at one bar and how they vary with temperature is shown in Figure 6. Both argon and air mass densities show a similar behavior for the temperature range plotted, although argon density is slightly higher than air.

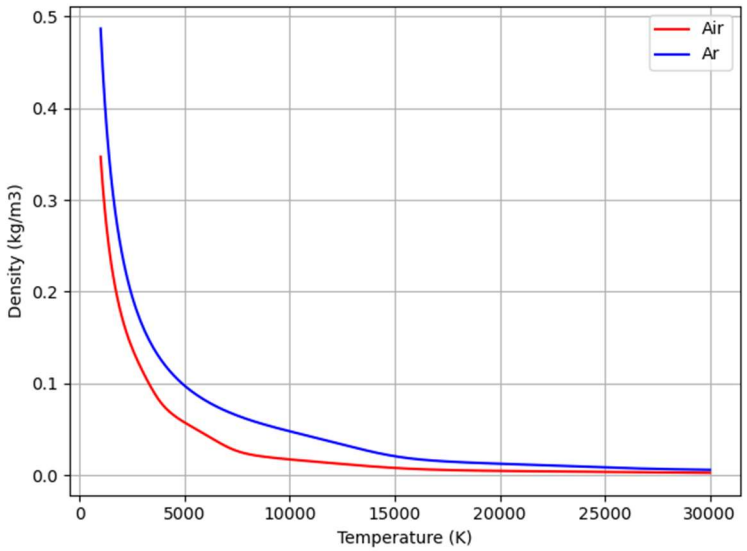


Figure 6. Mass density of air and argon at 1 bar.

The nature of the gases can have great impact on some of the properties, for instance the specific heat at constant pressure and thermal conductivity as seen in Figure 7 and Figure 8, respectively. The differences between air and argon are more evident in these cases: not only the specific heat and the thermal conductivity are higher in air compared to argon in most of the temperature range plotted, but also differences in the behavior of the properties are noticed at low temperatures. Below 10000 K, two peaks can be seen in air due to molecular dissociation ($O_2$, $N_2$) that are not present in argon. The peak observed at 15000 K in both air and argon corresponds to the first ionization. It occurs at almost the same temperature since the ionization energy of Ar (15.76 eV) is not so different to those of N (14.53 eV) and O (13.62 eV). For higher temperatures, the peaks are related to the successive ionizations.

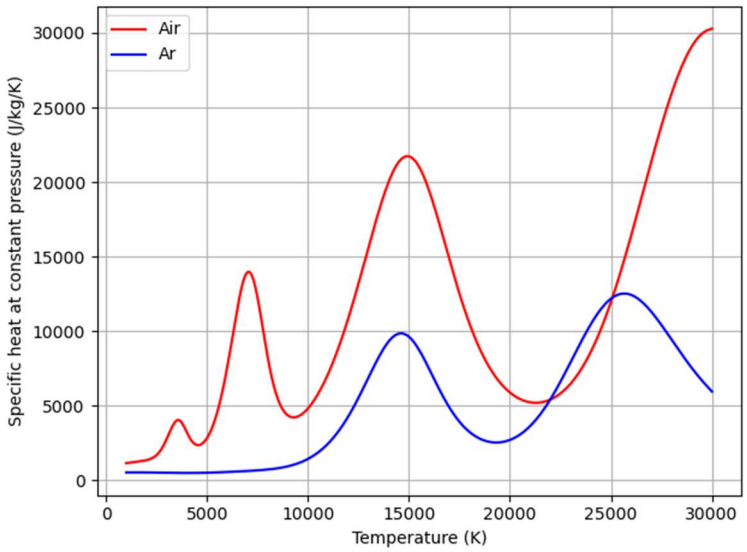


Figure 7. Specific heat at constant pressure of air and argon at 1 bar.

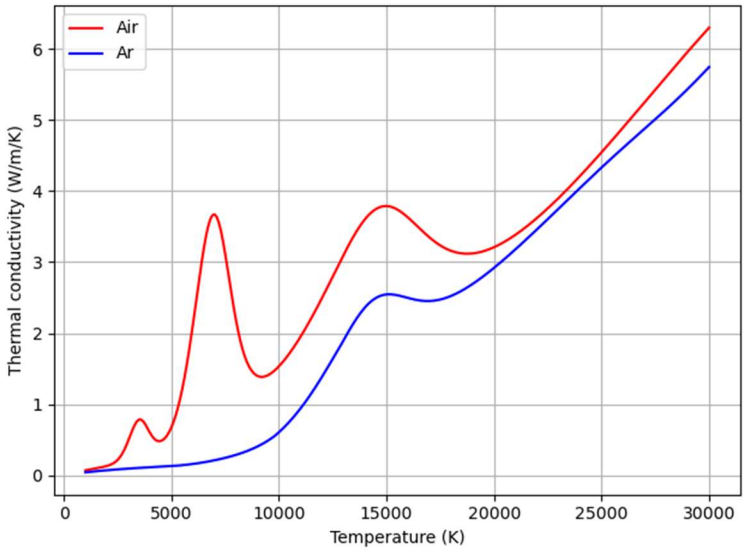


Figure 8. Thermal conductivity of air and argon at 1 bar.

This work uses the plasma thermodynamic properties and transport coefficients calculated according to the references previously mentioned, for a wide range of pressures (0.1 bar – 16 bar) and temperatures (300 – 30000 K).

### 2.2.2. The electrodes

In the solid volumes corresponding to the electrodes the energy equation and the current continuity equations are solved.

#### *Energy equation*

For a solid, the energy equation can be written as:

$$\frac{\partial}{\partial t}(\rho h_T) = \nabla \cdot (\lambda_T \nabla T) + S_h \,, \tag{22}$$

where $\rho$, $h_T$, and $\lambda_T$ correspond to the density, sensible enthalpy, and thermal conductivity of the metal material. $S_h$ includes the source terms such as the Joule heating.

#### *Current continuity equation*

The current continuity equation in the electrodes is the same as that of the arc column (equation $(16)$):

$$\nabla \cdot \vec{j} = 0 \,.$$

#### *Thermodynamics properties and transport coefficients*

Similar to the plasma in the air column, it is necessary to know how the metal properties vary with the operating conditions of the electrodes. This work considers pure metal such as tungsten, copper, or silver as electrode materials. Properties for tungsten are obtained from [42], which proposes analytical expressions for both solid and liquid phases. For copper and silver, the properties were retrieved from the Ansys Granta Selector software [43].

To illustrate the temperature dependency of the metal properties, the curves for copper, silver, and tungsten up to their boiling temperature are shown below:

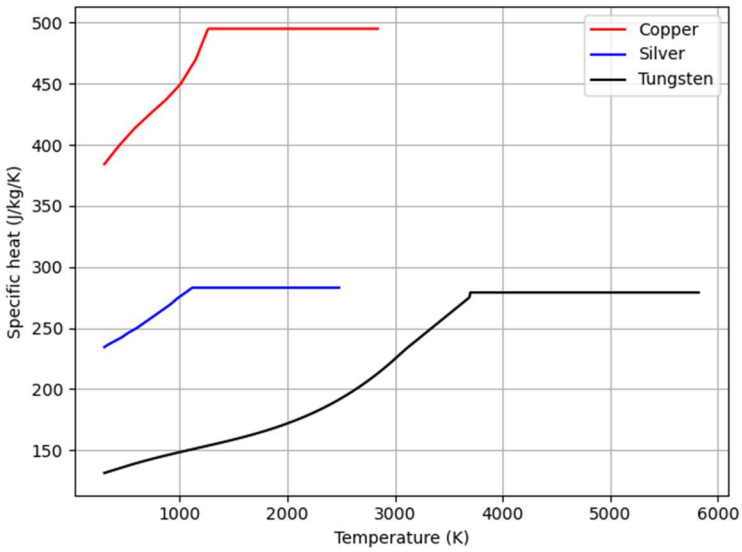


Figure 9. Specific heat of solid/liquid metals.

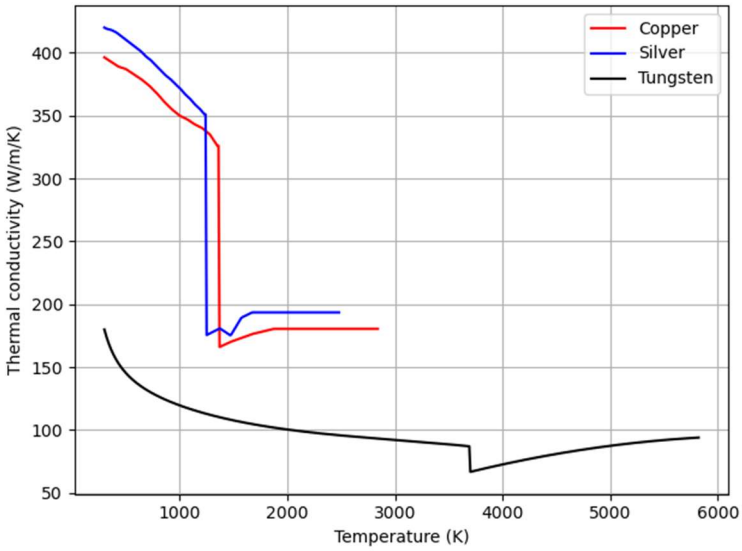


Figure 10. Thermal conductivity of solid/liquid metals.

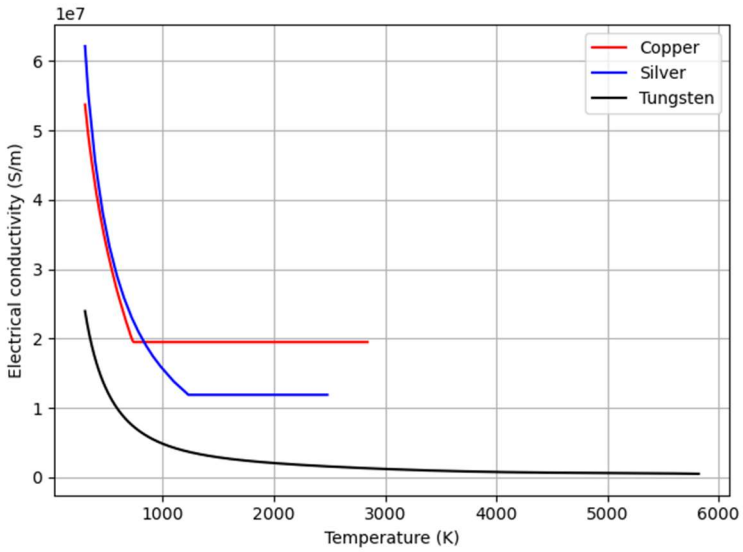


Figure 11. Electrical conductivity of solid/liquid metals.

Based on the data presented, one can see in Figure 9 to Figure 11 how the solid properties are affected by temperature, as well as discontinuities at the melting temperature (for copper it is 1356 K at 1 atm) in the curves due to the change of phase.

Another aspect to consider when modeling solid regions is the effects of the latent heat of fusion during melting / solidification. According to [44], in pure substances one can approximate the latent heat effect by a large increase in the specific heat for a small temperature range. This is done by calculating an equivalent specific heat $C_{p_{eq}}$, as in [45]:

$$C_{p_{eq}} = C_p + \frac{L_m}{\sqrt{\pi \Delta T^2}} e^{\frac{-(T-T_m)^2}{\Delta T^2}}, \tag{23}$$

where $L_m$ is the metal latent heat of fusion, $T_m$ is the melting temperature, and $\Delta T$ is the temperature interval.

### 2.2.3. The near-electrode layers

In order to make the coupling between the arc column and the electrodes, this work follows the approach proposed in [5], [46]. Accordingly, the near-electrode layers are treated as a zero-dimensional interface that contains the non-LTE regions of the plasma, that is, the

space-charge layer, the ionization layer, and the thermal non-equilibrium layers. Figure 12 illustrate the simplification of the near-electrode layer with the different non-equilibrium layers to the zero-dimensional interface used in this work.

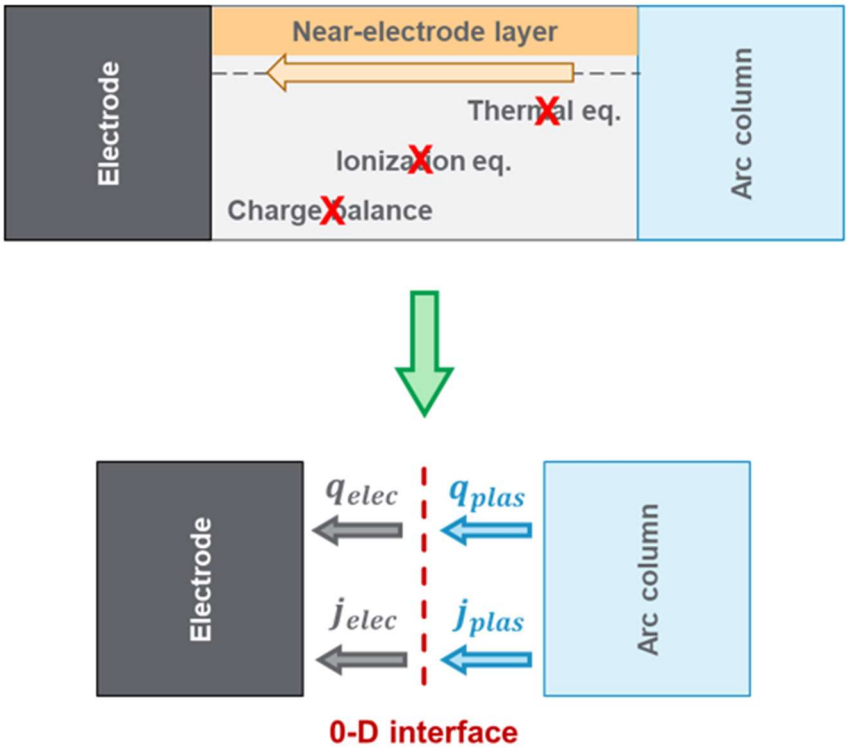


Figure 12. Treatment of the near-electrode layers.

This approach leads to discontinuities in the temperature and electrical potential between the arc column and the electrode, although the current density is assumed constant in the near-electrode layer. Thus, the current continuity condition is imposed at plasma-electrode interface:

$$j_w = j_{elec} = j_{plas}\,, \tag{24}$$

where $j_w$ is the current density crossing the interface. $j_{elec}$ and $j_{plas}$ are the current densities at the electrode and plasma boundaries, respectively.

The energy coupling is done by means of an energy balance in the near-electrode layer. The transfer of energy between the electrode and the arc column is defined by:

$$q_{elec} - q_{plas} = j_w\, U_d - j_w \frac{A_f}{e}\,, \tag{25}$$

where $q_{elec}$ is the energy flux directed from the near-electrode layer to the electrode, $q_{plas}$ is the heat flux from the arc column to the near-electrode layer, $U_d$ is the voltage drop in the near-electrode layer, and $A_f$ is the work function of the electrode material. The first term in the right-hand side represents the electrical power deposited in the near-electrode layer per unit area, and the second term is related to the energy required to extract electrons from the cathode surface. It is important to note that the sign of $j_w$ in equation $(25)$ corresponds to the situation illustrate in Figure 12, that is, the electrode is acting as cathode. If the electrode is anode, then the current density in the interface ($j_w$) changes sign. In this case, the second term in equation $(25)$ represents the energy release due to electrons condensing at the anode surface [46].

The advantage of using the zero-dimensional interface is that it avoids strong temperature gradients between the arc column and the electrodes [5]. Such gradients could potentially lead to problems of convergence during the calculations due to the great difference in the electrical conductivity of metals and cold plasma gas. In that case, a special treatment at the cells adjacent to the plasma-electrode interface is necessary, such as imposing artificially high electrical conductivities in the cold plasma or increasing the mesh size close to the electrodes.

The following sections describe how the different terms in equation $(25)$ are calculated in the near-cathode and the near-anode regions.

***Near-cathode region***

The heat flux to the cathode from the near-electrode layer ($q_{elec} = q_{cath}$) can be expressed as:

$$\begin{aligned} q_{cath} = j_{i,G}\left(U_c + E_{i,G} - \frac{A_f}{e} + \frac{5}{2}\frac{k_B T_e}{e} - \frac{2\,k_B T_w}{e}\right) + j_{i,M}\left(U_c + E_{i,M} - \frac{A_f}{e} + \frac{5}{2}\frac{k_B T_e}{e} - \frac{2\,k_B T_w}{e}\right) \\ + j_{bd}\left(\frac{A_f}{e} + \frac{2k_B T_e}{e}\right) - j_{em}\left(\frac{A_f}{e} + \frac{5}{2}\frac{k_B T_w}{e}\right) - j_{sem}\left(\frac{A_f}{e} + \frac{5}{2}\frac{k_B T_w}{e}\right), \end{aligned} \tag{26}$$

where $j_{i,G}$, $j_{i,M}$ $j_{bd}$, $j_{em}$, and $j_{sem}$ represent the density currents due to different particle fluxes: $j_{i,G}$ is the current density due to plasma gas ions, $j_{i,M}$ is the current density due to metal gas ions, $j_{bd}$ is electron back diffusing current density, $j_{em}$ is the electron emission current density, and $j_{sem}$ is the secondary electron emission. $U_c$ is the voltage drop in the near-cathode layer, $E_{i,G}$ and $E_{i,M}$ are the average ionization energy of the plasma gas and metal gas, respectively. $k_B$ is the Boltzmann constant and $e$ is the elementary charge. $T_e$ and $T_w$ represent the electron temperature and the electrode surface temperature, respectively. The first two term in the right-hand side of equation $(26)$ corresponds to the heating of the cathode by ions arriving at the surface, the main mechanism of cathode heating. The third term represents the electrons back diffusing to the surface heating the cathode. The other two terms have a cooling effect on the cathode caused by electron emission: thermo-field / thermionic emission, and secondary electron emission.

As can be seen in equation $(26)$, to calculate the heat flux to the cathode one must first know the contribution of each particle flux to the total current density. The voltage drop in the near-cathode region ($U_c$) also has to be either assumed or estimated. There are common methods presented in the literature to apply equation $(26)$, however the term corresponding to the metal gas ions is not considered in this work.

*Fixed current density ratio*

Probably the simplest approach to calculate the heat flux to the cathode is to fix the contribution of each particle flux. This has been done in the literature to study the arc in supersonic nozzle typical of plasma torch or high-voltage circuit breakers [47], as well as low-voltage applications [48]. Both works are based on the estimations made in [49]:

$$\frac{j_e}{j_w} = 0.78\,, \tag{27}$$

$$j_w = j_{i,G} + j_e\,. \tag{28}$$

Expressions $(27)$ and $(28)$ mean that the electron emission current is calculated from the total current density crossing the interface, regardless of the operating conditions in the cathode. It also limits the contribution to the current to electrons emission ($j_e$) and plasma gas ions ($j_{i,G}$), and so equation $(26)$ is reduced to:

$$q_{cath} = j_{i,G}\left(U_c + E_{i,G} - \frac{A_f}{e} + \frac{5}{2}\frac{k_B T_e}{e} - \frac{2\,k_B T_w}{e}\right) - j_e\left(\frac{A_f}{e} + \frac{5}{2}\frac{k_B T_w}{e}\right). \quad (29)$$

It is important to mention that the ratio calculated in [49] corresponds to thermionic cathodes. Therefore, it has to be adjusted for the case of cathodes made of no-refractory materials, such as copper or silver.

Regarding the voltage drop in the near-cathode layer, the work cited before assumed constant values around 15 V. However, it is also possible to define the voltage drop as a function of the local current density ($j_w$) with an expression of the form:

$$U_c = \frac{a\,j_w + b\,j_w^d}{c + j_w^d}\ , \quad (30)$$

where $a$, $b$, $c$, and $d$ are coefficients to be determined based on experimental observations. Figure 13 shows the voltage – current characteristics for the cathode obtained with equation $(30)$ [50]. It shows how at low currents the voltage drop near the cathode tends to zero, while at high currents the voltage drop approaches asymptotically 10 V. A peak value of 22 V around $10^4\ A/m^2$ allows to take into account the hump in voltage observed in experiments [24].

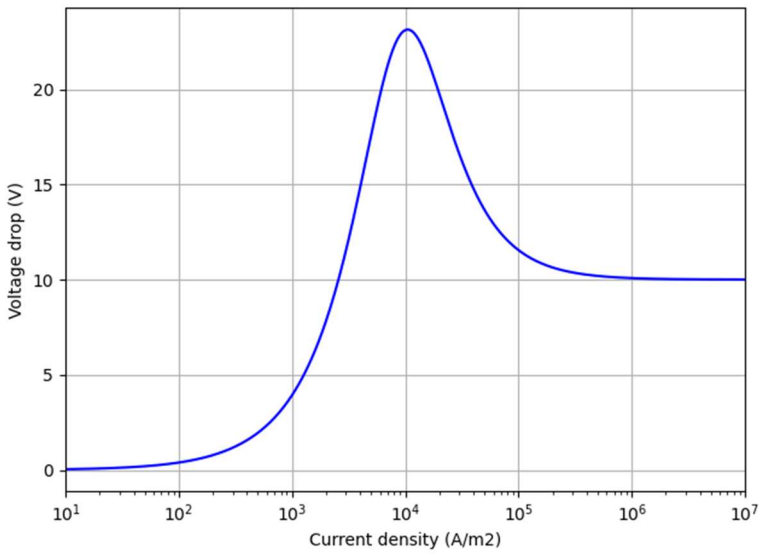


Figure 13. Voltage drop in the near-cathode layer as a function of the current density for a copper cathode.

*Lowke's model*

Another possibility is to use an approach based on the simplified unified theory, proposed in [51]. Here the electron current density due to thermionic emission ($j_e'$) is obtained from the Richardson equation:

$$j_e' = A\, T_w^2 \exp\left(\frac{-A_f e}{k_B T_w}\right), \tag{31}$$

where $A$ is the Richardson constant. As can be seen in equation (31), the calculation of the thermionic electron emission takes into account the cathode condition, the higher the cathode surface temperature ($T_w$), the higher the contribution of the electron emission current ($j_e$) to the total current density ($j_w$). Two cases are possible depending on the value of the electron emission current [18]:

$$j_e = \begin{cases} j_e' & if \quad j_e' < j_w \\ j_w & if \quad j_e' \geq j_w \end{cases}. \tag{32}$$

As noted by [52], one limitation of the simplified unified theory is that the thermionic current density calculated with equation (31) may be larger than the total current density crossing the interface, and so the current conservation is not assured. That is why the electron emission current is often limited, as in equation (32). Another limitation in this theory is the fact that the space-charge region is not considered.

In a similar way to the previous method, equations (28) and (29) are used to calculate the ion current density and the heat flux to the cathode, respectively:

$$j_w = j_{i,G} + j_e ,$$

$$q_{cath} = j_{i,G}\left(U_c + E_{i,G} - \frac{A_f}{e} + \frac{5}{2}\frac{k_B T_e}{e} - \frac{2\, k_B T_w}{e}\right) - j_e\left(\frac{A_f}{e} + \frac{5}{2}\frac{k_B T_w}{e}\right).$$

*NCPL: Near-Cathode Plasma Layer*

A more complex approach can be implemented with the Near-Cathode Plasma Layer model. This model calculates key characteristics of the near-cathode layer as a function of two

variables: the cathode surface temperature ($T_w$), and the voltage drop in the near-cathode region ($U_c$) [53]. The characteristics calculated are:

- $q_{cath}(T_w, U_c)$: The heat flux from the plasma to the cathode surface.
- $j_w(T_w, U_c)$: The current density from the plasma to the cathode surface.
- $T_e(T_w, U_c)$: The electron temperature in the near-cathode region.
- $p_w(T_w, U_c)$: The pressure exerted by the plasma over the cathode surface (not used in this work).

The heat flux ($q_{cath}$) and the current density ($j_w$) from the plasma to the cathode surface are determined as:

$$q_{cath} = j_{i,G}\left(U_c + E_{i,G} - \frac{A_f}{e} + \frac{5}{2}\frac{k_B T_e}{e} - \frac{2\,k_B T_w}{e}\right) + j_{bd}\left(\frac{A_f}{e} + \frac{2k_B T_e}{e}\right) - j_{em}\left(\frac{A_f}{e} + \frac{5}{2}\frac{k_B T_w}{e}\right) - j_{sem}\left(\frac{A_f}{e} + \frac{5}{2}\frac{k_B T_w}{e}\right), \quad (33)$$

$$j_w = j_{i,G} + j_{em} + j_{sem} - j_{bd}\,. \quad (34)$$

Since the NCPL model considers that the plasma-cathode interaction is dominated by the phenomena in the near-cathode layer with little-to-none influence from the plasma in the arc column, arc current, and cathode shape; the arc-cathode characteristics only need to be calculated one time for a given combination of plasma gas, plasma pressure, and cathode material [8]. The NCPL model is freely available on the internet or as an executable file, and the equations with the solution procedure are summarized in [54]. Originally it was developed for thermionic cathodes, and so only the particle fluxes of ions, back diffusing electrons, and thermionic emission were taken into account. However, the NCPL code has been recently modified by adding the secondary electron emission to be used in non-thermionic cathodes, where the surface temperature is not high enough to sustain the current by thermionic emission only.

An example of the arc-cathode interaction characteristics calculated with the NCPL is presented in Figure 14 to Figure 16. It corresponds to a case of argon plasma at 1 bar interacting with a cathode made of tungsten. The values of cathode temperature and near-cathode voltage drop, for which the NCPL characteristics are calculated, range from 300 K to 5000 K and 10 V to 500 V, respectively.

The current density crossing the interface ($j_w$) is shown in Figure 14. One can see how for low values of cathode surface temperature ($T_w < 1500$ K) and near-cathode voltage drop

($U_c < 150$ V) the current density is rather small, while on the other side the higher values are found for cathode temperatures higher than 4000 K, almost independent from the near-cathode voltage drop.

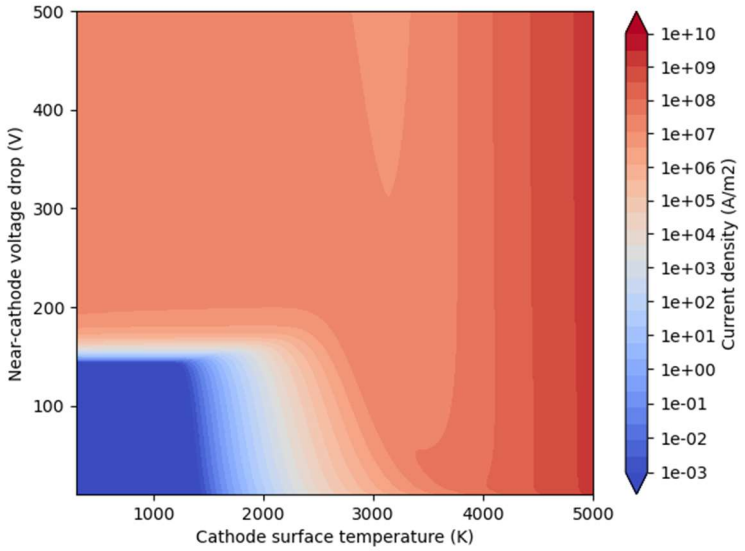


Figure 14. Current density to a tungsten cathode calculated with NCPL.

A similar behavior is observed in Figure 15 for the heat flux to the cathode. At low values of cathode temperature and voltage drop in the near-cathode layer the heat flux directed to the cathode is almost zero. To find considerable heat fluxes, it is then necessary to increase either the surface temperature of the cathode or the near-cathode voltage drop.

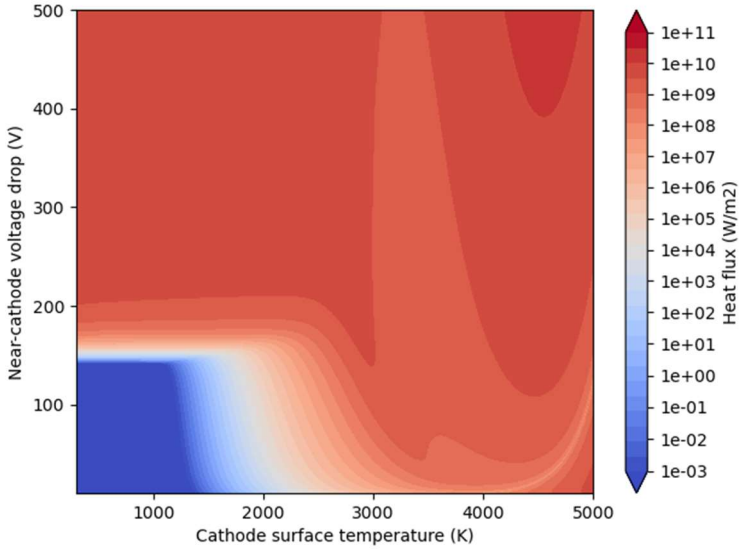


Figure 15. Heat flux to a tungsten cathode calculated with NCPL.

Another important characteristic calculated with the NCPL model is the electron temperature ($T_e$) in the near-cathode layer. The range of electron temperatures obtained is very broad as shown in Figure 16, it goes from a few thousand Kelvins to more than one million Kelvins. It is important to note that $T_e$ is a representative temperature of the integral near-cathode layer and hence the high values observed, however these values may cause also an extremely increase of the LTE plasma temperature in the arc column. Therefore, it is convenient to limit the maximum $T_e$ to a more reasonable value, for example 35000 K to assure solution convergence.

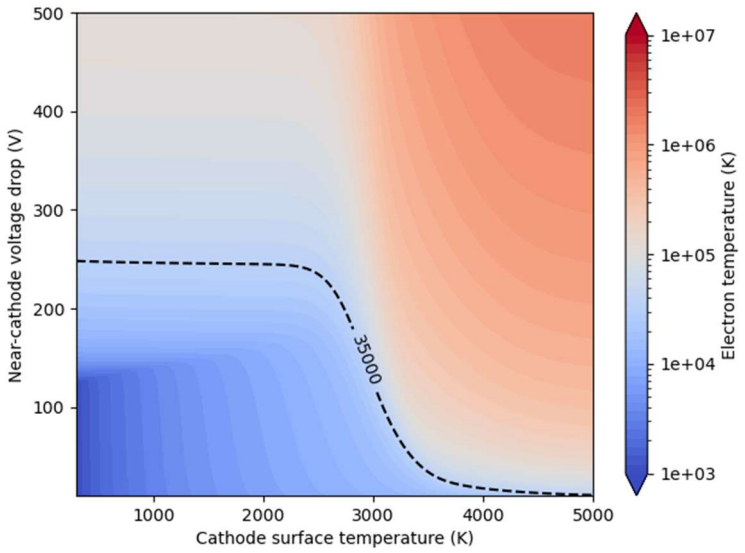


Figure 16. Electron temperature in the near-cathode layer of a tungsten cathode calculated with NCPL.

Once the arc-cathode interaction characteristics have been calculated with the NCPL model, they can be used to find the temperature and current distribution inside the cathode. This is done according to the non-linear surface heating method.

The profiles of cathode temperature and the near-cathode voltage drop are used to evaluate $q_{cath}(T_w, U_c)$ and $j_w(T_w, U_c)$ along the cathode surface, where $U_c$ is considered as constant at all points in the cathode surface. Then the heat conduction equation is solved in the cathode to obtain the new temperature distribution. The resulting arc current $I^*$ is given by integrating $j_w(T_w, U_c)$:

$$I^* = \int_S j_w(T_w, U_c)\, dS\,. \tag{35}$$

Since the arc current ($I$) is usually an input or known function in arc modelling, it can be compared with the integrated current ($I^*$) from equation $(35)$. In case the input arc current and the integrated current difference is higher than a predefined tolerance, the near-cathode voltage drop (which is used as a control parameter) is adjusted, and a new temperature distribution is calculated. This process is repeated until the integrated arc current converges.

The final step consists of using the converged solution in the cathode to calculate the plasma side. As the current density is conserved along the near-electrode layer, the current density condition on the plasma boundary is equal to $j_w(T_w, U_c)$. The second condition corresponds to the energy transfer to the plasma from the near-electrode region ($q_{plas}$), that is obtained from equation $(25)$.

In the next section, the NCPL model will be used to model the electric arc in a transient free burning configuration with novelty that the cathode starts with a cold temperature (300 K), which was not possible before in previous NCPL versions. However, in some configurations with non-refractory cathode, the results using the NCPL model are not satisfactory, as will be explained in the following chapters. In those cases, the fixed ratio approach will be used.

***Near-anode region***

As opposed to the cathode, the ion current in the near-anode layer is much smaller than the electron current, so it can be assumed that all the arc current crossing the interface is due to electron current.

$$j_w = j_e \,. \tag{36}$$

For the voltage drop in the near-anode layer ($U_a$), a curve similar to the one presented for the cathode in Figure 13 can be used at the anode-plasma interface:

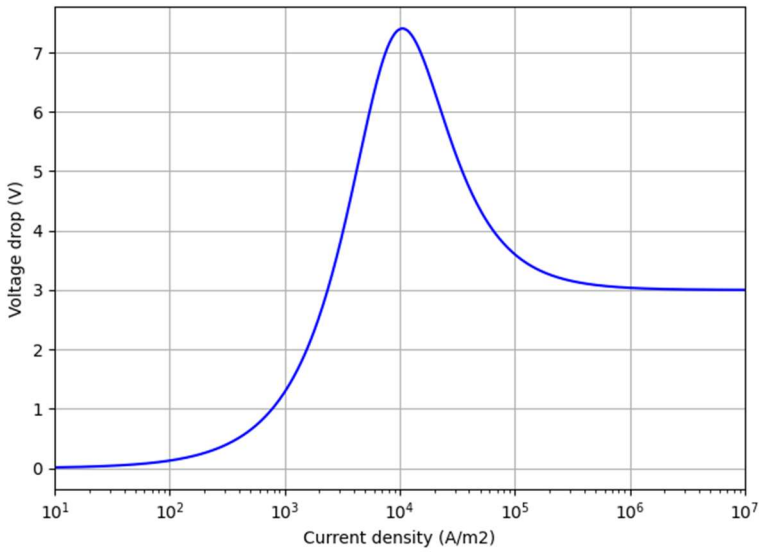


Figure 17. Voltage drop in the near-anode layer as a function of the current density for a copper anode.

Figure 17 shows the voltage drop – current density characteristic in the near-anode layer. It also presents a peak voltage and an asymptotic voltage, although their magnitudes are lower than those of the near-cathode layer.

The transfer of energy to the anode ($q_a$) is given by the following expression [5]:

$$q_a = j_w \left( \frac{5}{2} \frac{k_B T_e}{e} + \frac{A_f}{e} + U_a \right) . \tag{37}$$

As noted in [5], [46], the contribution of the near-anode voltage drop term to the anode heating is quite small and it can be omitted. Equation (37) can be applied directly during the calculation by taking the electron temperature ($T_e$) as the LTE temperature in the arc column.

An alternative to calculate $q_a$ is to use the heating voltage definition. It states that the heat flux to the anode is proportional to the current density, using the heating voltage as the proportionality constant:

$$q_a = j_w \, U_h \, , \tag{38}$$

where $U_h$ is the heating voltage. The values of $U_h$ have been calculated and tabulated for different arc conditions using the unified modelling approach, as in [10]. For example, a copper anode interacting with an argon plasma arc at different pressures gives the following heating voltages:

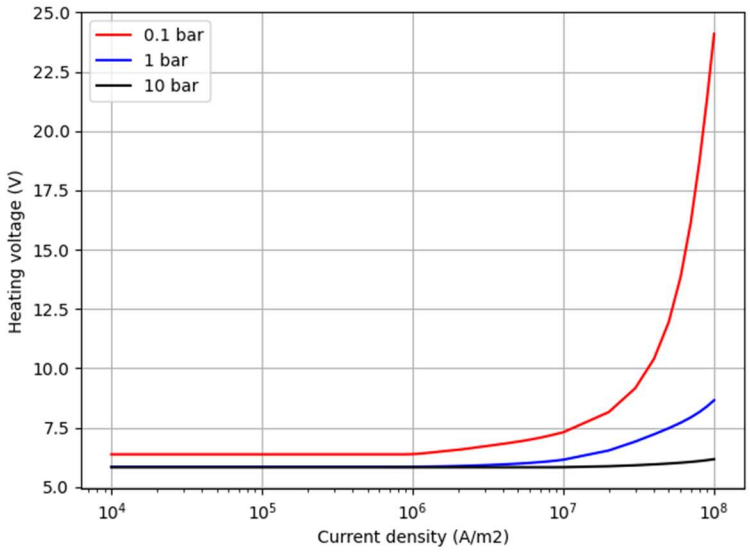


Figure 18. Heating voltage as function of the current density and different pressures. (Plasma gas: argon, anode: copper)

From Figure 18, it is possible to observe how the values of $U_h$ increases at higher current densities, and how it also increases as the pressure decreases. These values of heating voltage can be directly used in equation $(38)$ to obtain the anode heat flux.

## 2.3. EXAMPLE OF THE ARC-ELECTRODE INTERACTION MODELS IN A FREE BURNING ARC

In this section a transient free burning arc configuration is used to implement and study the recently developed NCPL model with consideration of the secondary electron emission, and the anode heating voltage approached described above. The free burning configuration was chosen because it is a well-known study case of arc modelling in the literature, the geometry is relatively simple, it has a steady-state solution, and numerous publications with experimental measurements are available to compare.

### 2.3.1. Case description

The configuration studied in this section is typical of gas tungsten arc welding (GTAW) processes and it is based on the operating conditions described in [46], [55]. It consists of a rod cathode made of tungsten, with a length of 12 mm, and a hemispherical tip of radius equal to 1 mm. The anode is a plate made of copper, with a radius of 30 mm, and a thickness of 4 mm. The electrodes are surrounded by an Argon gas volume and the interelectrode distance is 10 mm. Given the geometric characteristics of this configuration, it is possible to treat it as an axisymmetric case, as shown in Figure 19.

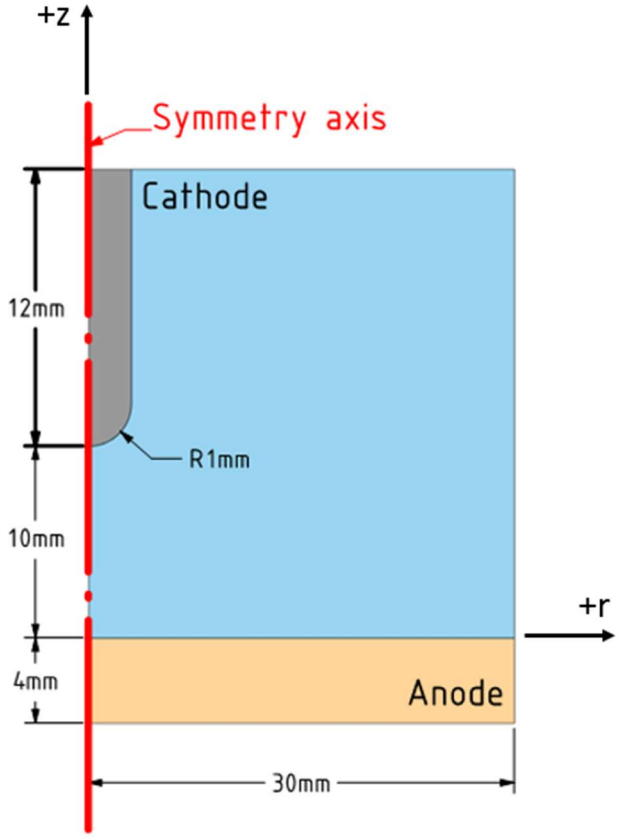


Figure 19. The free burning arc configuration.

### 2.3.2. Boundary and initial conditions

For the boundary condition, the top end of the cathode is set at a constant temperature of 300 K and a potential equal to 0 V. The same conditions are applied to the bottom face of the anode. The lateral face of the anode is defined as adiabatic for the energy equation and electrical insulator. The top boundary in the gas is set as a wall at constant temperature (300 K), while at the lateral gas boundary the pressure outlet condition is applied with a constant

gauge pressure of 0 Pa, as well as zero current and energy flux. Both the top and lateral boundaries in the gas are set as electrical insulators.

At the cathode-plasma interface, the $q_{cath}(T_w, U_c)$ and $j_w(T_w, U_c)$ functions obtained with the NCPL model is used to describe the energy and current transfers between the arc column and the cathode, as explained in the previous section. Because of the high cathode temperatures that can be reached in GTAW processes, the radiation losses in the cathode are included in the energy balance. On the other side, the heating voltage definition is used at the anode-plasma interface, with the values of $U_h$ taken from Figure 18. The voltage drop in the near-anode layer ($U_a$) is neglected.

Concerning the initial conditions, one of the novelties of the present work is the possibility of using the arc-electrode models to study the arc ignition from cold electrodes to their final hot state. Previously, the use of the NCPL model was limited to thermionic cathodes where the electrode was initialized at an already high temperature. The addition of the secondary electron emission then allows to apply the NCPL model to cathodes in the temperature range where current due to thermionic electron emission is not the dominant mechanism.

The electrodes in this example are initialized at ambient temperature, 300 K. An electrically conductive path between the electrodes is necessary in order to start the calculation. This is achieved by defining an initial temperature profile in the gas that is high enough to make it conductive. The temperature profile is expressed as:

$$T_{pl}^0 = 300\ K + 12000\ K\ \exp\left(-\frac{r^2}{r_0^2}\right), \tag{39}$$

where $T_{pl}^0$ is the gas initial temperature, $r_0$ is a parameter set to 10 mm, and $r$ is the radial coordinate. It is worth mentioning that this initial temperature profile is a pure hypothetical condition defined to observe the convergence of the arc column after the electrodes heat up with previous stationary works.

The problem described is solved for 10 s of simulated time to assure that the solution reaches the steady state. The arc current is applied as an input increasing from 0.01 A to a constant value of 200 A following a ramp function, as illustrated in Figure 20. This case was implemented and solved in COMSOL Multiphysics 6.1 using a time-dependent fully coupled solver.

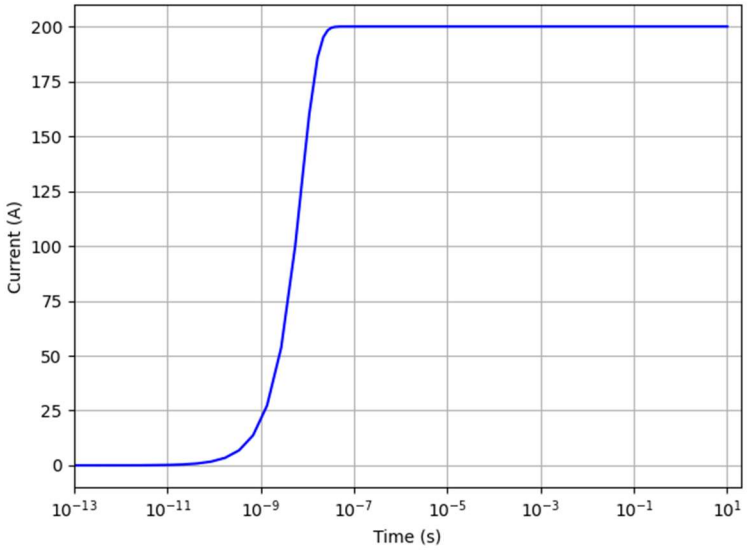


Figure 20. Current applied as function of time.

### 2.3.3. Results

Figure 21 shows the evolution of the arc voltage (solid line) and the near-cathode voltage drop (dashed-line) with time. Three main stages can be identified in the figure separated by black vertical dotted lines, in what can be called a cold-to-hot cathode transition:

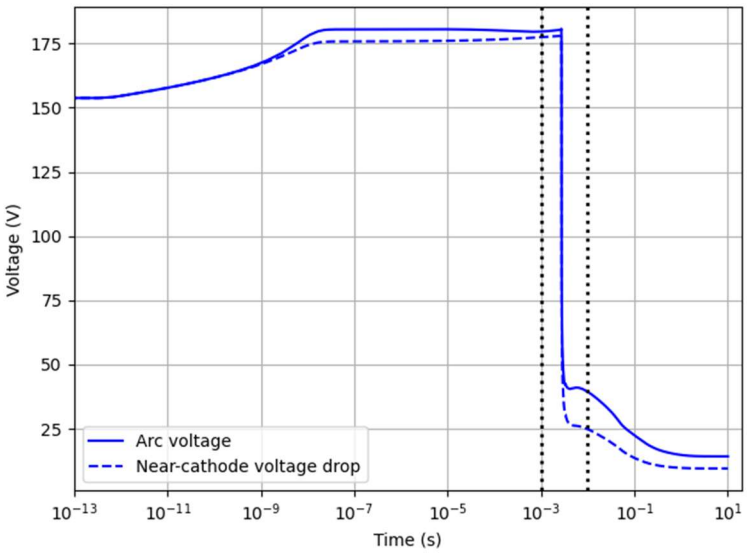


Figure 21. Temporal evolution of the arc voltage and near-cathode voltage drop.

The first stage corresponds to the cold cathode phase and takes place during the first 2 ms. It is characterized by high voltage values that increase up to 180 V, mainly due to the

voltage drop in the near-cathode layer. The contribution of the arc column to the arc voltage only accounts for a few volts. The cold-to-hot transition occurs in the second stage between 2 ms and 3 ms, approximately. During the transition, the voltage drop goes from 180 V to 40 V very rapidly, and at the end of the transition the voltage drop in the arc column correspond to 15 V. In the final stage corresponding to the hot cathode phase, the voltage continues to decrease but at a lower rate until the final value of 15 V is reached, where 10 V corresponds to the near-cathode layer and 5 V to the arc column.

Figure 22 presents the evolution in time of the temperature at the cathode tip. Initially, the cathode tip temperature starts increasing progressively until the transition. At this point, the temperature jumps from 2400 K to around 4300 K. Finally, in the hot cathode phase the temperature at the tip continues to increase to a maximum value of 4750 K, and then decreases to its steady-state temperature 3990 K.

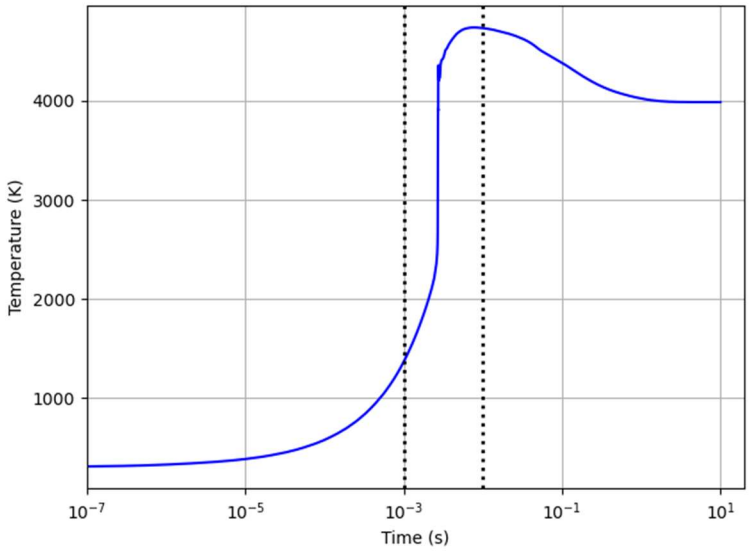


Figure 22. Temporal evolution of the temperature at the cathode tip.

***Cathode***

To better understand the processes involved in the cathode during the 10 s, images of the temperature distribution, as well as the surface profiles of temperature and current density are presented.

Figure 23 shows the temperature distribution in the cathode at three different moments: 2 ms (cold cathode phase), 2.75 ms (cold-to-hot transition phase), and 10 s (hot cathode phase). The cathode, initially at ambient temperature, is heated uniformly along all its surface during the cold phase. Then, as the cathode continues to be heated, a hot spot appears at the

cathode tip during the transition from cold to hot cathode. Once the transition is over and the system reaches its steady state, the temperature is more evenly distributed inside the cathode volume, with higher temperatures located at the bottom part that decrease towards the top end.

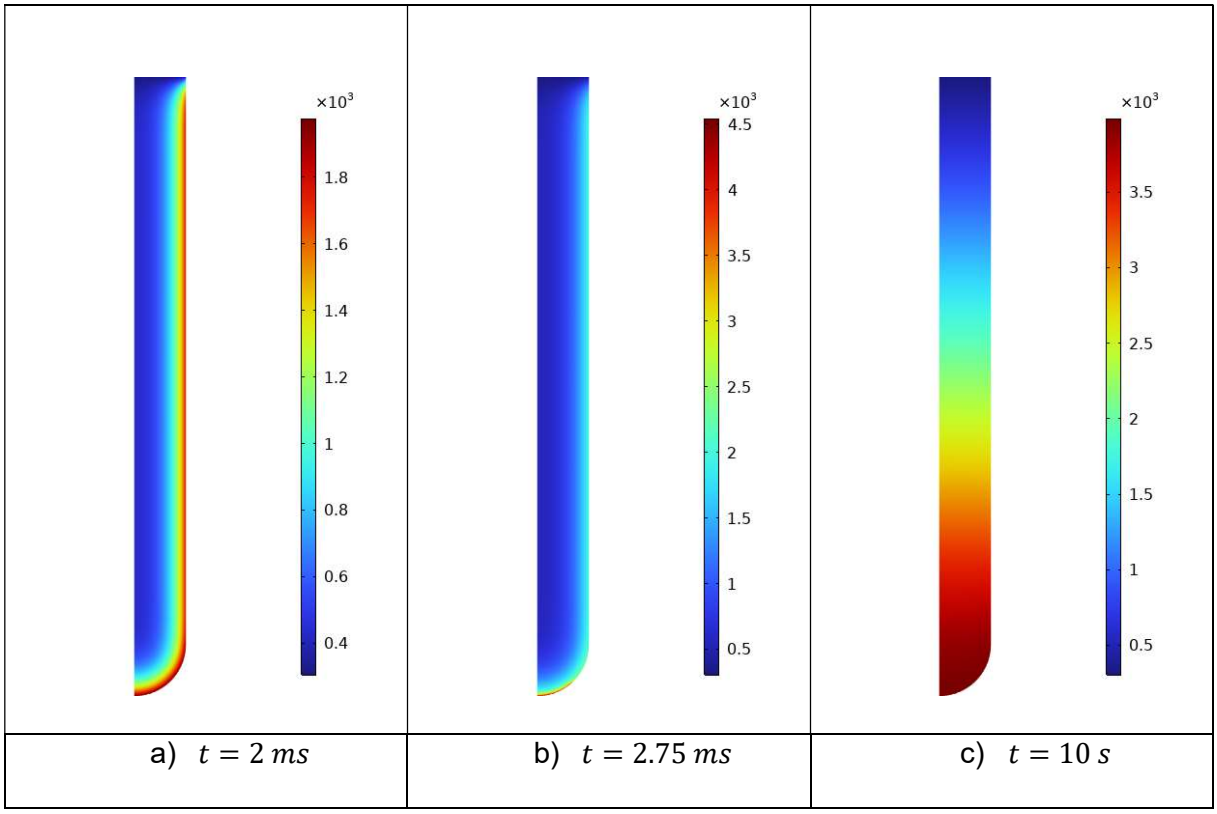


a) $t = 2\ ms$ b) $t = 2.75\ ms$ c) $t = 10\ s$

Figure 23. Temperature distribution in the cathode at different times.

The surface temperature and current density profiles in the cathode are presented in Figure 24 and Figure 25 as functions of the spatial coordinates ($r + z$). After 2 ms, the cathode has an almost constant temperature along its surface around 1800 K. The current density profile is also constant at this instant, meaning that all the cathode surface is current collecting. When the cold-to-hot transition occurs, around 2.75 ms, the temperature in the hot spot reaches values as high as 4550 K, while the rest of the cathode surface stays at 1920 K. At the cathode tip the current density increases to $2 \cdot 10^8\ A/m^2$, which is several orders of magnitude higher than the current density values outside the hot spot. Therefore, all the current is collected at the cathode hot spot. Finally, once the transition is over and the arc stabilizes, the temperature variations are smoother, with a maximum of 4000 K at the tip, and progressively decrease to the external cooling temperature of 300 K. The current collecting

surface also increases compared to the transition phase. The maximum in the current density occurs at the cathode tip ($2 \cdot 10^7\ A/m^2$), and gradually decreases as one moves away from the tip.

The magenta dashed line in Figure 24 corresponds to the numerical results obtained in [56] at 2 s, where the current transfer to a thermionic cathode was modelled starting from an already hot electrode and considering the melting of the cathode and the motion of the molten metal pool. The comparison of our results at the steady state with those of [56] shows similar values of temperature along the cathode surface. It also serves to prove that the modified NCPL version implemented in this work will yield the correct temperature profile in the cathode without guessing an initial high temperature profile.

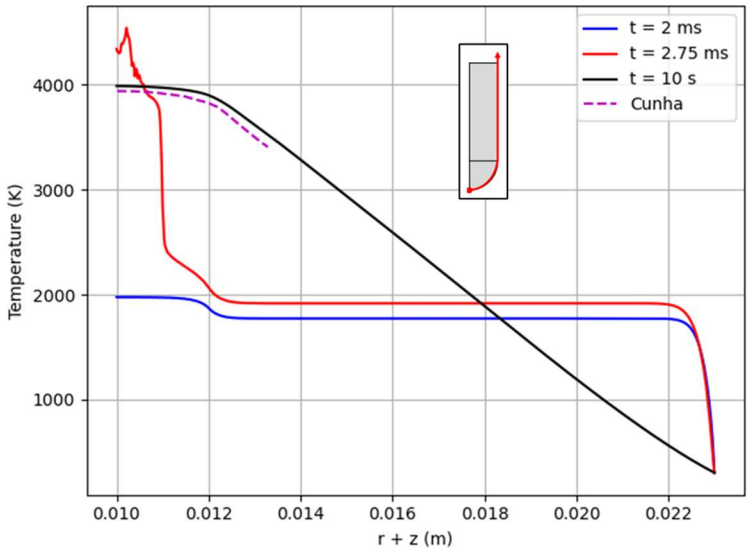


Figure 24. Cathode surface temperature profiles at different times.

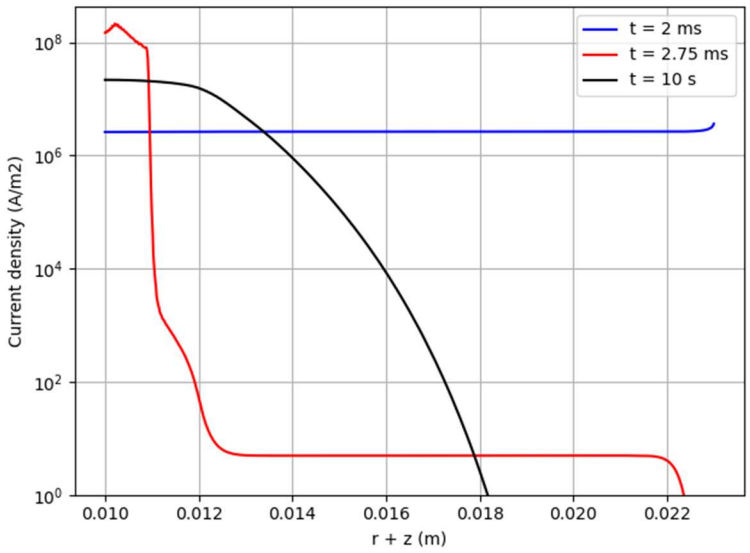


Figure 25. Current density profiles at different times.

These results obtained for the cathode can be understood as follows: during the first stage, the relatively low temperatures along the cathode surface makes the thermionic emission insignificant. Therefore, a high voltage is needed to sustain the current which is mainly due to ions.

Once the temperature starts increasing at the cathode tip and the hot spot is formed, the thermionic current begins to be comparable to the ion current. As the hot-spot temperature continues to rise, the thermionic emission becomes the dominant current mechanism, which in turn allows for a significant decrease of the voltage. This marks the transition stage described before.

Finally, with the calculation advancing in time, the temperature is more evenly distributed, and the current collecting surface increases. However, the cathode temperature in the lower part of the body is still high enough for the thermionic emission to be the main current transfer mechanism.

### *Arc column*

The results in the arc column are described next, starting from an arbitrary temperature profile, to evaluate its convergence in the steady state with previous stationary solutions reported in the literature. Figure 26 presents an image sequence describing the temperature distribution in the arc column from the initial conditions to its steady state, while Figure 27 compares the temperature profiles along the symmetry axis.

At $t = 0\ s$, a high temperature profile is imposed in the arc column in order to have an electrically conductive path between the electrodes, and then the argon temperature increases in the region close to the electrodes where the current flows.

The effects of the cold-to-hot cathode transition on the arc column are visible at $t = 2.75\ ms$. The plasma located below the cathode tip shows an abrupt increment in the temperature, reaching values up to 40000 K. This can be attributed to phenomena taking place in the hot spot (high cathode surface temperatures and high near-cathode voltage drops), and the fact that all the current flow at the arc-cathode interface is restricted to a small surface.

The arc in its steady state condition at $t = 10\ s$ displays lower temperatures in the symmetry axis. The maximum temperature is below the cathode tip with a value of 17200 K, the decreases in the center region of the arc before increasing again at 1 mm from the anode. The results obtained in the arc column after 10 ms matches the values reported in [46], which corresponds to an stationary study, although a difference is noticed close to the anode due to a slightly different formulation at the arc-anode interface.

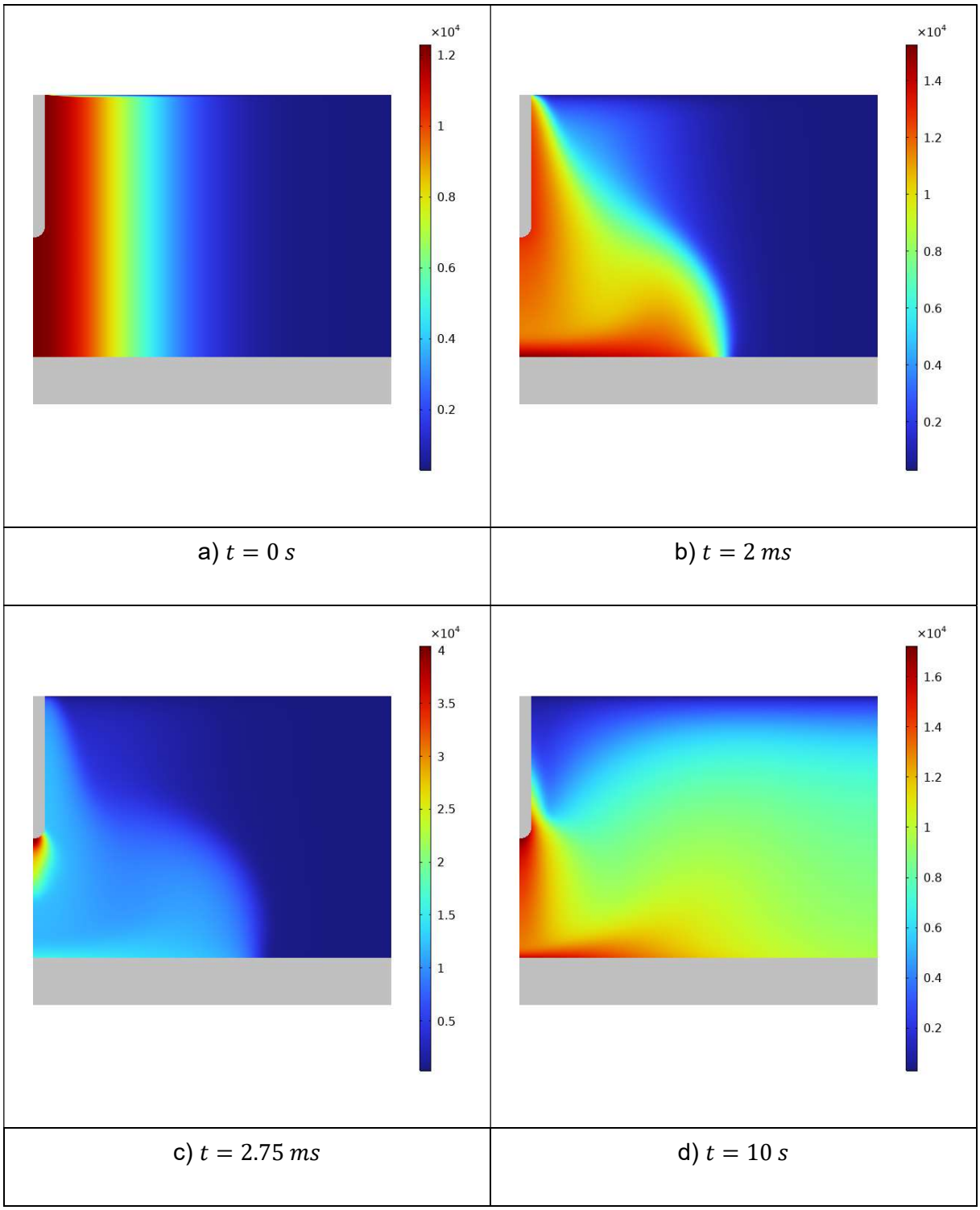


Figure 26. Temperature distribution in the arc column at different times.

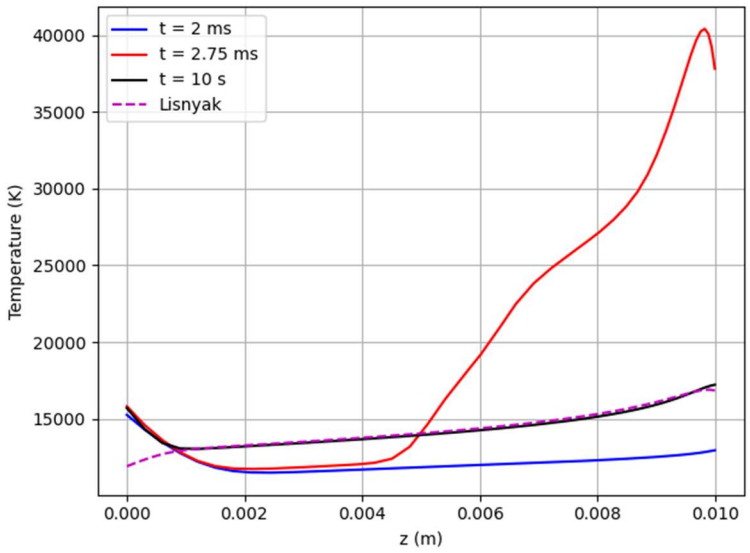


Figure 27. Arc column temperature profiles along the symmetry axis at different times.

***Anode***

Regarding the anode, no important variation in its temperature is observed during the calculation. This is due to the relatively low current densities at the arc-anode interface and the imposed cooling condition of 300 K at the bottom face and its proximity to the heated surface. Figure 28 describes the temperature at the center of the anode surface heated by the arc and its evolution with time. At first, the temperature raises by 10 K after 2 ms, then during the transition the slope of the curve becomes stepper, and the temperature reaches a value of 355 K. Finally, the temperature at the center of the anode stabilizes at 345 K. The temperature distribution in the anode at $t = 10\ s$ is shown in Figure 29.

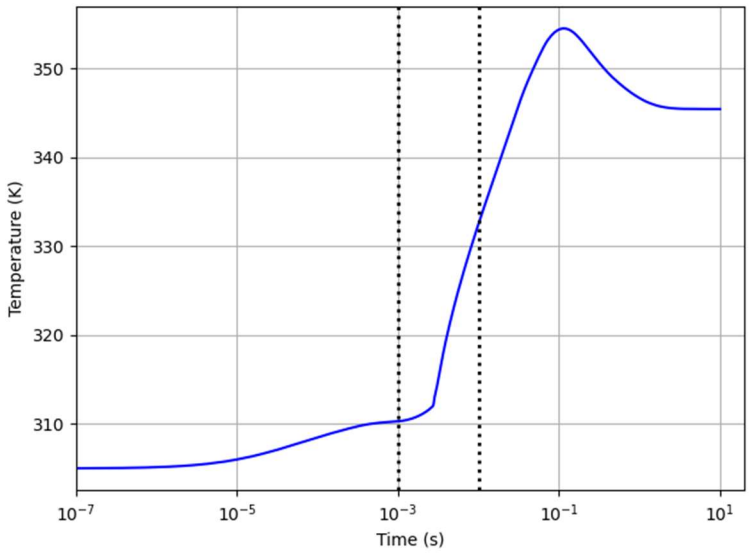


Figure 28. Temporal evolution temperature at the center of the top anode surface.


Figure 29. Temperature distribution in the anode at 10 s.

This section has shown the results for a complete transient arc model in a free burning configuration. The fact that the electrodes are heated from an initial cold condition leads to strong variations in the arc voltage due to the cold-to-hot transition in the cathode. Since this is the dominant and most interesting phenomenon observed during the calculations, additional studies are performed to evaluate its impacts on the model global behavior. These studies include the influence of the arc current, the cathode shape, the addition of an electric circuit, and the approach used to couple the arc and cathode solutions.

### 2.3.4. Influence of the arc current

The first parameter studied is the arc current imposed on the arc-cathode interface. A comparison of the voltage drop in the near-cathode layer is presented in Figure 30 for three currents: 20 A, 100 A, and 200 A. The 20 A case has the lowest near-electrode voltage drop during the cold phase with a value of 167 V compared to 176 V at 200 A.

Also, the cold-to-hot transition is delayed as the current decreases. The transition occurs at 50 ms at 20 A, while it only takes around 2.7 ms when the current is 200 A. For the intermediate case, 100 A, the transition from cold to hot cathode happens at 7 ms. This can be explained by a slower increase of the cathode surface temperature at lower currents as seen in Figure 31. The maximum temperature reached in the cathode tip is also affected by the arc current specified. A maximum of 4750 K appears a few milliseconds after the transition for a current of 200 A, while maximum temperature values of 5060 K and 4980 K show at the end of the cold-to-hot cathode transition for 100 A and 20 A, respectively.

The cathode tip temperature and near-cathode voltage drop values at the steady state are similar for 100 A and 200 A. At a current equal to 100 A the values obtained are 10 V and 3900 K, while for 200 A they are 9.38 V and 3990 K. When the arc current is 20 V, then the temperature at the cathode tip is 3590 K and the voltage drop in the near-cathode layer is 14.4 V.

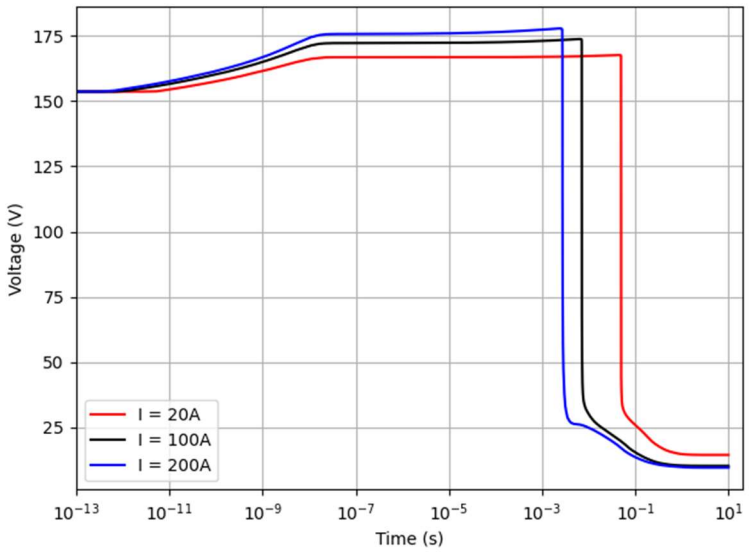


Figure 30. Temporal evolution of the near-cathode voltage drop for different currents.

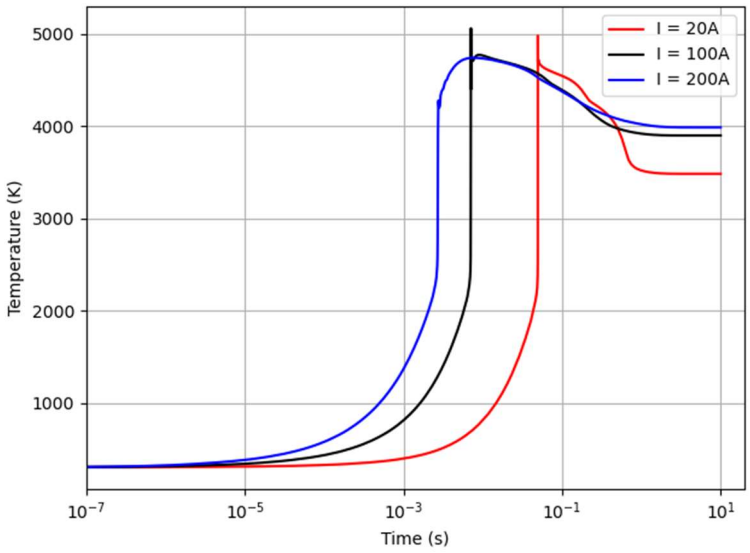


Figure 31. Temporal evolution of the cathode tip temperature for different currents.

### 2.3.5. Influence of the cathode geometry

Another aspect studied is the influence of the cathode geometry on the cold-to-hot transition. Three different shapes at the cathode rod end are considered while the rest of parameters remain unchanged: a rounded end (a), a sharp end (with a 30 deg cut) (b), and a flat end (c). These geometries are presented in Figure 32.

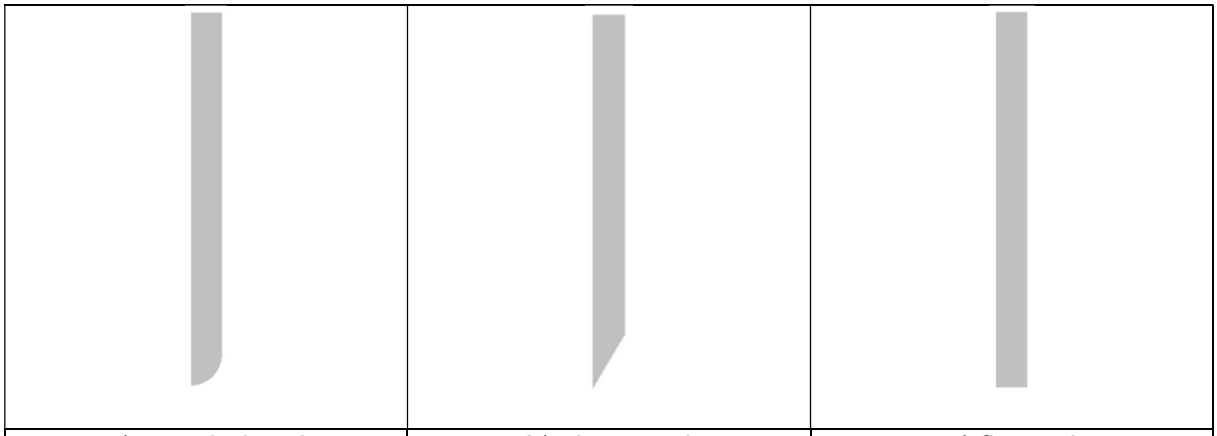

| a) rounded end | b) sharp end | c) flat end |
|---|---|---|

Figure 32. Cathode geometries studied.

The results in time are presented in Figure 33 and Figure 34 for the voltage drop in the near-cathode region and the cathode tip temperature, respectively. One particularity of the flat end case is that the maximum in temperature does not occur at the symmetry axis, but at the bottom surface edge, that is why an additional curve is plotted at this location in Figure 34.

In the cold and hot phases the near-cathode voltage drop values are similar for all cases, however some differences can be seen during the transition phase. The cold-to-hot transition occurs first in the sharp end cathode at 0.4 ms, followed by the flat end cathode at 1.38 ms, and the rounded end cathode at 2.7 ms.

Concerning the temperature values at the cathode tip, the case with the sharp end presents the fastest increase and the maximum value, 5750 K. It then gets to its steady state temperature of 4100 K. In the flat end cathode, the temperature raises faster at the edge than at the center of the bottom face, as mentioned before. The highest temperature reached is 5400 K, after the transition is over. At the final stage, the temperatures at edge and center are similar, with a value around 3950 K.

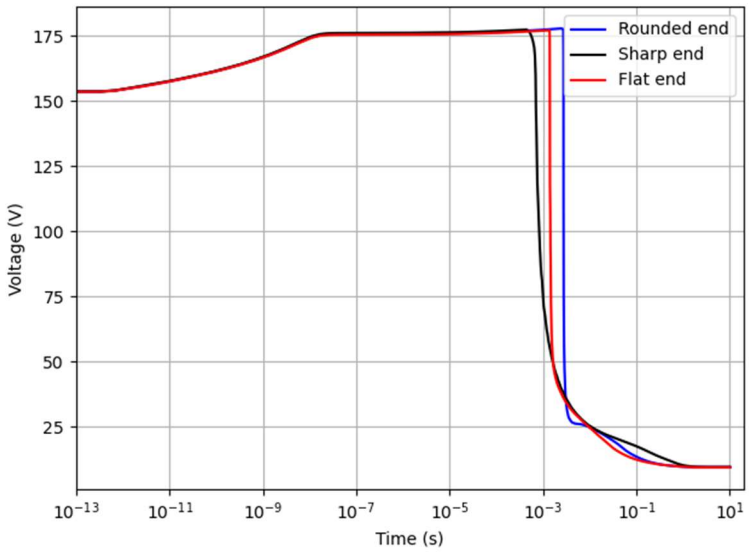


Figure 33. Temporal evolution of the near-cathode voltage drop for different cathode shapes.

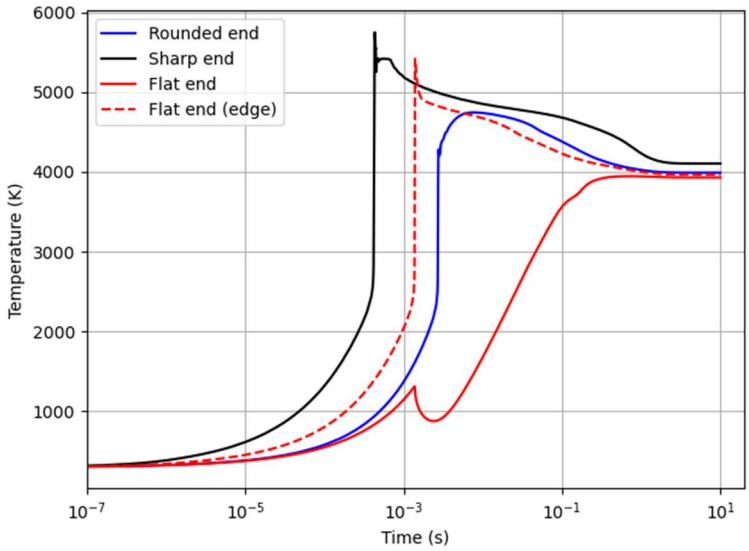


Figure 34. Temporal evolution of the cathode tip temperature for different cathode shapes.

### 2.3.6. Influence of an electric circuit

The condition of imposed arc current can be replaced by the arc current calculated from an electric circuit connected to the electrodes. This is a better representation of actual systems where the power is supplied by a voltage source, as in [57]. A simple example consists of connecting the free burning configuration in series with a DC voltage source, a resistor, and an inductor, as described in Figure 35.

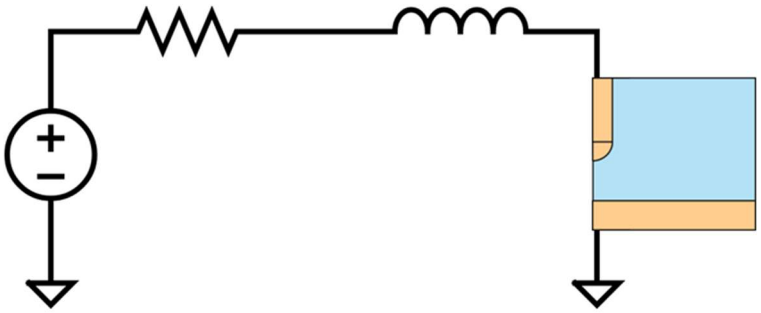

Figure 35. Free burning configuration connected to an electric circuit.

Then, the arc current ($I$) is obtained from the following equation:

$$L\frac{dI}{dt} = U_{src} - U_{arc} - I\,R\,, \tag{40}$$

where $L$, and $R$, and $U_{src}$ are the electric circuit parameters: $L$ is the inductance, $R$ is the resistance, and $U_{src}$ is the source voltage.

To understand the effects that the electric circuit has on the model, equation $(40)$ is solved together with the free burning arc model. The electric circuit parameters are arbitrary chosen as to assure a 200 A current at the steady state:

Table 3. Electric circuit parameters.

| Parameter | Value |
|---|---|
| $L$ | $1 \cdot 10^{-6}\,H$ |
| $R$ | $1.0789\,\Omega$ |
| $U_{src}$ | $230\,V$ |

The results are presented in Figure 36 to Figure 38. A notorious difference can be observed in the arc current evolution in time, shown in Figure 36. In the cold cathode phase, the current obtained with the electric circuit is significantly lower than the 200 A imposed on the previous cases. The value of 54 A in this case can be attributed to the impact that the high near-cathode voltage drop (Figure 37) has on limiting the current according to equation $(40)$. Once the transition starts and the voltage drop in the near-cathode region decreases, the arc current jumps very rapidly to 170 A. Then, as the near-cathode voltage drop stabilizes in the

hot phase to a value of 9.54 V, the current continues to gradually increase until it reaches the 200 A.

The temperature evolution in the cathode tip is described in Figure 38. The cathode temperature increases slower when the electric circuit is considered, as the current in the cold phase is lower. This also causes a delayed in the time at which the cold-to-hot cathode transition occurs, 15.5 ms. The temperature in the cathode tip reaches a maximum of 5030 K at the end of the transition, and then stays at 3990 K after 10 s.

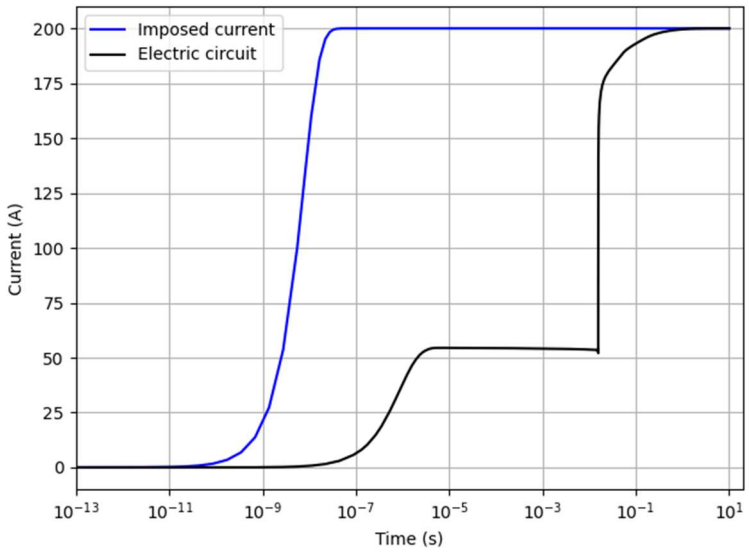


Figure 36. Temporal evolution of the arc current.

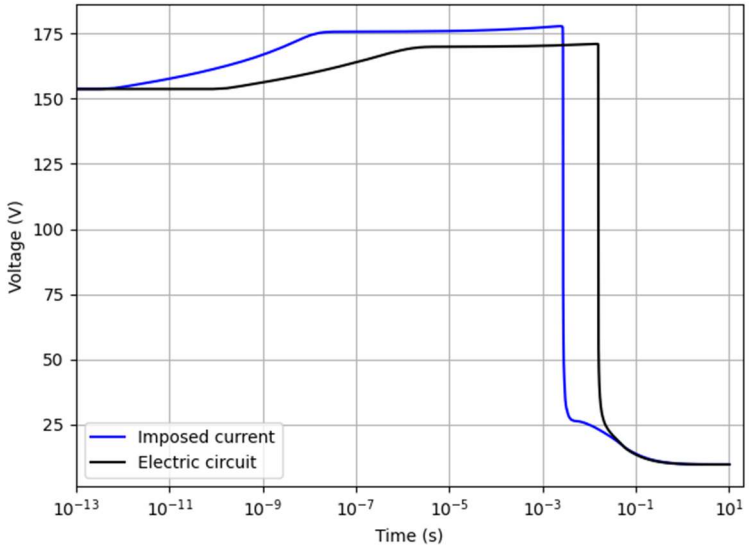


Figure 37. Temporal evolution of the near-cathode voltage drop.

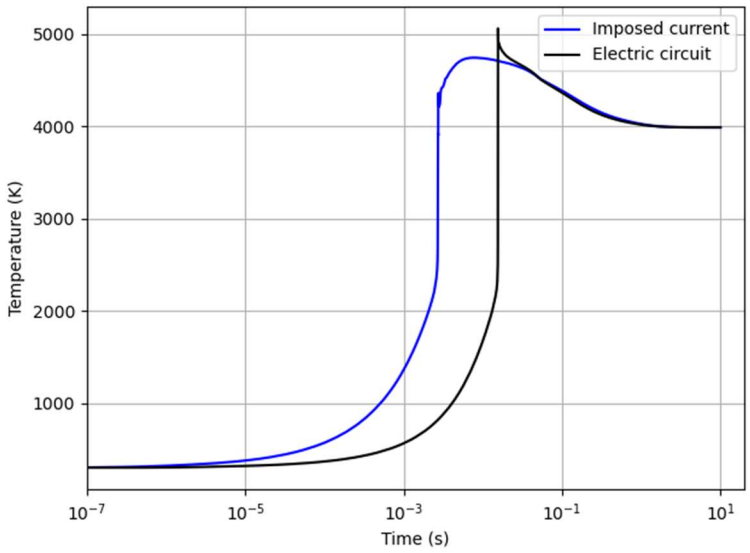


Figure 38. Temporal evolution of the cathode tip temperature.

### 2.3.7. Influence of the arc-cathode electric coupling

In all the previous calculations presented until this point, the near-electrode voltage drop ($U_c$) has been considered as constant along the cathode surface. This assumption makes the solution in the cathode completely independent of the arc column, and it is considered a unidirectional approach: the cathode is solved first, then the arc column.

In recent years, some authors have proposed a modification of this approach in order to have a more realistic condition at the arc-cathode interface. The so called bidirectional approach, based on [58], [59], uses the arc voltage ($U_{arc}$) as a control parameter during the calculations. This approach takes into account the electric potential distribution in the arc-column to calculate $U_c$, thus the cathode is no longer independent and needs to be solved simultaneously with the arc column. The near-cathode voltage drop at each point on the cathode surface is then given by:

$$U_{arc} = U_c + U_{pl}\,, \tag{41}$$

where $U_{pl}$ is the voltage drop in the arc column evaluated at the arc-cathode interface. By using equation (41), the bidirectional approach leads to a profile of near-cathode voltage drops along the cathode surface instead of a constant value.

The results in terms of the voltage drop in the near-cathode region and the temperature at the cathode tip do not show great differences between the unidirectional and bidirectional approaches, as seen in Figure 39 and Figure 40. The bidirectional case has a slightly earlier transition than the unidirectional one (1.72 ms vs 2.7 ms), and its maximum temperature reached is also higher (5120 K vs 4740 K). The profiles of the near-cathode voltage drop are presented in Figure 41. The larger variations along the surface are found during the cold cathode phase, 30 V between the top end and the cathode tip. In the hot cathode phase, this difference represents only 5 V.

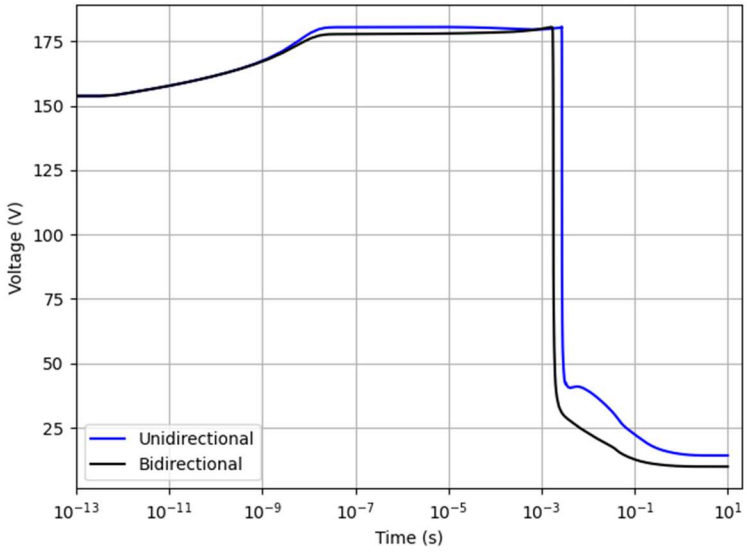


Figure 39. Temporal evolution of the near-cathode voltage drop for two different coupling approaches.

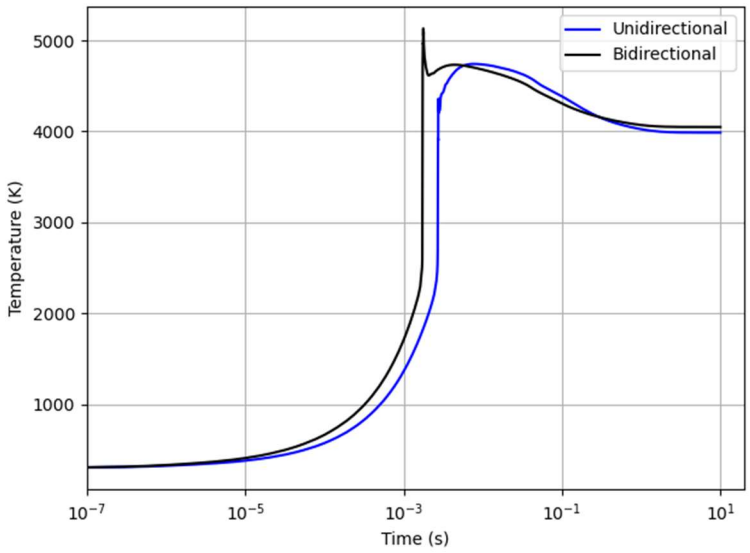


Figure 40. Temporal evolution of the cathode tip temperature for two different coupling approaches.

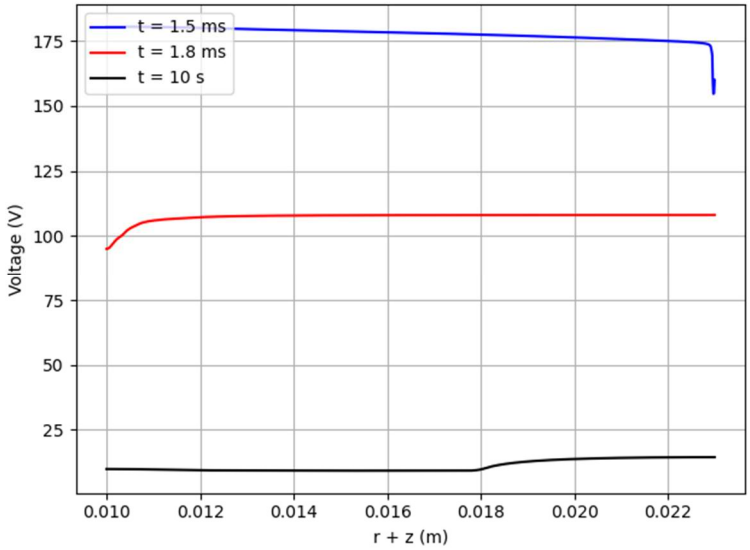


Figure 41. Near-cathode voltage drop profiles in the bidirectional case at different times.

### 2.3.8. Final remarks

The different studies performed in this configuration showed that the solution of the heat conduction in the cathode volume defines the near-cathode voltage drop variations. It was observed that the conditions that favored a faster increase in the cathode surface temperature, they all led to shorter time required to have the transition from high values of the near-cathode voltage drops to lower ones. Those conditions are higher arc currents, sharp

edges in the cathode geometry, and focalized current transfer resulting from the bidirectional coupling between the arc and the cathode.

## 2.4. SUMMARY

This chapter was dedicated to describing the modeling of the electric arc under the LTE bulk assumption. A special emphasis was given to the approach used to couple the arc column and the electrodes. The near-electrode layers were included in the model as a zero-dimensional interface, which have the advantage of avoiding strong temperature gradients close to the electrode surface that may lead to converge problems. The energy transfer at the arc-electrode interface was determined based on an energy balance in the near-electrode layer, while the current transfer was defined by the continuity condition. Since the current mechanisms at the anode and the cathode are different, a description of the near-electrode region had to be defined for each one. In the case of the cathode, ions arriving to the surface and back-diffusing electrons will heat the electrode, while it will be cooled by the different forms of electron emission. Therefore, it is important to estimate the ratio of each current mechanism to the total current. This can be simply done by fixing the ratios to a constant value, or by using a more complex model, as the NCPL model, that considers the cathode temperature and cathode fall. In the anode this is not a problem since it is mainly heated by electron condensation at the surface. The chapter finished by a test case in a gas tungsten arc welding (GTAW) configuration. This case was chosen to study a modified version of the NCPL model adapted to be used in cathodes at low temperatures. The results showed a voltage evolution that is governed by the heat conduction solution in the cathode and that follows the transition from a cold cathode to a hot one. Such calculations were not possible with previous versions of the NCPL model, since they required an initial high cathode temperature in order to calculate a steady-state solution.

# CHAPTER 3. ELECTRODE ABLATION MODEL

## 3.1. INTRODUCTION

The ablation of metallic material is important in numerous applications of thermal plasmas, where the presence of metal vapors in the processes can be incidental or an essential component. Examples where metal vapors play a key role are high-intensity discharge lamps, plasmas for production of nanoparticles, laser ablation for film deposition, among others. On the other hand, applications such as arc welding, switching devices, arc furnaces, and arc melting are instances where the appearance of metal vapors are incidental, but still significant [17].

In all these applications, numerical tools have been used to study the ablation and the effects that metal vapors have on the plasma. A classic case of study is the modeling of metal vaporization in free-burning arcs. For instance, F. Lago used a 2D axisymmetric model to perform a parametric study of the arc – anode interaction and the influence of metal vapors from the vaporization of the anode [60]. M. Schnick also presented a gas-metal arc welding model, where the metal vapors were considered to study the impact of net emission coefficient dataset used in the simulations and the rate of vaporization [61], [62]. Similarly, A. B. Murphy employed an 3D model including vaporization of the electrodes to investigate the effects of metal vapors on the arc temperature [63]. Another known author in the field is M. Tanaka, who showed the influence of iron vapors in the plasma for a gas tungsten arc [64].

Descriptions of the electrode ablation are also commonly included when modelling the electric arc in switching devices. A low-voltage circuit breaker was modelled by M. Rong to study the influence of the electrode erosion on the arc during the contact opening process [48]. F. Yang also published results of a low-voltage circuit breaker model used to analyze the erosion of the splitter plates and its impact on the arc, finding that vapors from the splitter-plate erosion have a major influence on the arc motion in the splitter-plate region [48]. More recently, J. Huo presented a simplified model of a low-voltage circuit breaker to study the wall ablation taking into account the Stefan flow caused by species generation [50]. Also, M. Baeva published a model of a low-current arc between copper electrodes using a unified model, where the metal evaporation is considered [65]. For high-voltage devices, the results of a high-voltage circuit breaker model by P. Freton showed the influence of copper vapors in a $SF_6$ plasma [66]. Moreover, Freton also proposed an ablation model for Cu/W electrodes typical of high-voltage circuit breakers, considering the diffusion and ablation vaporization regimes [67].

Other published works are also found in the literature for processes such as Layer Beam Melting (LBM), where layers of metal powders are melted by a laser beam. Y. A. Mayi

conducted a multiphysical model of vaporization under laser radiation by coupling the fluid flow and heat transfer between the melted pool and the surrounding gas [68]. Another example is the modelling of electrode erosion in plasma heaters as modelled by A. Marotta to investigate the importance of different parameters in the erosion process [69]. Finally, the impact of metal vapors in arc faults has also been studied to estimate its influence on the radiation emission losses and the pressure rise inside the enclosure, e.g. [70].

All the examples that have been mentioned serve to show that the study and modelling of electrode ablation and/or metal vapors in thermal plasma is an ongoing topic of interest in a variety of applications, both in the academia and the industry.

This chapter describes the methodology used in this work to describe the ablation of electrodes and the impact on the arc behavior and plasma properties caused by metal vapor contamination of the medium. Initially, the different source terms used in the governing equations to account for the electrode ablation are described. Then, the species transport equation is introduced along with the combined diffusion coefficients. Thirdly, the equations employed to estimate the evaporated mass from the electrodes are shown. The chapter concludes with a discussion on the impact of metal vapors on the plasma properties.

## 3.2. SOURCE TERMS IN THE GOVERNING EQUATIONS

The effects of the electrode ablation model are included into the governing equations presented in Chapter 1 by means of source terms. The equations concerned are the mass conservation, the energy equation, and the species transport equation described below.

The evaporated material from the electrode is injected into the gas volume as a source term ($S_m$) in the mass conservation equation $(4)$. It is worth mentioning that this source term, and the others described in this section, are applied at the fluid cells adjacent to the fluid/solid interface. As emphasized in [17], [63], [70], the mass source term is important in order to consider the impact on the flow due to vapor production. As the density is increased in the plasma next to the electrode, the pressure will also increase, and that in turn will result in higher plasma velocities to remove the mass originating from the electrode. The mass source term ($S_m$) is expressed as:

$$S_m = \dot{m}\frac{\Delta S}{\Delta V}\,, \tag{42}$$

where $\dot{m}$ is the evaporated mass flux, $\Delta S$ is the surface of the cell face in contact with the interface, and $\Delta V$ is the cell volume. The evaporated mass flux is determined according to section 3.4.

Similarly, a source term is necessary for the energy equation $(8)$ to take into account the enthalpy carried by the metallic vapors into the plasma.

$$S_h = h_T(T_w)\,\dot{m}\frac{\Delta S}{\Delta V}\,, \tag{43}$$

where $h(T_w)$ is the metal vapor enthalpy evaluated at the electrode surface temperature $T_w$ obtained with the model. Another term that can have an impact on the enthalpy field, and that should be considered in the energy equation $(8)$, is the transport of enthalpy due to species diffusion [34]:

$$\nabla \cdot \left[\sum_{j=1}^{N} h_{T\,j}\vec{J_j}\right].$$

It should be noted that alternative formulations, such as the mass fraction boundary condition approach presented in [60] where source terms $(42)$ and $(43)$ are not included, will tend to underestimate the velocities in the direction away from the vaporization source and the enthalpy carried by the metallic vapors. However if the vaporization rates are relatively small, then the result could be considered somewhat accurate [17].

Additional source terms are needed for the species transport equation, but they will be treated in the following section.

### 3.3. THE SPECIES TRANSPORT EQUATION

When modelling thermal plasmas in gas mixtures, the most general approach is to specify a conservation equation for each individual species. In this case, convection-diffusion conservations equations for each species $i$ must be added as follows:

$$\frac{\partial}{\partial t}(\rho Y_i) + \nabla \cdot (\rho \vec{v} Y_i) = -\nabla \cdot \vec{J_i} + S_i\,, \tag{44}$$

where $Y_i$ is the local mass fraction, $J_i$ is the diffusion mass flux, and $S_i$ contains any source terms. The diffusion mass flux of the species $i$ is given then by:

$$\vec{J_\iota} = \frac{m_i n^2}{\rho} \sum_{j=1}^{N} m_j D_{ij} \vec{d_j} - D_i^T \nabla \ln T \,, \tag{45}$$

where $m_i$ is the mass density of species $i$, $n$ is the number density, $\vec{d_j}$ is the driving force term related to the diffusion due to gradients in the species $j$ molar fraction, pressure and external forces acting on the species $j$. $D_{ij}$ and $D_i^T$ are the multicomponent diffusion coefficients, which have to be calculated for each pair of species. This is, $\frac{1}{2} N(N-1)$ ordinary diffusion coefficients ($D_{ij}$) and $N-1$ thermal diffusion coefficients ($D_i^T$) for a gas mixture where N species are present.

This general formulation can represent an enormous challenge to solve, especially when the gas mixtures are composed of an important number of species. Taking as example an argon – copper mixture with $N = 7$ species ($e^-$, $Ar$, $Ar^+$, $Ar^{2+}$, $Cu$, $Cu^+$, and $Cu^{2+}$), then equation (7) must be solved for 6 of those species (namely $N-1$, since the diffusion velocities are defined with respect to the mass average velocity). For the multicomponent diffusion coefficients, it is necessary to calculate 21 ordinary diffusion coefficients and 6 thermal diffusion coefficients. This allows to illustrate the great complexity and computational resources that are required to model the species conservation in a rather simple composition. That is the reason why simplified methods are commonly used for such modellings.

### 3.3.1. The combined diffusion coefficient method

A well-known and used approach is the combined diffusion coefficient method proposed by A. B. Murphy, which allows for major simplifications [71]. Following this approach, all the species in the gas – metal mixture are grouped into their parent gases (“G” corresponding to the plasma gas, and “M” for the metal vapors), and then equation (7) is used to describe each of these gases. The diffusion mass flux of the metal vapor M in its complete form is given by:

$$\overrightarrow{J_M} = -\rho \frac{\overline{m_M}\,\overline{m_G}}{\bar{M}^2}\left(\overline{D_{MG}^{x}}\,\nabla\overline{x_M} - \overline{D_{MG}^{P}}\nabla \ln P - \overline{D_{MG}^{E}}\vec{E}\right) - \overline{D_{MG}^{T}}\nabla \ln T \ , \qquad (46)$$

where $\overline{m_M}$ and $\overline{m_G}$ are the average masses of the heavy species of the metal vapor "M" and the plasma gas "G", respectively. $\bar{M}$ is the average mass of all species in the gas mixture, $\overline{x_M}$ is the sum of the mole fractions of metal species. $\overline{D_{MG}^{x}}$, $\overline{D_{MG}^{P}}$, $\overline{D_{MG}^{E}}$, and $\overline{D_{MG}^{T}}$ are the so-called combined diffusion coefficients. They describe diffusion due to molar fraction gradients ($\overline{D_{MG}^{x}}$), gradients of pressure ($\overline{D_{MG}^{P}}$), external electric fields ($\overline{D_{MG}^{E}}$), and temperature gradients ($\overline{D_{MG}^{T}}$).

Retaking the previous argon – copper example, one can see how the combined diffusion coefficient approach helps to simplify the modelling of metal vapors in the plasma gas. Instead of solving the species conservation equation for 6 individual species, it is now necessary to solve it for either argon or copper as a gas. Similarly, the diffusion coefficients required also decrease from 21 ordinary diffusion coefficients and 6 thermal diffusion coefficients with the multicomponent approach to only 4 combined diffusion coefficients. Such simplifications make the study of metal vapors in plasmas more accessible in terms of computational resources and calculation time once the 4 combined diffusion coefficients are known.

The combined diffusion coefficient approach is equivalent to the full multicomponent diffusion coefficient method under three conditions [48]:

1) The mixture is in the state of local chemical equilibrium, which is valid if local thermodynamic equilibrium is assumed.
2) The gases are homonuclear (the molecules are made from atoms of a single element).
3) The gases do not react with each other.

For mixtures including air, such as air-copper, the gases are heteronuclear and some of the species present react with each other. However, it is still possible to calculate the combined diffusion coefficient for these cases with relatively small errors.

The equation $(46)$ representing the mass diffusion flux of metallic vapors in a gas is the original form presented by A.B. Murphy, where the ordinary diffusion is expressed in terms of the molar fraction gradient ($\nabla\overline{x_M}$). However, most computational fluid dynamic codes require this term to be written as a function of the mass fraction gradient ($\nabla\overline{Y_M}$), thus equation $(46)$ needs to be modified [72]. The molar fraction gradient can be written as:

$$\nabla \overline{x_M} = \frac{\bar{M}}{\bar{M}_M} \nabla \overline{Y_M} + \overline{Y_M} \nabla \left( \frac{\bar{M}}{\overline{M_M}} \right) \ , \tag{47}$$

where $\bar{M}$ is the average mass of all the species in the gas mixture and $\bar{M}_M$ is the average mass of all the species of metal vapor. Therefore,

$$\overrightarrow{J_M} = -\rho \frac{\overline{m_M}\,\overline{m_G}}{\bar{M}\,\bar{M}_M} \overline{D_{MG}^x}\, \nabla \overline{Y_M} - \rho \frac{\overline{m_M}\,\overline{m_G}}{\bar{M}^2} \overline{D_{MG}^x}\, \overline{Y_M}\, \nabla \left( \frac{\bar{M}}{\overline{M_M}} \right) + \rho \frac{\overline{m_M}\,\overline{m_G}}{\bar{M}^2} \overline{D_{MG}^P} \nabla \ln P + \rho \frac{\overline{m_M}\,\overline{m_G}}{\bar{M}^2} \overline{D_{MG}^E} \vec{E} - \overline{D_{MG}^T} \nabla \ln T \ . \tag{48}$$

By substituting equation $(48)$ in $(44)$, we have the complete form of the species conservation equation for a metal vapor "M" in a plasma gas "G", with the mass diffusion flux expressed in terms of the mass fraction gradient.

$$\frac{\partial}{\partial t}(\rho \overline{Y_M}) + \nabla \cdot (\rho \vec{v} \overline{Y_M}) = \nabla \cdot \left( \rho \frac{\overline{m_M}\,\overline{m_G}}{\bar{M}\,\bar{M}_M} \overline{D_{MG}^x}\, \nabla \overline{Y_M} \right) + \nabla \cdot \left( \rho \frac{\overline{m_M}\,\overline{m_G}}{\bar{M}^2} \overline{D_{MG}^x}\, \overline{Y_M}\, \nabla \left( \frac{\bar{M}}{\overline{M_M}} \right) \right) - \nabla \cdot \left( \rho \frac{\overline{m_M}\,\overline{m_G}}{\bar{M}^2} \overline{D_{MG}^P} \nabla \ln P \right) - \nabla \cdot \left( \rho \frac{\overline{m_M}\,\overline{m_G}}{\bar{M}^2} \overline{D_{MG}^E} \vec{E} \right) + \nabla \cdot \left( \overline{D_{MG}^T} \nabla \ln T \right) + S_M \ . \tag{49}$$

According to this form, the first term on the right-hand side is treated as the diffusion term in the transport equation. The second, third, fourth, and fifth terms are then considered as source terms. Finally, the last term ($S_M$) correspond to the metal vapor coming from the electrodes due to vaporization, and it is equal to $(42)$.

### 3.3.2. Combined diffusion coefficients for an air – copper mixture

This section presents the combined diffusion coefficients for an air – copper mixture used in this work as an input. They were calculated by the SciPRA team from the Laplace laboratory (France), based on A.B. Murphy's theory [73]. Figure 42 to Figure 45 show the coefficient values at 1 bar for different temperatures and mass metal concentrations. Explanations on the behavior of the different combined diffusion coefficients can be found in [71], [74].

For example, Figure 42 shows the combined ordinary coefficient for an air-copper mixture at 1 bar and different mass metal concentrations. A peak in the coefficient is observed at temperatures lower than 10000 K, however the temperature for the maximum varies according to the concentration. It is explained in [73] that this dependency is indirect and is attributed to the influence of the gas proportions on the ionization degree of the plasma: at low temperatures the coefficient rises due to the diffusion between neutral particles, while at high temperatures Coulombian interactions reduce the mobility of electrons and ions decreasing the diffusion.

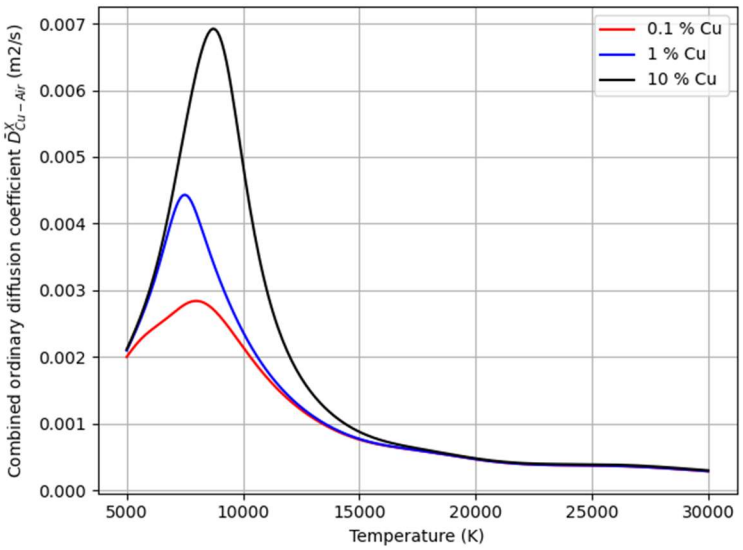


Figure 42. Combined ordinary diffusion coefficient at 1 bar.

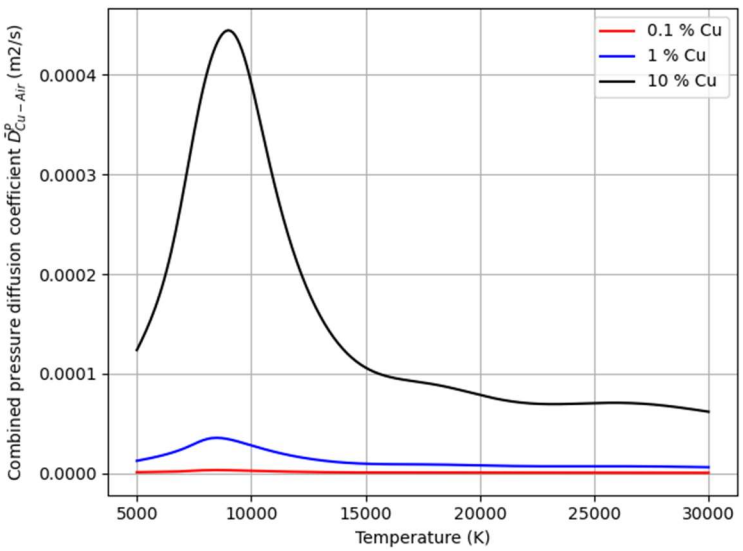


Figure 43. Combined pressure diffusion coefficient at 1 bar.

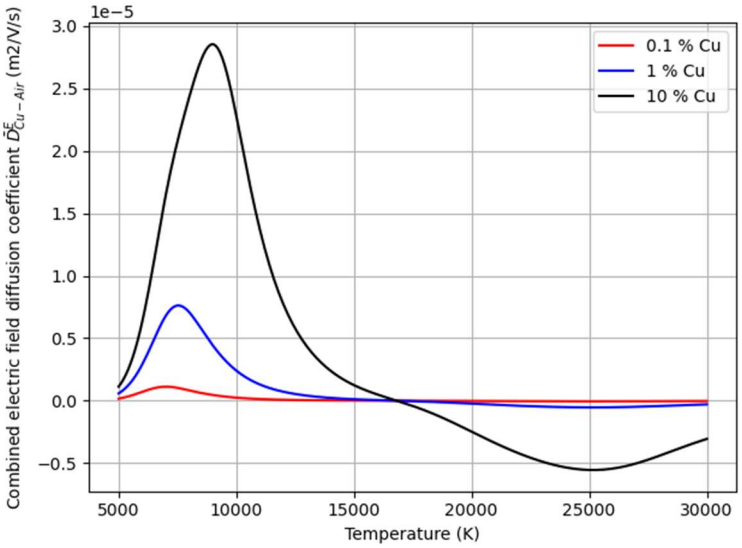


Figure 44. Combined electric field diffusion coefficient at 1 bar.

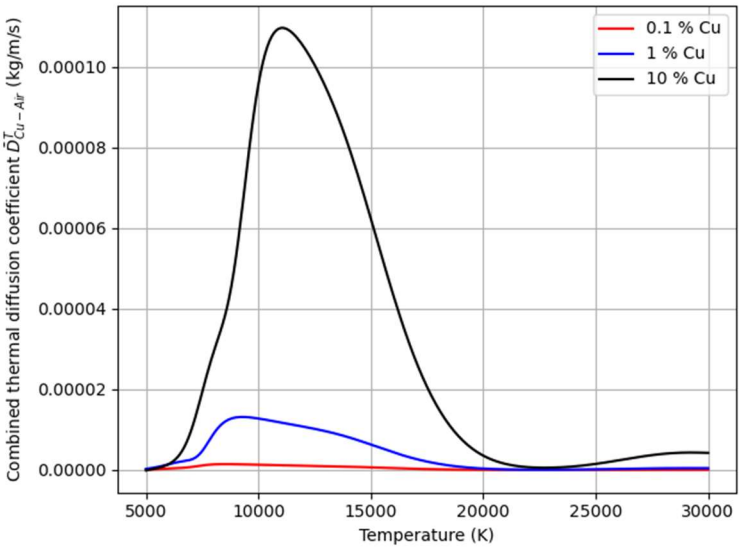


Figure 45. Combined thermal diffusion coefficient at 1 bar.

## 3.4. ELECTRODE ABLATION

There exist several methods to estimate the mass flux of ablated electrode material. Two of the most common are the energy flux approach and the pressure vapor approach. Once it has been determined, it can be used to compute the source terms ($S_m$) and ($S_h$) presented in section 3.2.

### 3.4.1. Energy flux approach

According to the energy flux approach, the evaporated mass flux can be determined as the ratio between the incident energy flux at the surface ($q_w$) estimated by the model, and the total enthalpy needed to evaporate the electrode material ($H_T$).

$$\dot{m} = \frac{q_w}{H_T} \ . \tag{50}$$

This approach is valid in applications with very high energy fluxes that result in instant vaporization. However, it presents the inconvenience of neglecting the cooling of the metal due to conduction [17].

### 3.4.2. Vapor pressure approach

The alternative approach uses the pressure vapor to estimate the ablated mass flux. The metal pressure vapor ($P_v$) at the interface electrode – plasma is calculated according to the Clausius – Clapeyron equation:

$$P_v = P_{atm} \exp\left(-\frac{H_{vap}}{R}\left(\frac{1}{T_w} - \frac{1}{T_{boil}}\right)\right), \tag{51}$$

where $P_{atm}$ is the atmospheric pressure, $H_{vap}$ is the molar heat of vaporization, $R$ is the ideal gas constant, and $T_{boil}$ is the boiling temperature of the electrode material. $T_w$ is the temperature at the electrode surface estimated by the model.

The mass flux is then determined by using the Hertz – Knudsen – Langmuir equation. In its simplest form:

$$\dot{m} = \left(\frac{m_M}{2\pi k_B T_w}\right)^{1/2} P_v \, , \tag{52}$$

where $m_M$ is the atomic mass of the metal vapor, and $k_B$ is the Boltzmann constant. The vapor pressure and vaporization mass flux calculated with equations $(51)$ and $(52)$ for different metals common in low voltage switching devices are shown in Figure 46 and Figure 47, with the material properties summarized in Table 4.

Table 4. Thermodynamic properties for several metals.

| **Metal** | $H_{vap}$ (J/mol) | $T_{boil}$ (K) | $m_M$ (kg) |
|---|---|---|---|
| Ag | $255 \cdot 10^3$ | 2435 | $1.791 \cdot 10^{-25}$ |
| Cu | $300.3 \cdot 10^3$ | 2868 | $1.055 \cdot 10^{-25}$ |
| Fe | $347 \cdot 10^3$ | 3134 | $9.2733 \cdot 10^{-26}$ |
| W | $800 \cdot 10^3$ | 5828 | $3.0527 \cdot 10^{-25}$ |

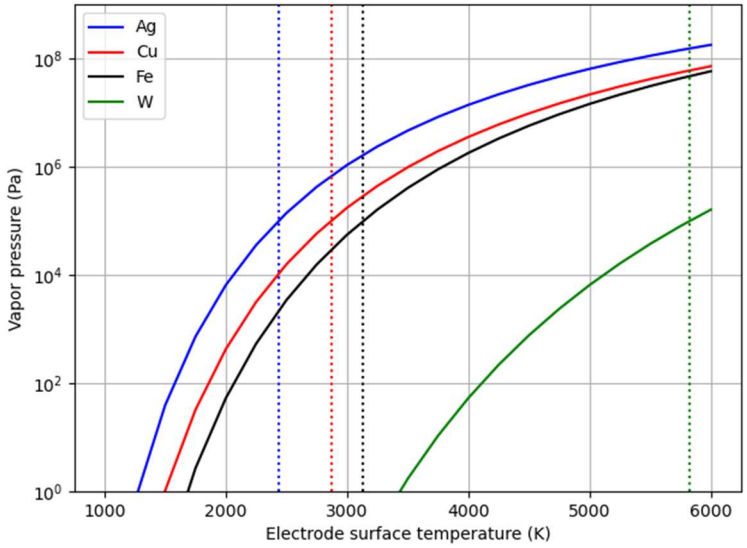


Figure 46. Vapor pressures at different wall temperatures.

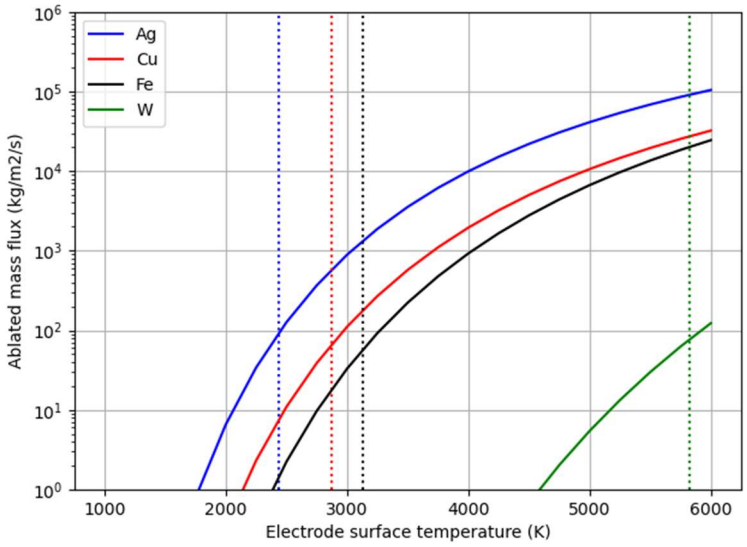


Figure 47. Ablated mass flux at different wall temperatures.

From the graphs, it follows that materials with lower molar heat of vaporization and boiling temperature have higher vapor pressures and ablated mass flux. For any given temperature, then silver presents the highest values of these quantities, followed by copper and iron. Refractory materials, as tungsten, have much lower values of vapor pressure and ablated mass flux, even by several orders of magnitude.

The mass flux calculated with equation $(52)$ corresponds to the case of vaporization in vacuum, where effects such as the ambient gas pressure or backscattering due to atoms collisions close to the surface do not limit the vaporization rate. Therefore, it represents the maximum mass flux at a given electrode surface temperature.

The equation $(52)$ has also been modified to include these effects. For example, a coefficient $\beta_R$ can be introduced to account for the fraction of evaporated mass that re-condensates at the surface after interacting with the surrounding gas. Values of $\beta_R$, called the retro-diffusion coefficient, can go from 0.17 for high evaporation rates to 1 when the metal temperature is relatively low [45].

$$\dot{m} = (1 - \beta_R)\left(\frac{m_M}{2\pi k_B T_w}\right)^{1/2} P_v \,. \tag{53}$$

M. Shibayama also proposes an expression to calculate the ablated electrode metal considering not only the ablation flux, but also the re-deposition flux onto the electrode surface [75]:

$$\dot{m} = \left(\frac{m_M}{2\pi k_B T_w}\right)^{\frac{1}{2}} P_v - \rho\overline{Y_M}\left(\frac{k_B T_{pl}}{2\pi m_M}\right)^{\frac{1}{2}}, \tag{54}$$

where $T_{pl}$ is the gas temperature calculated by the model at the interface.

Similarly, more complicated formulations exist to consider the effects of the ambient gas. For instance, the pressure and temperature of the ambient gas are added to the Langmuir equation in [76]:

$$\dot{m} = \left(\frac{m_M}{2\pi k_B}\right)^{1/2}\left(\sigma_e \frac{P_v}{T_w^{1/2}} - \sigma_c \frac{P_\infty}{T_\infty^{1/2}}\right), \tag{55}$$

where $P_\infty$ and $T_\infty$ correspond to the pressure and temperature of the surrounding gas, respectively. Two coefficients are also introduced: an evaporation coefficient ($\sigma_e$) and a condensation coefficient ($\sigma_c$), which are usually equal and close to one, although ($\sigma_c$) could be lower due to the reflection of non-condensing species [76]. However, complex formulations such as $(54)$ and $(55)$ are seldom used for switching applications, as is the retro-diffusion coefficient. Therefore, in this work ablated mass are estimated following equation $(52)$.

### 3.4.3. Test case of the electrode ablation model

Since the Langmuir equation $(52)$ gives the vaporization in vacuum, and thus represents the maximum mass flux at a given surface temperature, it may result in an overestimation of the evaporated mass and affect the cathode temperature calculation. To better understand the impact of the evaporation limitation due to higher pressures, a simple case of the heating of an electrode is studied. Equation $(53)$ is used to estimate the ablated mass flux, as it also serves to observe the influence of the retro-diffusion coefficient ($\beta_R$) on the electrode temperature and total ablated mass. This case corresponds to a cylindrical electrode made of silver, with a height of 6 mm and a radius of 4 mm.

The electrode is heated at the top surface by an imposed heat flux ($q_{arc}$), and it is cooled down once evaporation takes place ($q_{evap}$). So, the energy flux at the surface ($q_w$) is:

$$q_w = q_{arc} - q_{evap} \,. \tag{56}$$

The energy flux heating the surface for this study was chosen to represent the arc-electrode interaction in a low voltage switching device. If one considers that the arc is uniformly heating the electrode in the attachment zone, then:

$$q_{arc} = \begin{cases} j_0 \cdot U_h & if \quad r \leq r_{att} \\ 0 & if \quad r > r_{att} \end{cases}, \tag{57}$$

Where $j_0$ is the current density at the interface, and $U_h$ is the heating voltage. These parameters are taken as constants equal to $2 \cdot 10^8 \, A/m^2$ and $6 \, V$, respectively. To define region where $q_{arc}$ is applied, the attachment radius ($r_{att}$) is calculated considering an AC current wave:

$$r_{att} = \sqrt{\frac{I\sqrt{2}\sin(2\pi f t)}{2\pi j_0}} \,, \tag{58}$$

Where $I$ is the nominal current, and $f$ is the frequency. The heat losses due to metal ablation are given by:

$$q_{evap} = \dot{m} L_v \,, \tag{59}$$

Where $L_v$ is the metal specific heat of vaporization.

The problem is solved for 10 ms and modelled as a 2D axisymmetric case in COMSOL Multiphysics 6.1 using a time-dependent fully-coupled solver.The bottom surface of the electrode is maintained at constant temperature (300 K) and the lateral wall is adiabatic. As initial condition, the temperature at the surface where the heat flux is applied is set to the melting temperature of silver (1235 K). The conditions are illustrated in Figure 48:

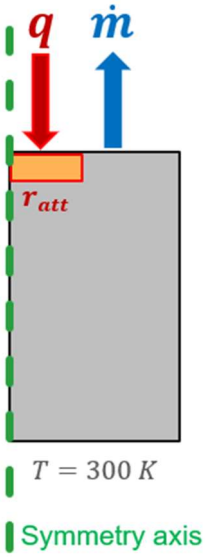


Figure 48. Description of the electrode heating case.

***Results***

The results are presented for a nominal current ($I$) set to 2000 A and a retro-diffusion coefficient ($\beta_R$) equal to 0, corresponding to equation $(52)$ chosen in our study case. Figure 49 shows the temperature evolution at the center of the electrode top surface. The temperature increases from the initial value (1235 K), passing the silver boiling temperature (2435 K) at 7 ms, to a maximum of 2880 K. This will in turn cause the vaporization of the electrode material, which is presented in Figure 50 as the integration of the ablated mass flux along the surface. From Figure 50 it can be seen that the ablated mass rate begins to increase around 4 ms, and reaches a maximum value of $2.65 \cdot 10^{-5}$ kg/s at 9 ms. The evolution of the ablated mass is shown in Figure 51, where the total ablated mass after the 10 ms calculated adds to $6 \cdot 10^{-8}$ kg.

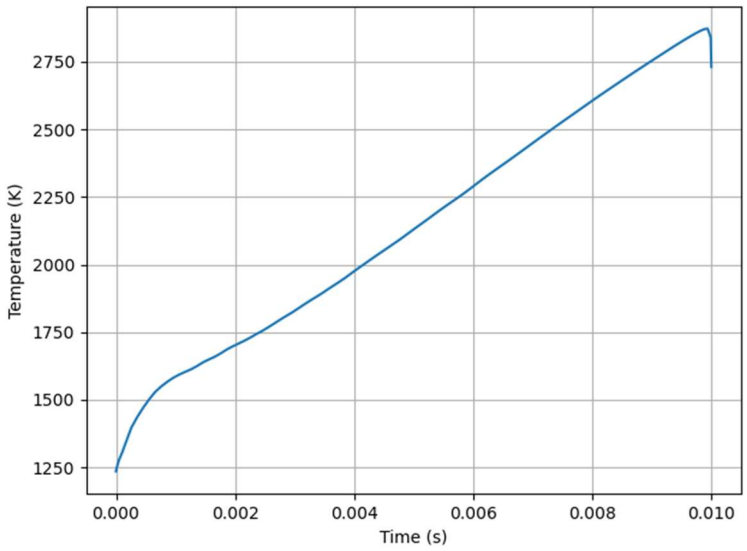


Figure 49. Temporal evolution of temperature at the center of the top surface.

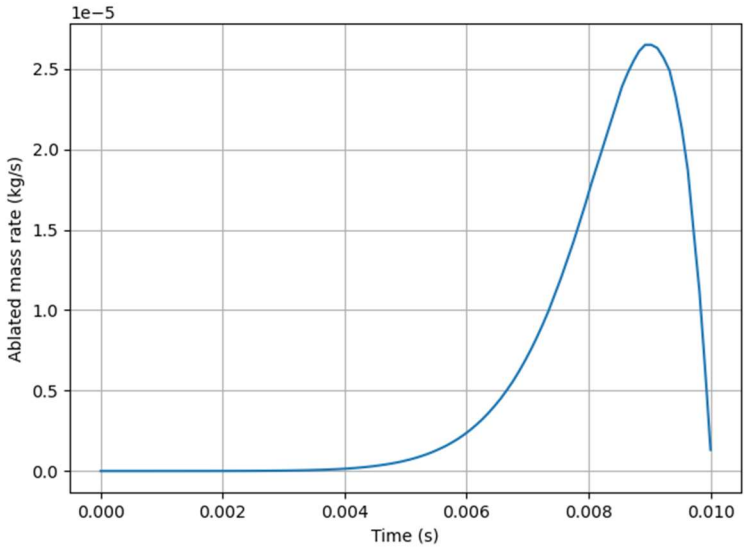


Figure 50. Temporal evolution of the total ablated mass rate.

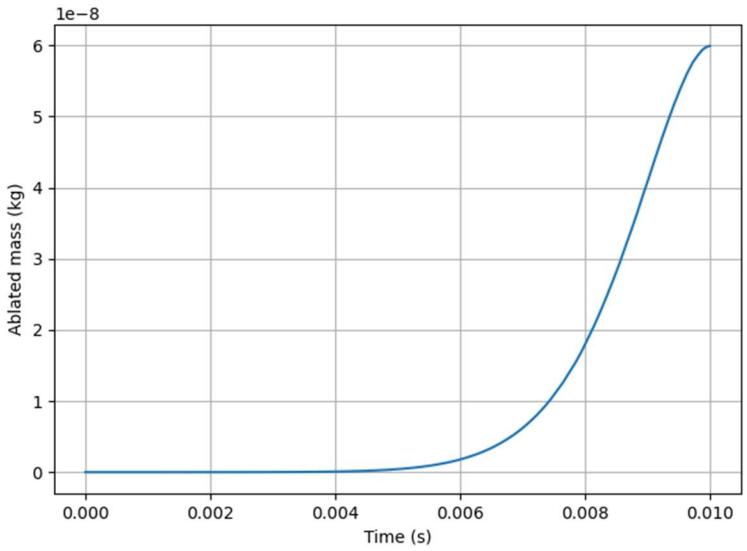


Figure 51. Temporal evolution of the total ablated mass.

Similar calculations can be performed varying the different parameters to see their impact on the results. Several values of nominal currents (500 A, 1000 A, 2000 A, 3000 A) and retro – diffusion coefficients (0, 0.17, 0.5, 1) were used to conduct the parametric study.

The maximum temperature reached in each case is plotted in Figure 52. At low nominal current (500 A), the temperature at the surface reaches a maximum around 2520 K for all the cases despite the change in the retro – diffusion coefficient ($\beta_R$). As the nominal current is increased, the influence of $\beta_R$ becomes somewhat more evident. The electrode has a maximum temperature of 2920 K for a nominal current equal to 3000 A and a $\beta_R$ of 0, contrasting to a maximum temperature of 2990 K for the same current but with $\beta_R = 1$. However, this represents only a variation of 2.4% in the maximum temperature reached in the electrode.

Figure 53 and Figure 54 present the maximum flow of ablated mass and the total mass losses for each case. When $\beta_R$ is set to 0, the total ablated mass rate goes from a maximum of $1.7 \cdot 10^{-6}$ kg/s at 500 A to $4.78 \cdot 10^{-5}$ kg/s for 3000 A. Similarly, the mass loss when $\beta_R$ = 0 starts at $4 \cdot 10^{-9}$ kg for 500 A and increases to $1.5 \cdot 10^{-7}$ kg at 3000 A. As expected, the increase of the retro – diffusion coefficient ($\beta_R$) will directly impact the mass flow and total mass loss. For example, at 3000 A the total ablated mass rate decreases to $4.03 \cdot 10^{-5}$ kg/s when $\beta_R$ = 0.17, and to $2.5 \cdot 10^{-5}$ kg/s for $\beta_R$ = 0.5. Regarding the total ablated mass, it falls to $8.9 \cdot 10^{-8}$ kg for a $\beta_R$ of 0.17 and to $5.5 \cdot 10^{-8}$ kg when $\beta_R$ equal to 0.5.

This example illustrates how the ablation model is used to calculate the metal losses in the electrodes. It also shows how the cooling effects due to the electrode ablation has a minor impact on the temperature calculation under the conditions set for this case, and how the retro – diffusion coefficient ($\beta_R$) directly affects the quantity of mass ablated from the electrode. As mentioned before, the following of this work uses equation $(52)$.

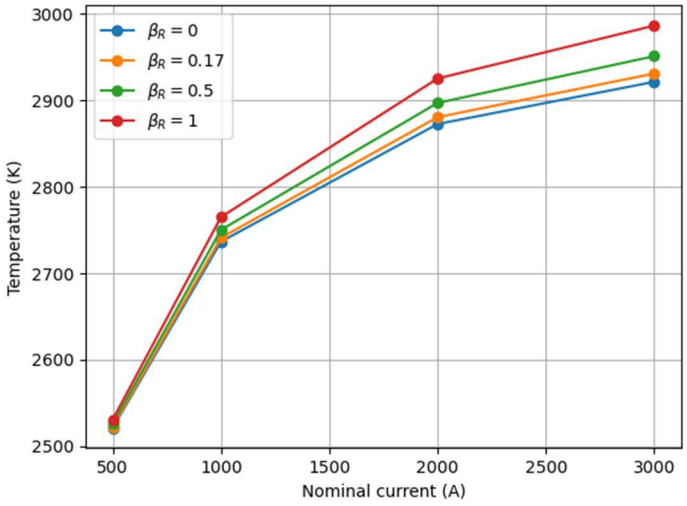


Figure 52. Maximum temperature reached.

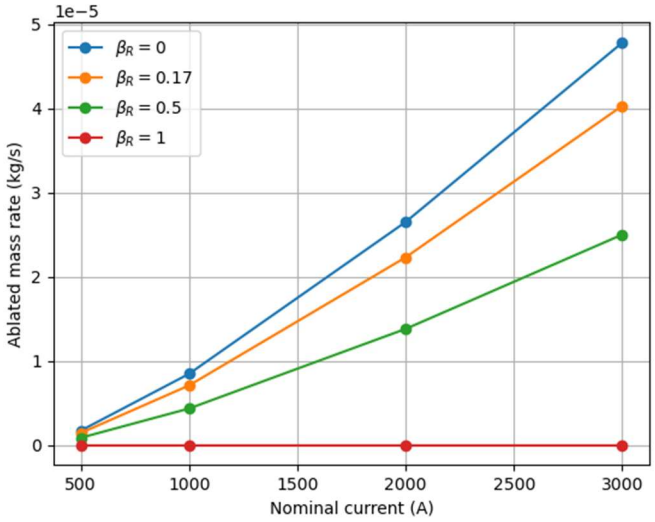


Figure 53. Maximum ablated mass rate.

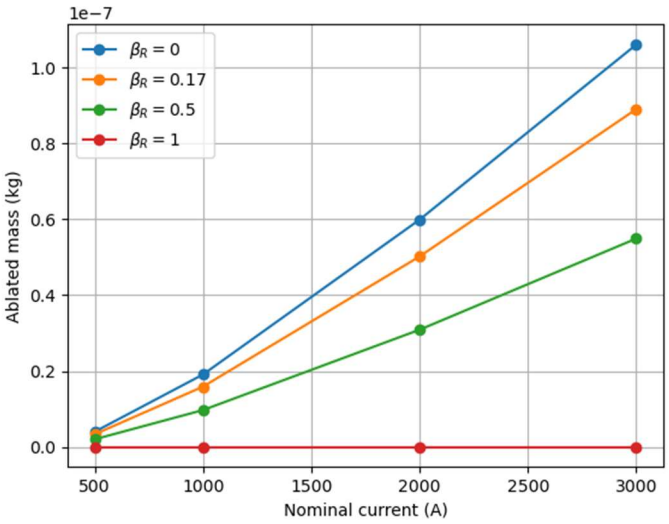


Figure 54. Total ablated mass.

### 3.5. EFFECTS OF METAL VAPORS ON THE PLASMA PROPERTIES

The effects that metal vapors have on the arc are essential and must be taken into account when modelling processes include electrode ablation. The presence of metal vapors will influence the arc, as a consequence of its impact on the thermodynamic, transport and radiative properties of the plasma [40]. This is especially true at low to intermediate temperatures (lower than 10000 K), where even a small amount of metal vapors can cause an increase in the electrode number density ($n_e$) in the plasma due to the lower ionization energies of metal species with respect to the gas components [77].

Properties such as the radiation emission of the plasma are affected by the rise of $n_e$. A good example of this is the net emission coefficient for an air – copper mixture, shown in Figure 55. The figure shows three curves for different copper mass fractions at 1 bar and a plasma radius ($R_p$) of 1 mm: 0% Cu (pure air), 1 % Cu, and 100 % Cu. For the temperature range plotted, the highest values of radiation losses correspond to the 100 % Cu curve, while the lowest values belong to the pure air gas. It is also interesting to compare the curves for pure air and air with 1% Cu. One can note how below 10000 K, the radiation losses represented by the net emission coefficient are substantially increased by adding a small amount of copper. At 6000 K for example, 1% of copper accounts for an increment of one order of magnitude. However, the difference between the two curves is reduced at temperatures above 10000 K.

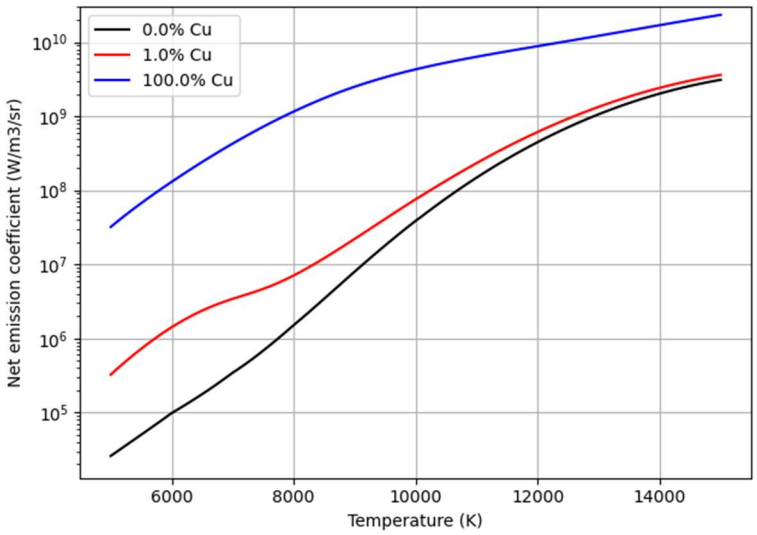


Figure 55. Net emission coefficient of an air - copper mixture at a pressure of 1 bar and $R_p = 1\,mm$.

A similar behavior is observed in Figure 56 describing the electrical conductivity evolution with temperature for the same air – copper mixture. The highest values at temperatures lower than 15000 K correspond to 100 % Cu and the lowest values to the pure air plasma. At temperatures below 9000 K, the presence of 1 % Cu in the mixture causes an increase in the electrical conductivity, but this increment is considerably reduced for higher temperatures. However, it is important to note that the general trend presented in Figure 56 is inversed after 16000 K, meaning that the electrical conductivity for pure air is higher in this temperature range than that of 100 % Cu. This behavior is attributed to a change in the main elastic collisions involving electrons, as discussed in [78].

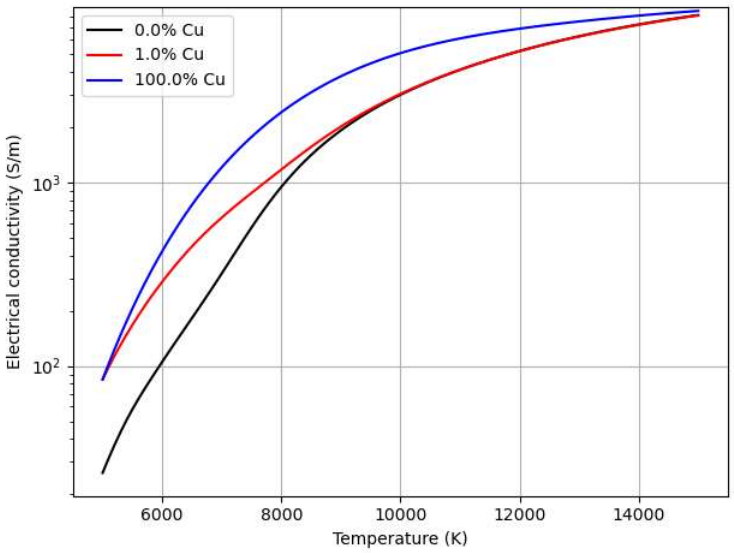


Figure 56. Electrical conductivity of an air - copper mixture at a pressure of 1 bar.

Other plasma properties are also affected by the metallic vapors, although they may be less sensible to small amounts of metal. One example of this is the specific heat at constant pressure ($C_P$) presented in Figure 57. The pure air curve has the highest $C_P$ values overall in the entire temperature range (5000 K to 30000 K) due to the peaks of molecular dissociation and ionization, while the 100 % Cu curve shows in general lower values of $C_P$ with less pronounced peaks. In contrast to the net emission coefficient and the electrical conductivity, a mixture with 1 % Cu does not result in a noticeable change in the $C_P$, as the two curves superpose. It is necessary to have a higher metal mass fraction in the mixture in order to start observing some variation in the $C_P$. Figure 57 shows how a 10 % Cu mixture will lead to slightly lower values of $C_P$ compared to pure air.

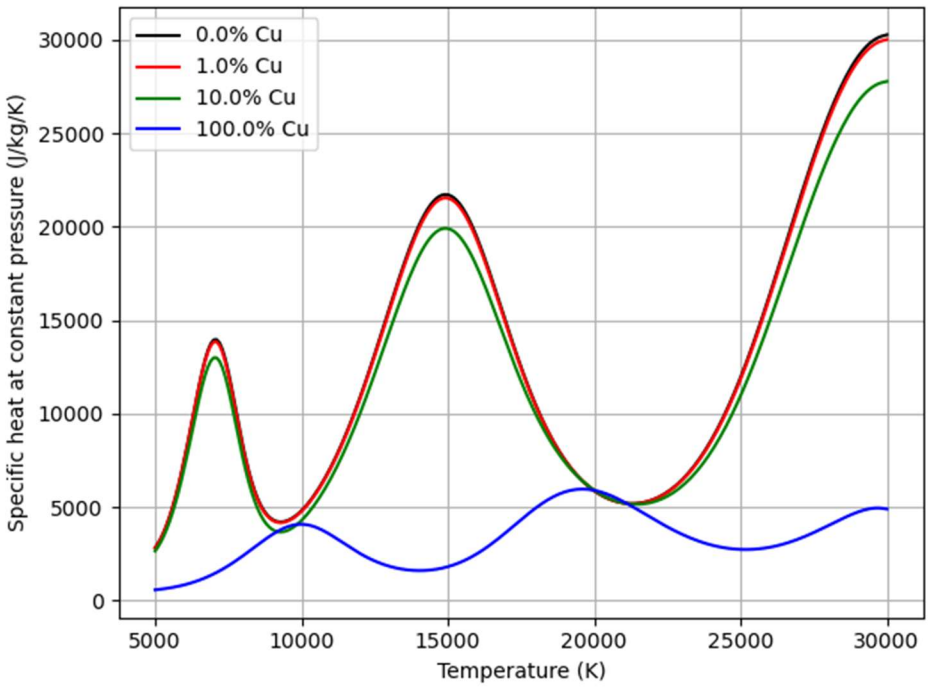


Figure 57. Specific heat at constant pressure of an air - copper mixture at a pressure of 1 bar.

The previous examples of net emission coefficient, electrical conductivity, and specific heat at constant pressure serve to show the impacts that the metal vapors have on the plasma properties. They also demonstrate that the property variations with the metal mass fraction can be complex and differ from one property to another. Therefore, a question is raised as to what method should be used to determine the plasma properties in a gas – metal mixture in arc modellings. Three main approaches are usually followed to this end [79].

The first approach is to directly calculate the mixture properties at each time and each position in the domain while the model is computed, e.g. [80]. This approach has been used for quasi-thermal plasmas where the composition is not in equilibrium. However, it has the disadvantage of being complex, time consuming and requiring considerable computational resources.

Another approach is to apply mixing rules to get the mixture properties from pure gases' properties. This is an attractive alternative since pure gas properties are easy to obtain, the implementation of mixture rules is simple, and its execution is fast; thus, it is useful to obtain a rough approximation of the system behavior, especially in industrial codes. Yet, some caution must be taken when using this approach as the exact mixing rules to be applied change depend on each property and the temperature range. Figure 58 compares the exact result for $C_P$ in an air – copper mixture with those calculated following two mixing rules: mass proportion-

based interpolation and molar proportion-based interpolation. It shows that the mixing rule based on the mass proportion gives better results than the molar one, and the results are quite satisfactory for this particular mixture, except maybe in the range of 10000 K and 12500 K where some discrepancies can be observed with respect to the exact solution. The thermal conductivity calculated with mixing rules also presents the difficulties as the specific heat at constant pressure, this due to the chemical reactions that can exist between the two gases [79]. However, the use of mixing rules can lead to good approximations in case of other properties as electrical conductivity, viscosity, and the net emission coefficient. Whether the mixing rules approach is valid or not will depend on the specific objective of each application.

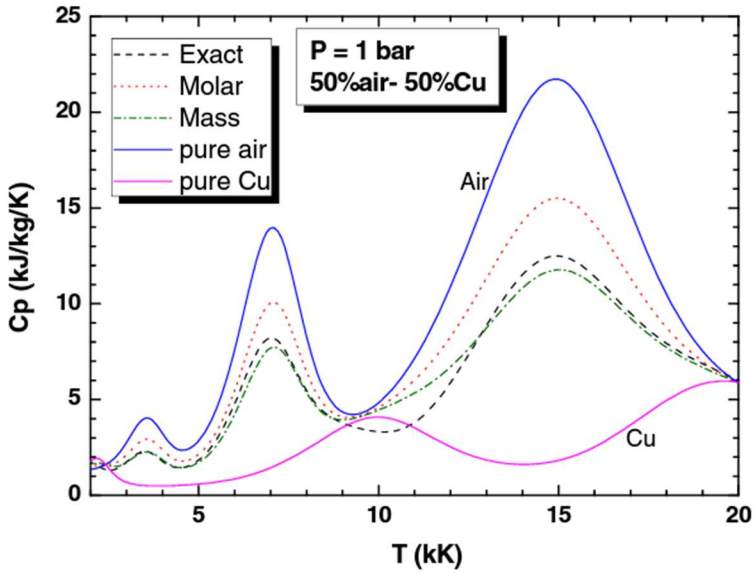


Figure 58. Comparison of exact and mixing rules approach for the specific heat at constant pressure in an air - copper mixture. Source: [79]

The third approach consists of the use of tabulated data created from previously calculated properties. The plasma properties are given as functions of several parameters, such as pressure, mass fraction, and temperature; and then the tables are interpolated to obtain the exact value. As a downside, it requires an extensive calculation of properties over a large range of parameters that can result in a large dataset. This is the approach used in this work as it is rather rigorous, and it is also the most common method for metal vapors modelling in thermal plasmas.

## 3.6. SUMMARY

In this chapter, the approach used to implement the vaporization of the electrode material and its effects on the arc is presented. Initially, the source terms needed to account for the mass injection and its respective enthalpy in the governing equations are introduced. Then, a transport equation to follow the metal concentration is added to the system of equation to follow the metal vapors in the gas volume. A special emphasis is done on the diffusion term of the species transport equation, where it was shown that the use of the combined diffusion coefficients simplifies greatly the calculation. On the electrode, the Clausius – Clapeyron and the Langmuir equations are used to estimate the ablated mass in the electrode, which depends on the electrode material properties and the surface temperature. Since it represents the vaporization under vacuum conditions, a simple cylinder heating study was performed to observe how the introduction of a coefficient limiting the evaporated mass will affect the temperature in the solid, however it was found to be of little impact on the temperature while directly affecting the ablated mass. The chapter finished with a short discussion on the effects that the metal vapors have on the plasma properties and the different methods that have been used to introduce it in the arc model. The interpolation of values from a property database for a wide range of temperatures, pressures, and metal mass concentration is used in this work.

# CHAPTER 4. LOW VOLTAGE SWITCHING APPLICATIONS

## 4.1. INTRODUCTION

The purpose of this chapter is to apply the different models described throughout this work on a configuration that is representative of low voltage switching applications. The electrode ablation model, described in Chapter 3, is therefore included in the magnetohydrodynamic set of equations presented in Chapter 2 to have a complete description of the electric arc, the impact it has on the electrodes, and how it is affected by the presence of metal vapors.

The chapter presents an arc after the separation of two contacts, which is typical of industrial contactors. An experimental study is performed on this configuration, and then it is modelled using the magnetohydrodynamic approach.

## 4.2. ARC DURING THE OPENING OF CONTACT

### 4.2.1. Case description

This case corresponds to the opening of contacts under an electric load, which resembles the typical configuration of contactors. The electrodes are connected to an electric circuit, in series with an AC voltage source, an inductor, and a variable resistor. The electric circuit is illustrated in Figure 59.

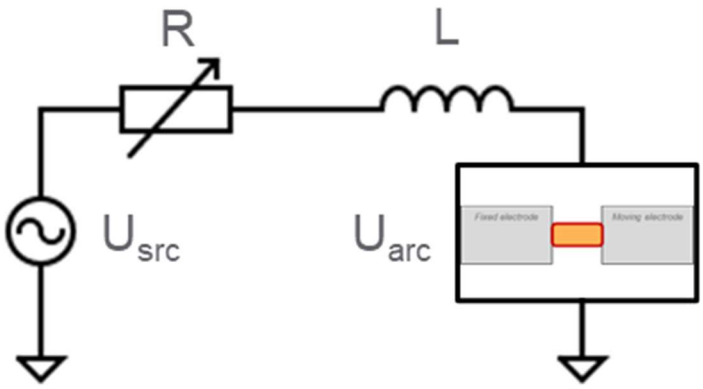


Figure 59. Electric circuit representation of the contact separation case.

When two contacts separate, and provided that the current and voltage are higher than some minimum values, an arc is created [81]. These minimum values are required to sustain

the electron supply from the cathode, in the case of silver, they have been estimated to be $I_{min} = 0.37 - 0.4\ A$, and $U_{min} = 12\ V$, the values for other electrode materials are reported in [7]. The contact opening process is depicted in Figure 60, and is as follows: two cylindrical electrodes are initially in closed position, where their front faces are in contact, and some current is passing through. One of the electrodes has a fixed position, while the other can move in the axial direction. Then, a command is given to the moving contact, and it starts to drive away from the fixed electrode. During the initial instants, the surface in contact is reduced and the ohm heating increases, a molten metal bridge is produced connecting the two electrodes. As the electrodes continue to separate, the bridge breaks close or above the boiling temperature, the space between the electrodes is filled by metal vapors, and a metal arc is formed. Finally, the surrounding gas starts filling the interelectrode gap, and the ambient gas arc is stablished until it extinguishes. More details on the electrode separation can be found in [81] and references therein.

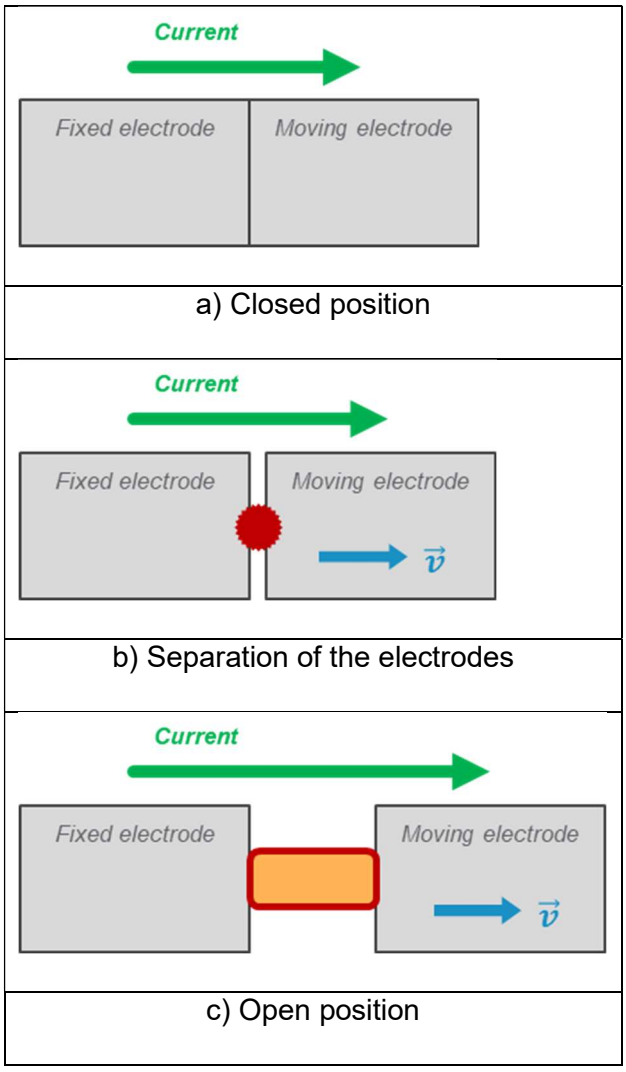


Figure 60. Contact opening process.

The goal of this case is to have a numerical model to study the arc after the contact separation. As a first step, an experimental study was conducted to investigate the behavior of the arc and its effects on the electrodes. The results obtained experimentally are then used to compare with those from the numerical model and have a first validation of the model.

### 4.2.2. Experimental study

#### *Experimental setup*

The experimental study was performed in a device used to characterize the electrical endurance of electrode materials. It consists of a fixed electrode, a moving electrode, a linear actuator to drive the moving electrode, and a spring that links the moving electrode to the linear actuator. This experimental setup is shown in Figure 61. The device is connected to an electrical network, similar to the one presented in Figure 59. The power supply is an AC voltage source of 230 $V_{RMS}$ and 50 Hz. The resistor and inductor are adjusted to guarantee a current of 600 $A_{RMS}$ and a power factor of $\cos(\phi) = 0.35$. The electrodes were made of $AgSnO_2$, their shape was cylindrical with a radius of either 2.5 mm or 4 mm, and a height of 8 mm.

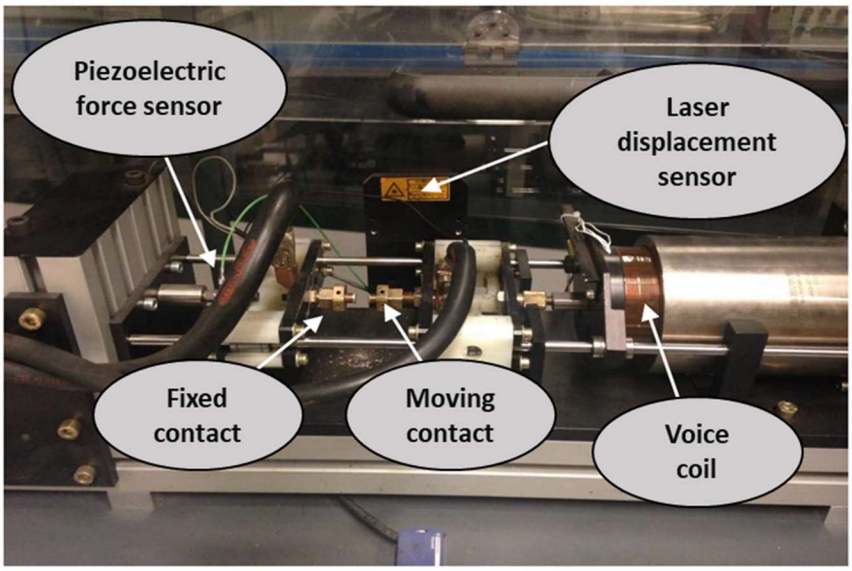


Figure 61. Photograph of the experimental setup.

The classical contact opening operation is as follows: firstly, the two electrodes are disconnected from the electric network and in open position. Then, the moving electrode is put in contact with the fixed electrode by the actuator with a contact force of 10 N. After the electrode are in contact, the device is connected to the network and electric current starts circulating through the system. At a predefined time, the linear actuator pulls the moving

electrode, and an arc is formed. The electric arc remains between the electrodes until it is extinguished at the zero current point or reignites for another half current wave. After the current is interrupted, the device is disconnected again from the electric network and the electrodes stay at the open position.

The operation of the device is controlled by an PID controller based on parameters such as: the moving electrode opening and closing speed, the arc duration, the interelectrode separation, among others. The arc voltage and arc current are measured at each operation, as is the moving electrode carrier displacement by a laser sensor. A high-speed camera is also employed to record the arc throughout the operation. Additionally, a microscope is used to observe the electrode surface and the damage caused by the arc on it.

### *Results*

*Tests with one arc*

The first group of tests corresponds to the cases where there is not reignition of the arc, meaning that the arc is extinguished after the first passing through the zero current.

The oscillogram shown in Figure 62 presents measurements of arc voltage, arc current, and displacement of the moving electrode carrier for a single arc test with an electrode opening velocity of 0.53 m/s. Initially, the electrodes were in the closed position and current is flowing through the system. The electrodes started separating at 17 ms, when the current is 800 A. At the separation, the arc voltage jumped to 16.1 V, mainly due to the sum of the near-electrode voltage drops. One must note that the displacement curve shows an electrode carrier displacement of 2.8 mm, but this corresponds to the elongation of the spring that is initially compressed to apply the contact force. The arc lasted for approximately 4.2 ms, with the arc voltage increasing slightly to a value of 22 V as the voltage drop in the arc column rises with the interelectrode distance, and it finally extinguished at 21.2 ms.

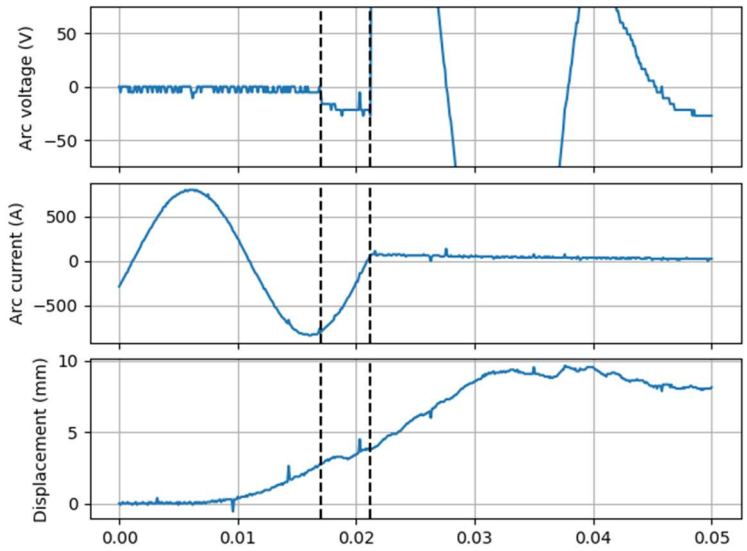


Figure 62. Oscillogram of a single arc test.

The high-speed camera was also used during the test to record the arc behavior with a sample rate of 24000 fps and an exposure time of 10 µs. Figure 63 shows a sequence of the images obtained at four different times: 18 ms, 19 ms, 20 ms, and 21.1 ms.The arc is represented by the high luminosity regions in the frames, and it can be seen how the arc is formed at the center of the electrode surfaces, grew as the electrode separated, remained stable at the center position, and then extinguished.

This is further confirmed by images of the electrode surface taken after the test under a microscope and presented in Figure 64. The traces left by the arc on the electrodes are located at the center, they have a circular shape and an approximate radius of 1.5 mm. Both electrodes showed signs of melting at the surface, but a stronger effect was observed on the fixed electrode (acting as anode).

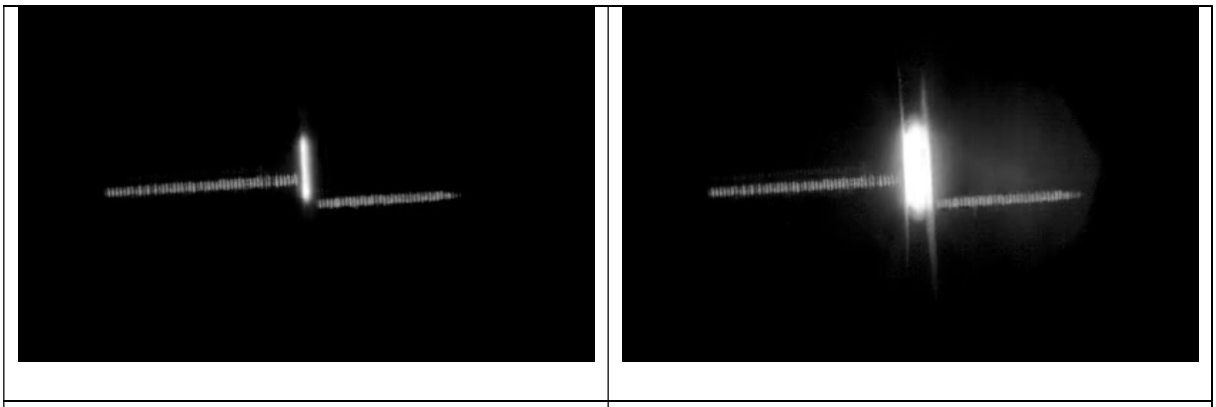

a) $t = 18\,ms$ | b) $t = 19\,ms$

c) $t = 20\,ms$ | d) $t = 21.1\,ms$

Figure 63. Image sequence of a single arc.

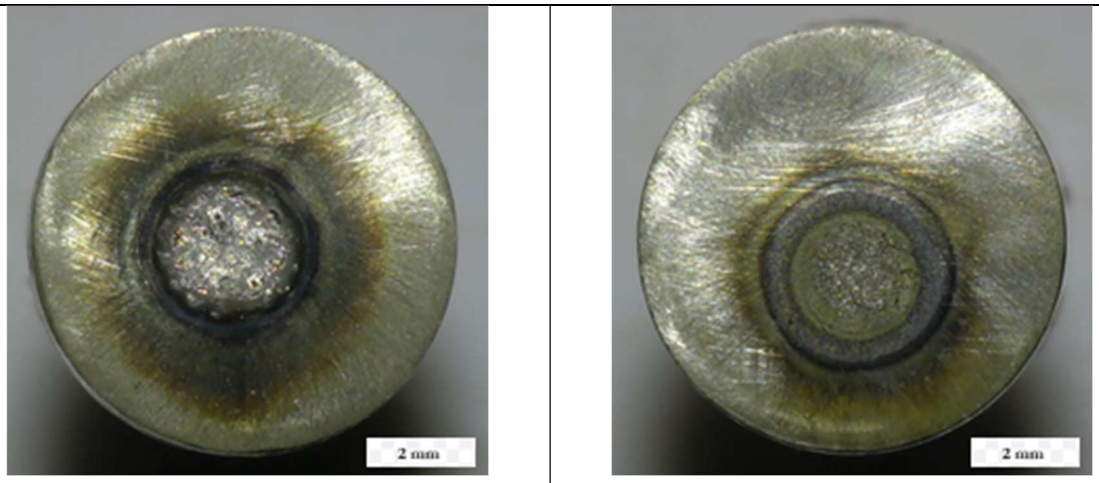


a) Fixed electrode | b) Moving electrode

Figure 64. Images of electrode surfaces after a single arc test.

*Tests with multiple arcs*

Some input conditions in the experimental setup favor the reignition of the arc after the passing through the zero current, for example: cases with longer arc duration, higher currents, worn electrodes.

As an example, the oscillogram for a test with four arcs is shown in Figure 65. The electrode separation occurred at 19 ms when the current was 675 A, and the arc is formed with a voltage of 16.3 V and increased to a value of 27 V. The behavior of this first arc is similar to the one described before: a stable arc that stayed centered between the two electrodes. After the passing through the zero current, the arc reignited, and the electrodes changed their polarity. The arc reignition took place three times in this test, for a total of four arcs. The arcs that followed the first one presented a different behavior: they tended to be more unstable and moving along the electrode edges. They also showed strong plasma jets from both electrodes. This can be observed in Figure 66, where an image for each arc is shown.

The damage done to the electrodes by the four consecutive arcs is significant. Figure 67 shows the state of the electrode surface at the end of the test. A circular mark at the center of each electrode is observed and it corresponds to the traces left by the first arc. Most of the damage is located in the region close to the edge where the reignited arcs stablished, and where large areas with signs of metal melting are visible.

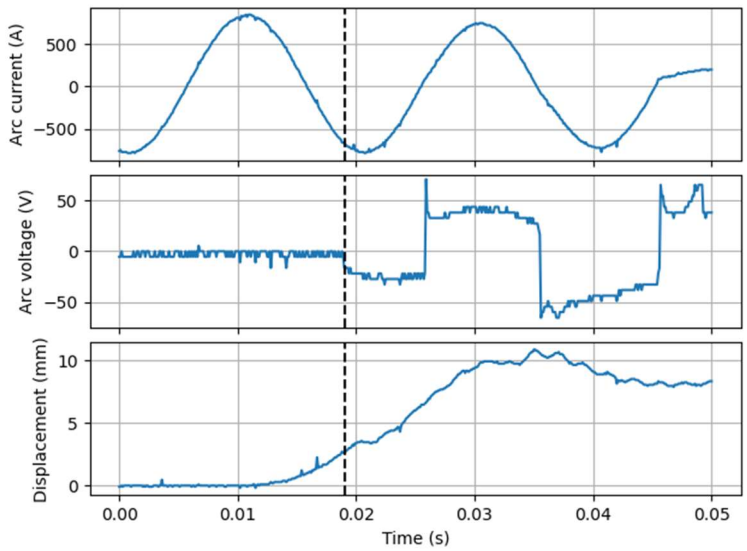


Figure 65. Oscillogram of a test with multiple arcs.

| | |
|---|---|
| 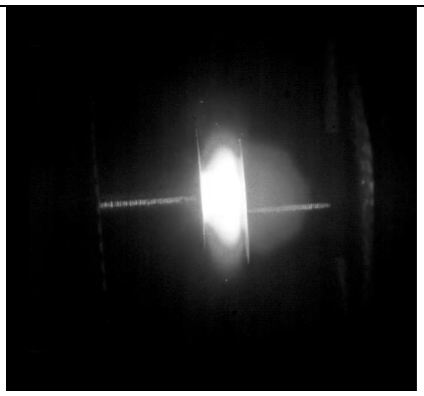 | 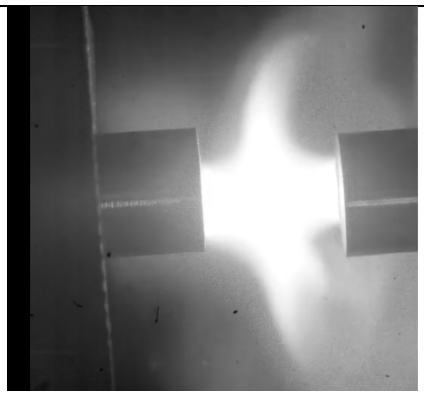 |
| a) First arc | b) Second arc |
| 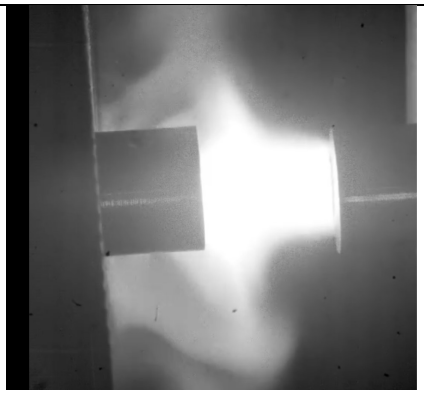 | 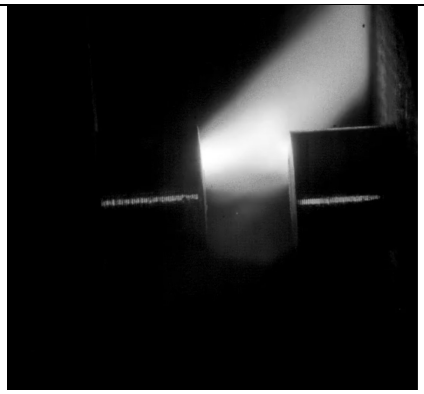 |
| c) Third arc | d) Fourth arc |

Figure 66. Image sequence of a multiple arc test.

| | |
|---|---|
|  |  |
| a) Fixed electrode | b) Moving electrode |

Figure 67. Images of the electrode surfaces after a multiple arc test.

### 4.2.3. Numerical modelling

A numerical model of the experiment was prepared to study the arc-electrode interaction and the electrode ablation on this configuration. The model solves the transient magnetohydrodynamic set of equations on a two-dimensional axisymmetric geometry. The two cylindrical electrodes are set in parallel with an initial gap of 0.4 mm, and atmospheric air surrounds the electrodes. The electrode on the left has a fixed position while the one on the right is defined as the moving electrode. A description of the configuration and its dimensions are displayed in Figure 68.

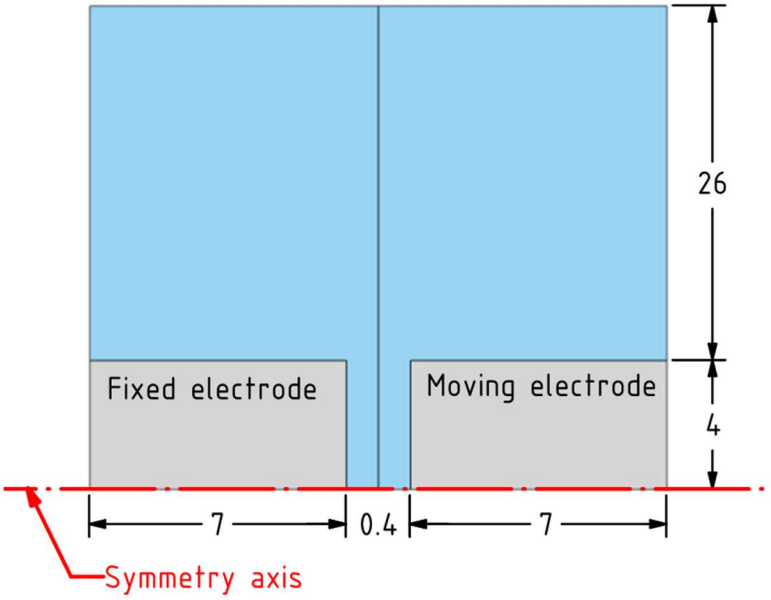


Figure 68. Configuration of the opening contact case.

The electric arc model is coupled to an electric circuit, as the one presented in Figure 59. Equation (60) is used to solve the electric circuit and obtain the current ($I$), with the parameters defined in Table 5.

$$L\frac{dI}{dt} = U_{src} - U_{arc} - I\,R\,, \tag{60}$$

Table 5. Electric circuit parameters.

| Parameter | Value |
|---|---|
| $L$ | $1.14 \cdot 10^{-3}\ H$ |
| $R$ | $0.134\ \Omega$ |
| $U_{src}$ | $210.15\ V$ |
| $\phi$ | $\cos(\phi) = 0.35$ |

where $L$ is the inductance, $R$ is the resistance, $U_{src}$ is the voltage of the power supply, and $\phi$ is the power factor. $U_{arc}$ is the total arc voltage calculated with the model as the sum of the voltage drops in the arc column and the near-electrode regions.

It should be noted that there is not an arc extinction criterion implemented in the model. Therefore, the calculation is forced to stop when the current wave passes through zero after the desired number of arcs are obtained. Otherwise, the electric arc will restart indefinitely after each passing through the zero current.

***NCPL model***

A point should be made about the use of the Near-Cathode Plasma Layer (NCPL) model, described in Chapter 2, on non-refractory materials as those employed in the experimental study. Before implementing the NCPL model in the separating electrode case, a preliminary study was performed to see its feasibility.

As an example, the NCPL functions calculated for a silver cathode interacting with an argon arc are shown in Figure 69. The graph shows the near-cathode voltage drop as dots for different temperatures and current densities. Similarly, a blue region marked as “Experiments” is added to the image based on the experimental results described in the previous section for single arc tests: arc voltages that range approximately between 15 and 30 V and temperatures that do not exceed the boiling temperature of silver.

When comparing in Figure 69 the NCPL data points and the experimental zone for a temperature interval between 1000 K and 2435 K (silver boiling temperature), one can see a great difference in their corresponding near-cathode voltage drop. In fact, even for very low current densities, in the order of $\sim 10^4$ A/m2, the voltage drop in the near-cathode region can exceed by a factor of 10 those measured experimentally. Only when the temperature in the cathode increases to the point where thermionic electron current becomes dominant, the near-

cathode voltage drop falls to values around 10 – 20 V. However, those values imply having a cathode temperature more than 1000 K higher than the boiling temperature of silver, which do not correspond to the damage to the cathode observed in the experiments, for example in Figure 64 b).

Furthermore, the current density at the cathode surface can be estimated based on the traces left by the arc. For a maximum current of $600\sqrt{2}\ A$ and an arc attachment radius to the cathode of $1.5\ mm$, the resulting current density is $1.2 \cdot 10^8\ A/m^2$. As seen in Figure 69, this order of magnitude is only obtained when the cathode temperature is at least 4000 K. Again, such a high temperature is not consistent with experimental observations.

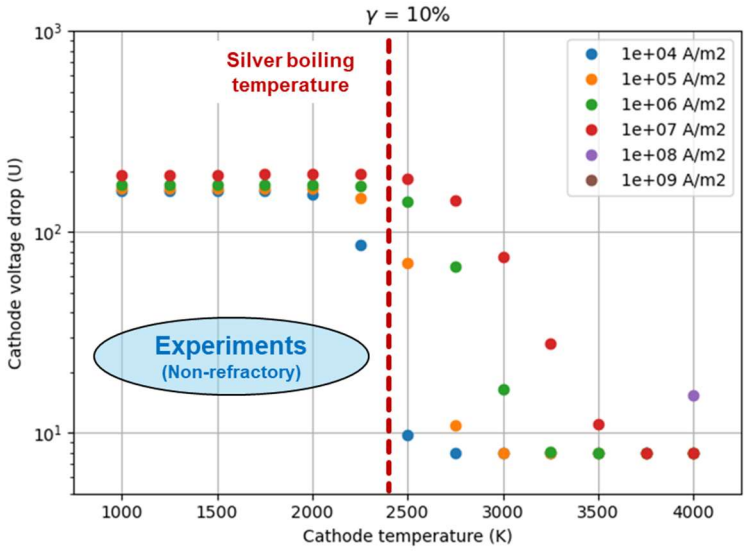


Figure 69. Representation of the NCPL functions and the experimental measurements.

A possibility studied in order to reduce the discrepancies observed in the near-cathode voltage drop at low temperature was to increase the secondary electron emission ($\gamma$). Originally, a value of 10% was assumed since it is a common choice in the literature [10], [52]. Increasing this parameter in the NCPL model will result in a lower near-cathode voltage drop at temperatures where the thermionic current is not dominant. This can be seen in Figure 70, where the NCPL functions for three secondary electron emission coefficients (10%, 20%, and 40%) and two current densities ($10^7\ A/m^2$ and $10^8\ A/m^2$) are presented. In the temperature range of interest (1000 K – 2435 K), and with a current density of $10^7\ A/m^2$, the voltage drop in the near-cathode layer decreases from 190 V when $\gamma = 0.1$ to 50 V for a $\gamma = 0.4$. However, even after increasing the secondary electron emission, a current density of $10^8\ A/m^2$ can only be obtained at a temperature equal to 4000 K.

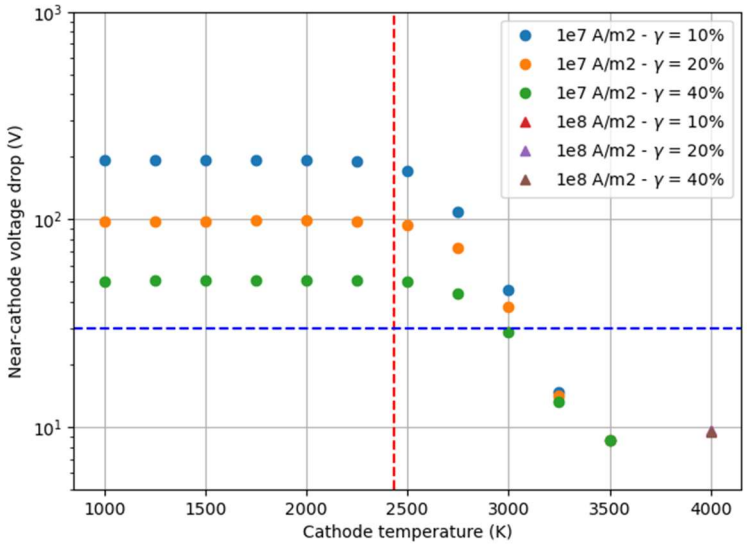


Figure 70. Influence of the secondary electron emission coefficient ($\gamma$) on the NCPL functions.

Some authors have suggested that a field enhancement factor ($\beta$) should be considered in order to have the similar voltage drops as those measure in experiments. This factor multiplies the electric field at the cathode surface and allows to account for effects of the cathode roughness, protrusions, and presence of ions close to the surface [65]. A typical value for the field enhancement factor use in arc modelling is a few hundred. This parameter is also implemented in the NCPL model and the results for $\beta$ equal to 1, 10, and 50 are illustrated in Figure 71. When the current density is $10^7\ A/m^2$, the effects of increasing $\beta$ to 10 are visible starting from 1750 K and become more noticeable as the cathode surface temperature increases. If the $\beta$ value is set to 50, the near-cathode voltage drop reduces from 190 V to approximately 12 V. Higher current densities ($10^8\ A/m^2$) are possible at temperatures superior to 3500 K for $\beta$ values of 1 and 10. For field enhancement factor values of 50 or higher, it is possible to have a current density of $10^8\ A/m^2$ in all the temperature range. However, the exact value of $\beta$ is rarely known and it is usually chosen to match the experimental observations. Moreover, the choice of high field enhancement factors, while decreasing the near-cathode voltage drop, may lead to unphysical results as described in [10].

For all the reasons previously mentioned, the NCPL case will not be used to model cathode-arc interaction in the opening contact case. Instead, the fixed current density ratio approach described in Chapter 2 is implemented.

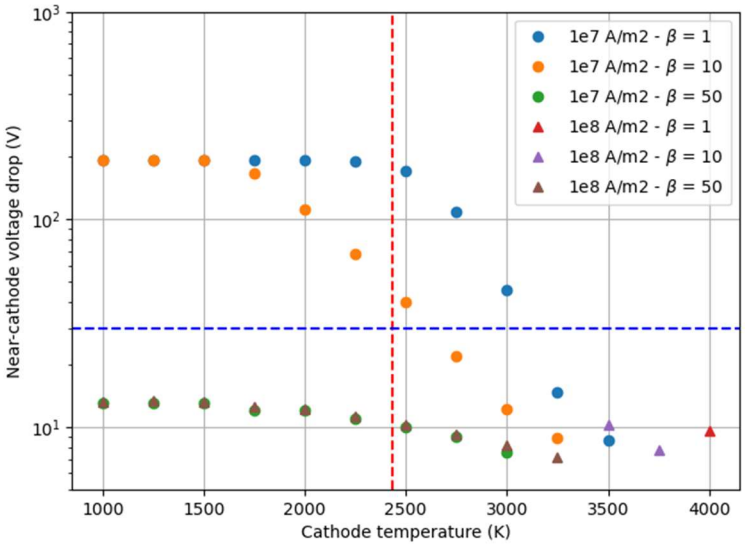


Figure 71. Influence of the field enhancement factor ($\beta$) on the NCPL functions.

***Boundary and initial conditions***

The boundary conditions in the case are as follows: the external boundaries of the gas volume are set to a pressure equal to 1 bar. A constant temperature of 300 K is fixed at the electrode ends. The base of the fixed electrode is set to a reference electric potential of 0 V, while a current density input is imposed at the moving electrode end.

The interaction between the arc column and the cathode is given by the fixed current density ratio approach. A contact resistance at the interface arc-cathode allows to obtain the near-cathode voltage drop, its value is calculated locally based on the curve presented in Figure 13. As mentioned in Chapter 2, the ratio of electron current with respect to the total current at the cathode surface ($j_e/j_w = 0.78$) is based on estimations for thermionic cathodes. To adapt this approach to the case of non-thermionic cathodes, the ratio $j_e/j_w$ is adjusted using the observations and conclusions found in [82] as reference. In particular, it is noted in [82] that the energy injected in the near-cathode layer ($U_c \cdot j_w$) is equally divided between the arc column and the cathode. This allows to estimate a ratio of $j_e/j_w = 0.65$ under typical conditions at the interface ($T_w = 1000\ K$, $T_{LTE} = 20000\ K$). Once the ratio is known, equation $(29)$ is used to calculate $q_{cath}$, and then $q_{plas}$ is obtained with equation $(25)$.

To obtain the voltage drop in the near-anode region, a similar approach is used where the values presented in Figure 17 are introduced as a contact resistance profile along the arc-anode interface. The heating of the anode is given by equation $(37)$ without considering the

voltage drop term, as mentioned in Chapter 2. The $q_{plas}$ term is calculated with equation $(25)$ as well.

It is important to note that the approach used to couple the arc and the electrodes by a zero-interface is applied only where the arc foot is present. Outside the arc foot, a heat conduction condition between the gas and the electrode is implemented as:

$$q_{cond} = -\overline{\lambda_T}\left(\frac{T_{elec} - T_{gas}}{\delta x}\right), \tag{61}$$

where $q_{cond}$ is the conduction heat flux ($q_{cond} = q_{elec} = -q_{gas}$), $\delta x$ is the distance between the fluid and solid cell centroids, and $\overline{\lambda_T}$ is the harmonic mean of the gas and electrode thermal conductivity at the interface [83]:

$$\overline{\lambda_T} = \frac{2 \cdot \lambda_{T_{gas}} \cdot \lambda_{T_{elec}}}{\lambda_{T_{gas}} + \lambda_{T_{elec}}}. \tag{62}$$

To make the transition between the arc foot condition and the condition outside the arc foot, a coefficient ($x_{arc}$) is calculated based on the current density:

$$x_{arc} = 1 - \tanh^5\left(\frac{j_w}{j_0}\right), \tag{63}$$

where $j_0$ is a parameter used to specify the threshold current density between arc foot and outside the arc foot with a value of $10^7\ A/m^2$. Therefore, the heat flux at the electrodes is given by:

$$q_{elec} = q_{a,c} + x_{arc} \cdot q_{cond}. \tag{64}$$

At both arc-electrode interfaces, the terms corresponding to the electrode ablation model described in Chapter 3 are implemented when the local surface temperature is higher than the melting temperature: the cooling of the electrode due to metal vaporization, and the injection of metal vapor in the gas volume with its respective enthalpy. The diffusion mass flux

of metal vapor in air is calculated considering only the combined ordinary diffusion term, which is a valid approximation since convection is dominant in the arc center [17].

For the conditions at $t = 0\ s$, an initial temperature profile is defined in the plasma to ensure an electrically conductive path between the electrodes. The profile is given as:

$$T_{pl}^{0} = 300\ K + 20000\ K \exp\left(-\frac{r^2}{r_0}\right), \tag{65}$$

where $r_0$ is a parameter set to $10^{-3}\ m$, and $r$ is the radial coordinate. An initial profile for the metal vapor concentration is also defined, as to consider the metal vapors in the medium after the metal bridge breaks and the metallic arc is formed. The metal concentration profile has a similar shape to that of the initial temperature:

$$\overline{Y_M}^{0} = 1 \cdot \exp\left(-\frac{r^2}{r_0}\right). \tag{66}$$

In the electrodes an initial hotspot is set at the center of the front surface, with a temperature of 1235 K and a radius of 1 mm. A velocity of 0.5 m/s is applied to the moving electrode in the direction away from the fixed electrode based on the experimental setup. The electrode starts moving from $t = 0.8\ ms$, which is the time needed to reach the initial distance (0.4 mm) at the mentioned speed. It will continue to move until the calculations stops or until it reaches an interelectrode distance of 8 mm.

The case was implemented and solved in ANSYS Fluent 2021 R2 using a pressure-based solver with a SIMPLE algorithm.

***Results***

*One arc case with silver electrodes*

The calculation was performed for an arc between silver electrodes. The fixed electrode is set as anode, while the moving one acts as cathode. The arc current at the opening of contacts was 665 A and reached a maximum of 765.7 A after 1.7 ms. The calculation stopped at 6.53 ms, when the current is zero. The arc voltage was 18.2 V after the separation of contacts and remains almost constant until the cathode begins to move. As the electrodes

separated, the arc voltage increased slightly until it reaches a maximum of 26.6 V just before the zero current. A comparison of the calculated values of arc current and the arc voltage with those measured experimentally under similar conditions is shown in Figure 72, where it can be seen that numerical results are in good agreement with the experimental data.

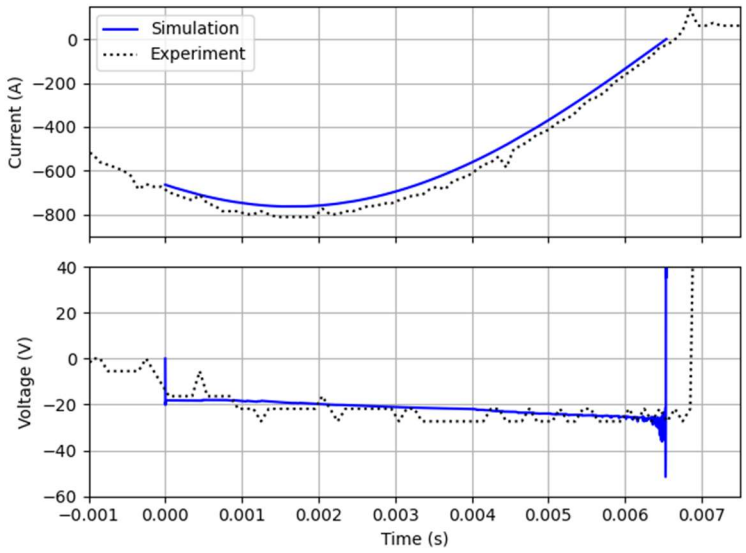


Figure 72. Comparison of experimental measurements and numerical results for the arc current and arc voltage.

High-speed images taken during the experiment are also used to evaluate the global arc shape of the simulated arc. The luminous regions of the arc images are compared with the temperature distributions obtained numerically at different times: 1, 3, and 5 ms, they are presented in Figure 73.

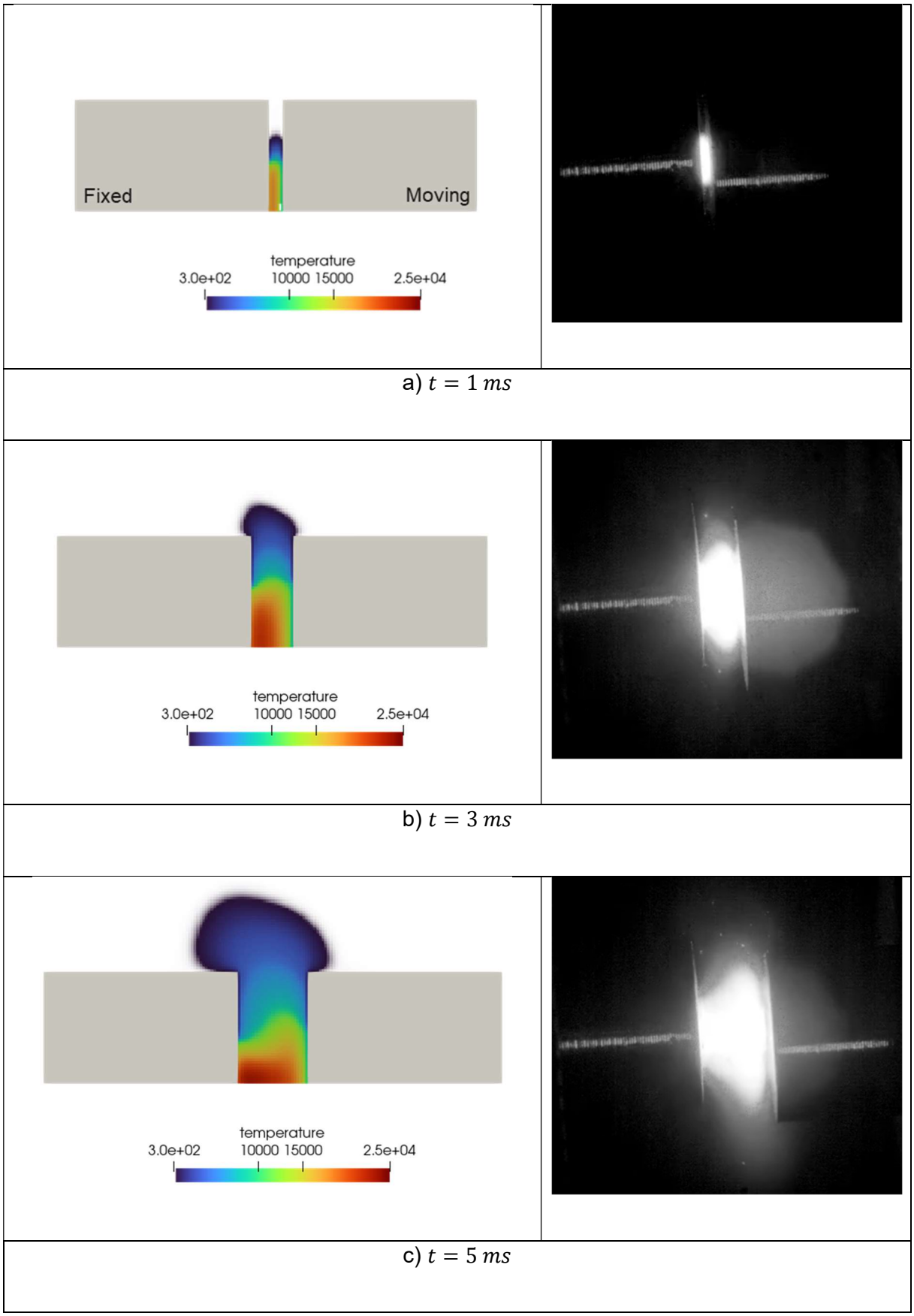


a) $t = 1\ ms$

b) $t = 3\ ms$

c) $t = 5\ ms$

Figure 73. Comparison of the arc shape between numerical results and experiments.

At 1 ms after the contact separation, the arc is rather small and confined between the two electrodes, with the higher temperatures located near the fixed electrode. As the interelectrode distance increases, a plasma flow (presented in Figure 74) is observed from the fixed contact to the moving electrode creating a pear-like shape of the arc. This arc shape emulates the arc recordings from the experiments.

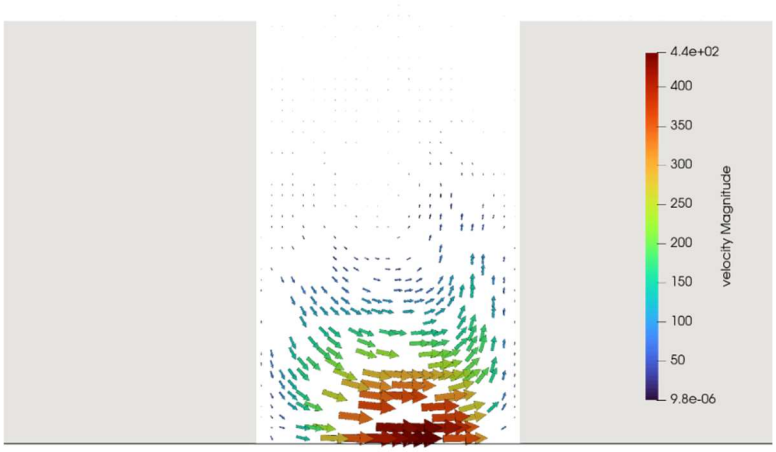


Figure 74. Velocity vectors (m/s) between the electrodes at $t = 5\,ms$.

The fields of silver concentration are shown in Figure 75, where the white arrow vectors indicate the normalized mass flux of silver vapor in air due to combined ordinary diffusion. After 1 ms, the metal concentration expanded from the initial profile in the radial direction. The strongest diffusion mass flux ($1.4 \cdot 10^{-1}\ kg/m^2/s$) occurred close to the right electrode since the lower plasma temperatures results in higher combined ordinary diffusion coefficients. At 3 ms, the highest silver concentrations (around 35 %) are located close to the moving electrode, which can be attributed to the gas flow between the electrodes. Signs of electrode vaporization are observed from $t = 5\,ms$ as the mass concentration of silver locally increased to 30 % in the vicinity of the fixed electrode. As the metal vaporization continued, the silver concentration rose to 44 % next to the fixed electrode surface at 6 ms and a channel of metal vapor is maintained between the electrodes due to convection effects.

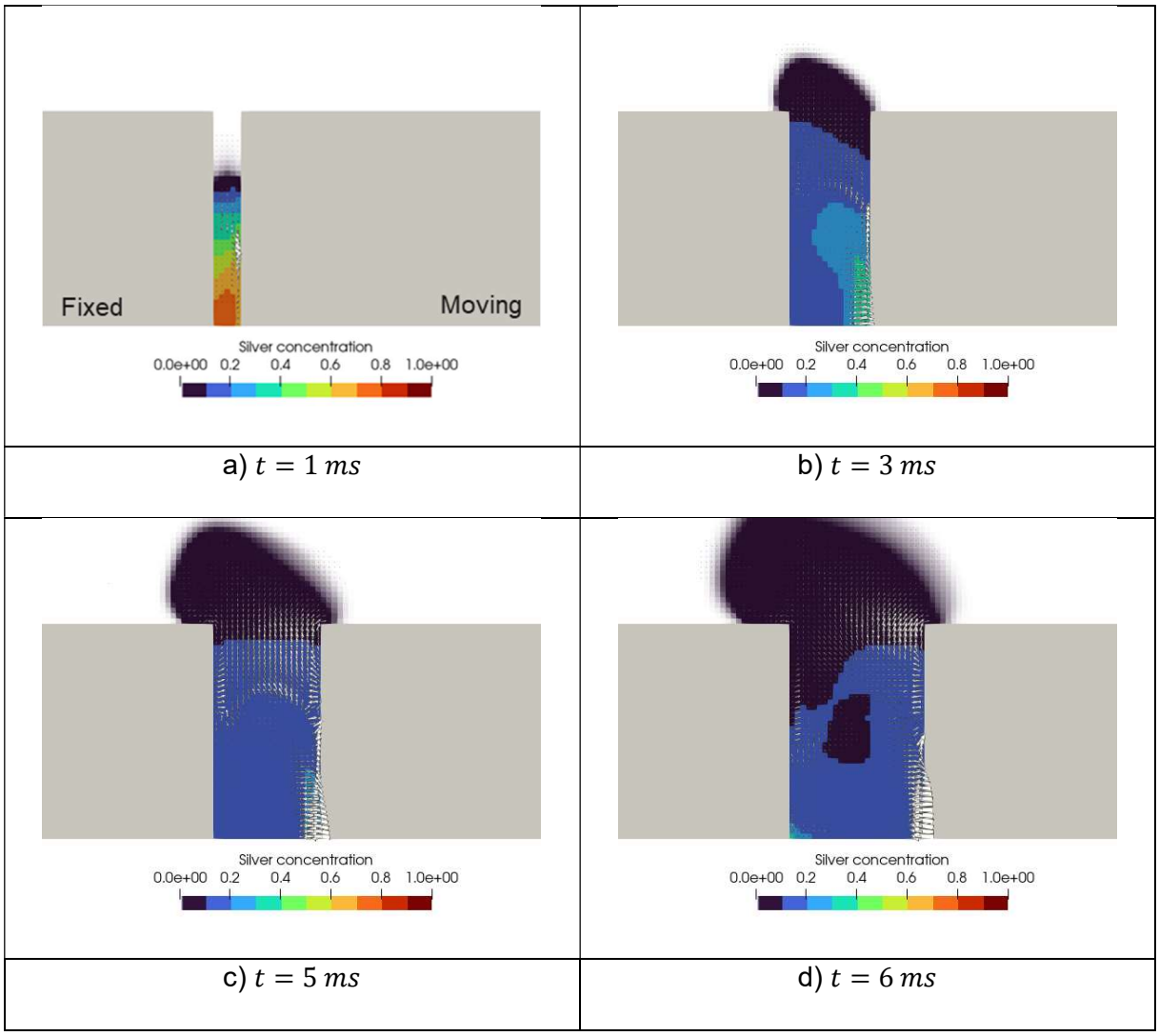


a) $t = 1\ ms$ b) $t = 3\ ms$

c) $t = 5\ ms$ d) $t = 6\ ms$

Figure 75. Distributions of metal concentration at different times.

Moreover, the model allows to estimate the temperature at the electrode surface, which can be a good indicator of the impact that the arc has on the contacts. Figure 76 describes the temporal variation of the maximum electrode temperature from the initial condition to the zero current point, for both the fixed and the moving electrodes. In the moving electrode, which is acting as cathode, the temperature decreased from its initial value to 850 K and remained close to this value during all the calculation. The fixed electrode, on the other side, presented an initial decrease in its temperature during the first tenths of millisecond. After this, the temperature started increasing again, where it reached a maximum of 1500 K. This difference in the electrode temperature is compatible to what was observed in the one arc tests: the anode presenting greater damage in its surface than the cathode.

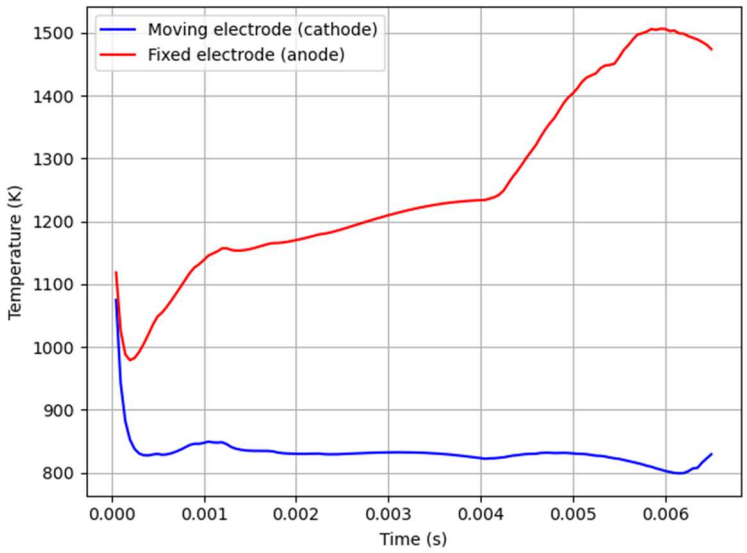


Figure 76. Temporal evolution of the electrode temperature.

The rate of mass evaporated from the surface is also calculated in the model for the two electrodes, the results are displayed in Figure 77. The fixed electrode started evaporating once it exceeded the melting temperature around 4 ms, the maximum value in the ablated mass rate of $0.28 \cdot 10^{-3}$ kg/s is obtained at 5.85 ms. At the end of the calculation, the total mass ablated from the fixed electrode was $3.07 \cdot 10^{-7}$ kg. No evaporation occurred on the moving electrode as its temperature remained below silver melting point.

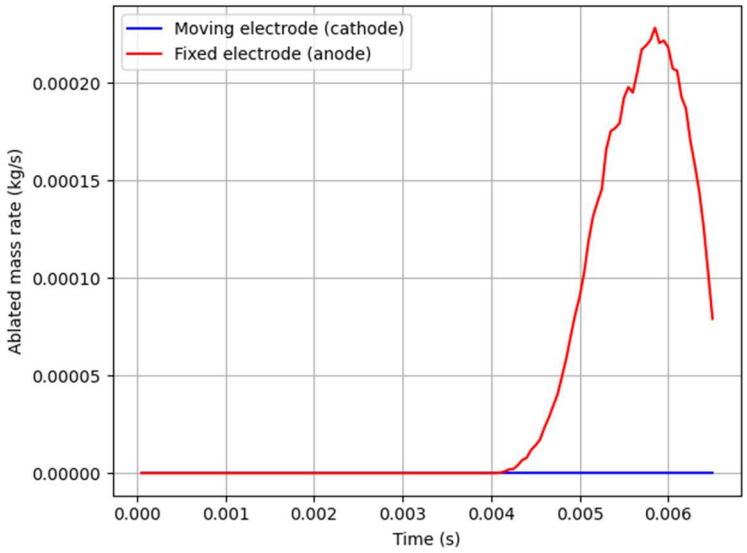


Figure 77. Temporal evolution of the total ablated mass rate.

Finally, the melted volume in the electrodes can also be estimated by integrating the volume of the cells above the melting temperature for silver. The results for both electrodes

are presented in Figure 78. As already mentioned, melting only occurred in the fixed electrode starting at around 4 ms. The maximum is obtained at 5.5 ms with a value of $2.83 \cdot 10^{-10}\ m^3$, which represents roughly 0.08 % of the total electrode volume.

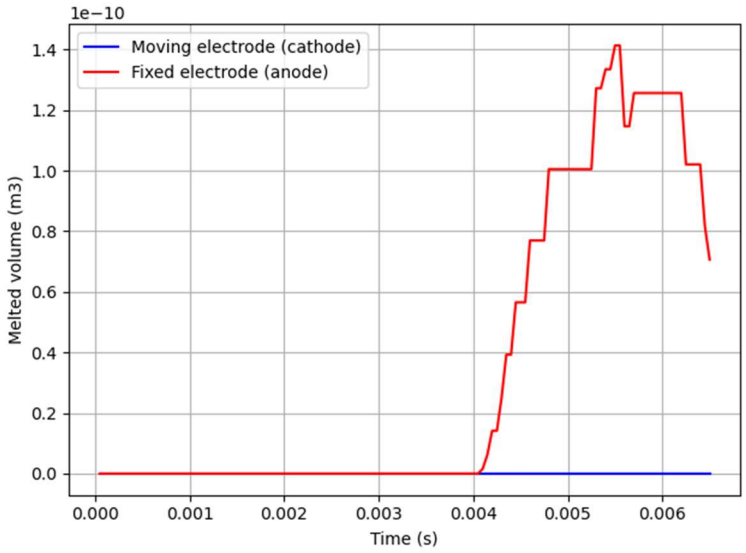


Figure 78. Temporal evolution of the electrode melted volume.

***Influence of the electrode ablation model***

It is interesting to study what is the impact of excluding the electrode ablation in the model, meaning: the vaporization of the electrode material and its effects on the arc. To that end, a new calculation was performed by removing the initial profile of silver vapor in the gas, and all the mass and energy sources related to the metal vaporization. Therefore, the silver concentration is guaranteed to remain 0 %.

Figure 79 shows the results of the model without ablation model (“Pure Air”) with the previous model (“Air+Ag”, where the ablation is considered and metal vapors are present in the gas), and the experimental measurements. Slightly higher values of the arc voltage for the pure air case are observed in the graph, as expected, with variations of up to 5 V between the model with ablation and that without ablation. No notable differences were observed in the arc current.

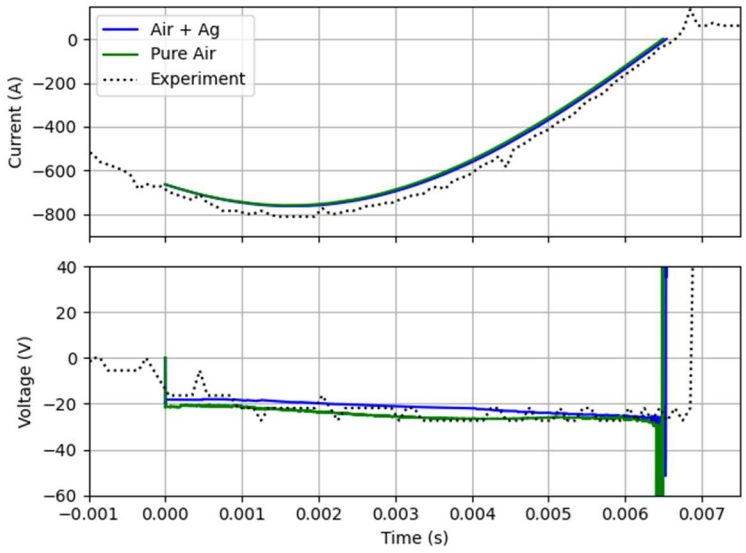


Figure 79. Comparison of experimental measurements of arc voltage and current and the numerical results with and without electrode ablation.

The next figure presents the temperature fields of the arc at different times. A comparison of the temperature contour with the Air + Ag, allows to note that the pure air case presents an arc that is more constricted and with higher temperatures at the beginning of the calculation. At 3 ms, it is possible to observe a plasma flow that was stablished from the moving electrode to the fixed electrode and maintained until the end of the calculation. The velocity vectors in the pure air case at $t = 5\ ms$ are displayed in Figure 81, which has roughly the same magnitude at the arc center although orientated in the opposite direction.

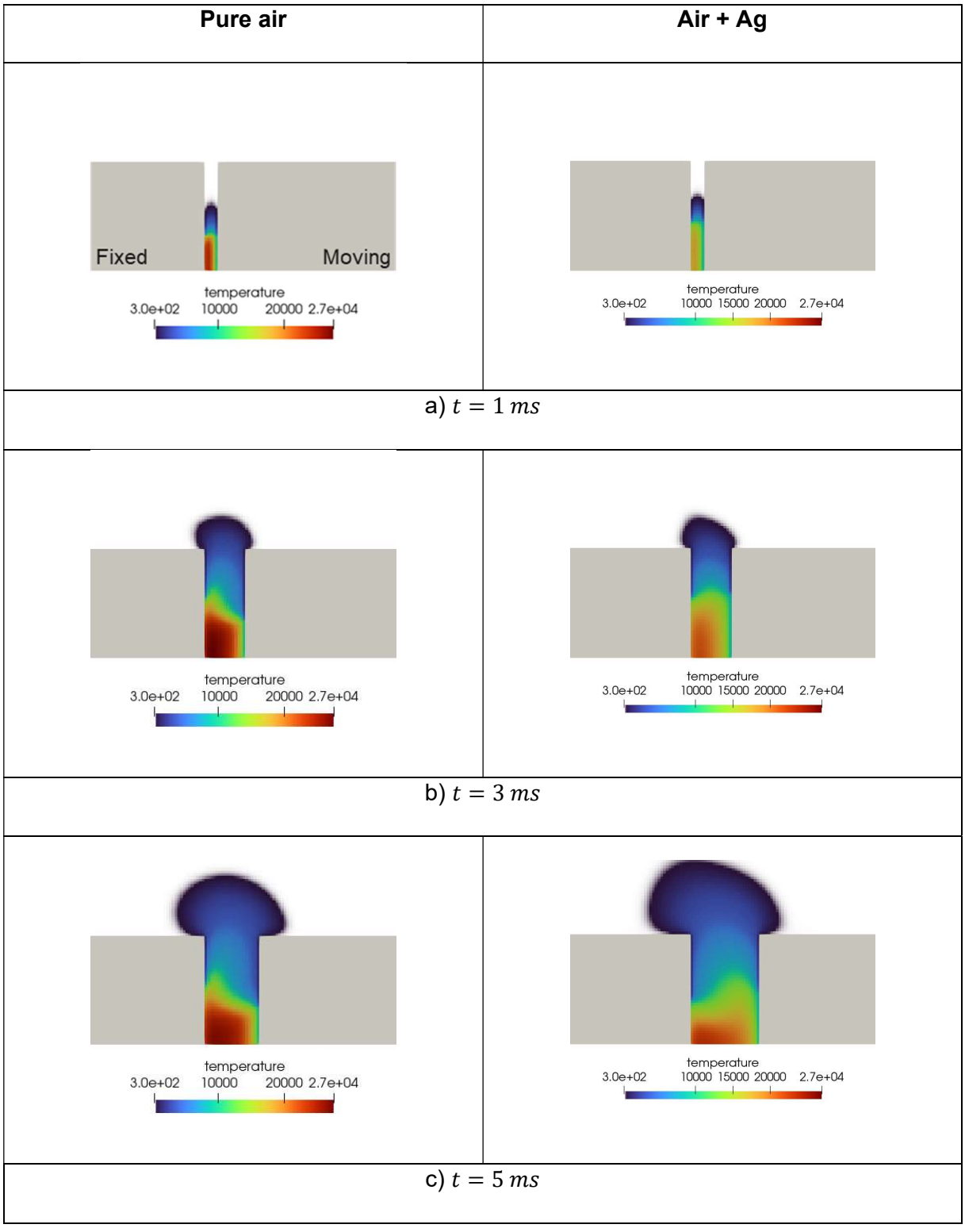


Figure 80. Temperature distribution of the arc in the pure air case and the Air + Ag case at different times.

| Pure air | Air + Ag |
| --- | --- |
| 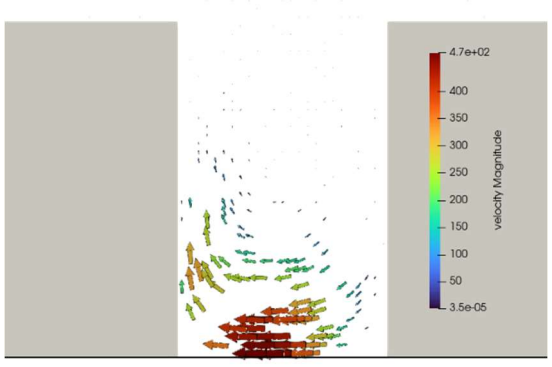 | 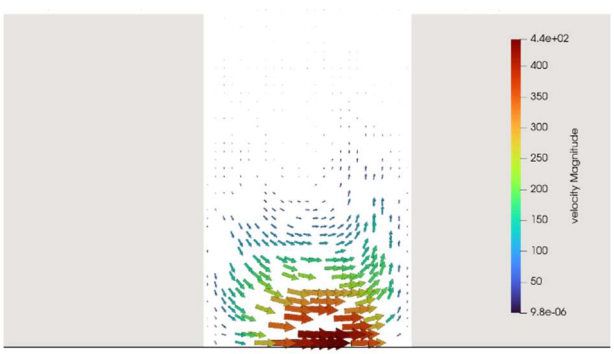 |



Figure 81. Velocity vectors between the electrodes in the pure air case and Air + Ag case after 5 ms.

Concerning the variation in time of the electrode temperatures, Figure 82 presents the results for the pure air case and the case considering electrode ablation. It can be seen from the figure that when the electrode ablation is not included in the model both electrodes will exhibit higher temperatures during all the time range studied. In the case of the fixed electrode, the temperature rose rapidly from the beginning and reached a maximum of 2450 K at 2.3 ms, which is slightly above the boiling temperature of silver. This represents an increase in the maximum temperature of 950 K with respect to the case with electrode ablation. For the moving electrode, the temperature had a maximum of 1370 K at 4 ms, surpassing the melting point of silver. The higher temperatures observed in both electrodes with respect to the case with ablation can be attributed to the higher current densities that results from a more constrained arc when the metal vapors are not present in the medium.

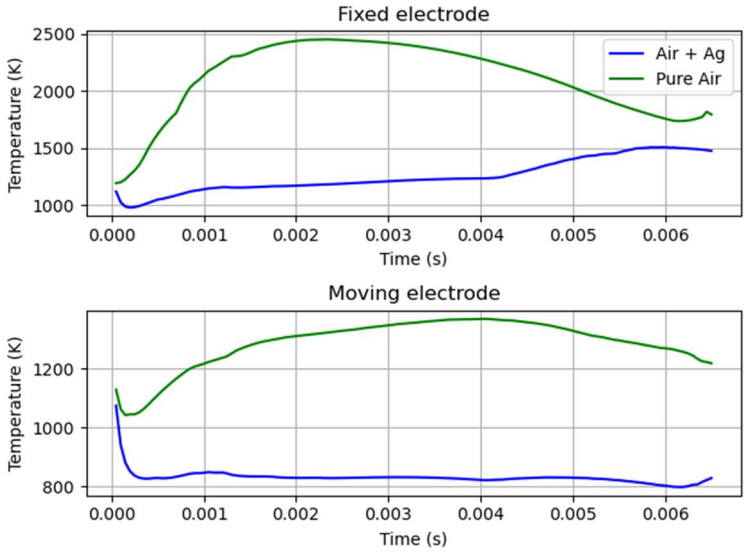


Figure 82. Comparison of the temporal evolution of the electrode temperature for the Air+Ag and pure Air cases.

The evolution of the melted volume in the electrodes are shown in Figure 83. In the fixed electrode, it increased from the initial condition to a maximum of $1.28 \cdot 10^{-9}\ m^3$ at 3.7 ms, before decreasing to $6 \cdot 10^{-10}\ m^3$ at the end of the calculation. The maximum melted volume in the fixed electrode was one order of magnitude higher in the pure air case compared to the Air + Ag case. When the electrode ablation is not included in the model, the moving electrode also presented melting from $t = 1.15\ ms$, reaching its maximum of $2 \cdot 10^{-10}\ m^3$ at 3.5 ms.

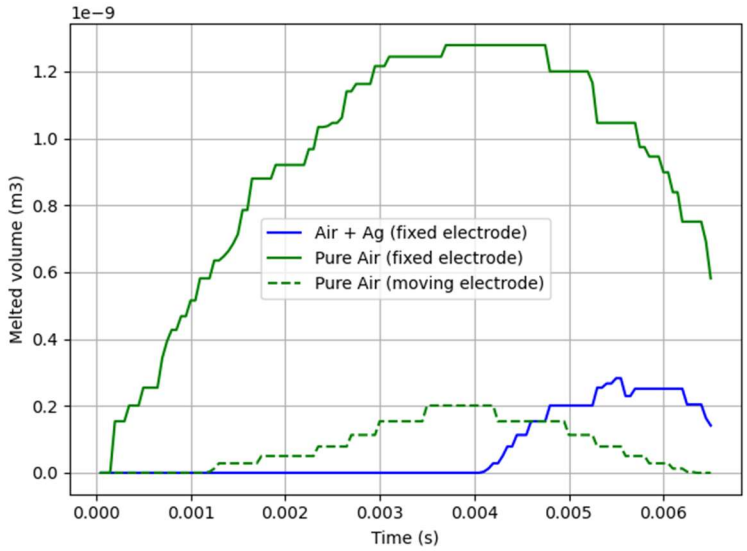


Figure 83. Comparison of the temporal evolution of the melted volume for the Air+Ag and pure Air cases.

***Influence of the electrode material***

To observe the influence of the electrode material on the one arc test, the calculation was repeated by considering copper instead of silver. The boundary and initial conditions are kept unchanged. Only the initial temperature of the electrodes was adjusted to that of the melting temperature of copper (1358 K). Figure 84 shows the comparison of the numerical results for silver and copper electrodes with those obtained experimentally with AgSnO2 electrodes. From the graph it is clear that the change of the electrode material, and therefore the metal vapor in the plasma, did not affect the arc current or the arc voltage curves. In fact, only a few volts difference was observed in the model between the two electrode materials.

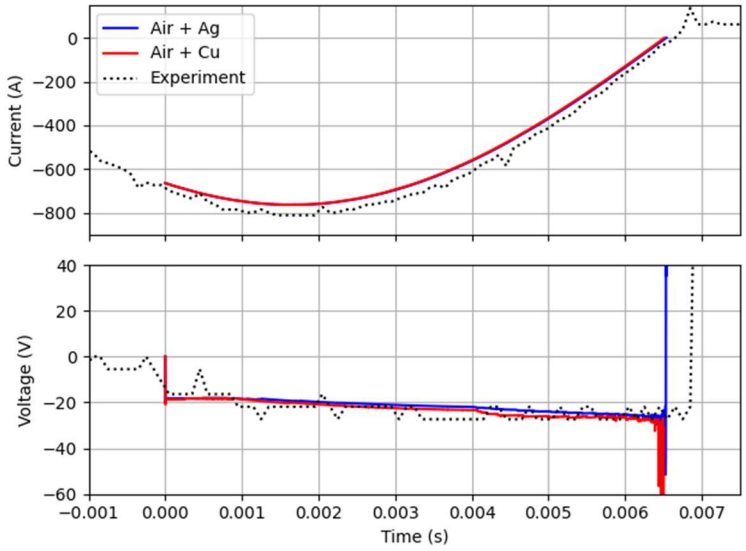


Figure 84. Comparison of experimental measurements of arc voltage and current and the numerical results for different electrode materials.

The distributions of the arc temperature and copper vapor concentration are presented in Figure 85 and Figure 86, respectively. Similar to the first 3 ms in the silver electrode case, the highest temperatures were located close to the fixed electrode surface (anode). During this time, the copper vapors in the plasma diffused rapidly, with the mass concentration decreasing to a maximum of 19 % next to the moving electrode, compared to 35 % in the silver electrode case at the same instant. After 5 ms, the plasma flow is observed to be from the moving electrode to the fixed electrode. Even though there exists metal vaporization at the fixed electrode, the mass flow rate in the copper electrode is considerably smaller than that of the silver case, as shown in the next figures. This results in a further reduction of the copper mass concentration in the gas with values lower than 1 % in all the fluid domain.

| Air + Cu | Air + Ag |
| --- | --- |
| 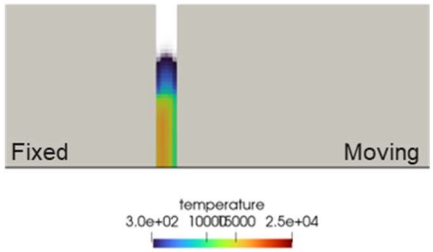 | 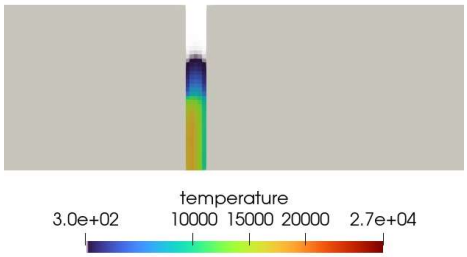 |
| a) $t = 1\ ms$ | |
| 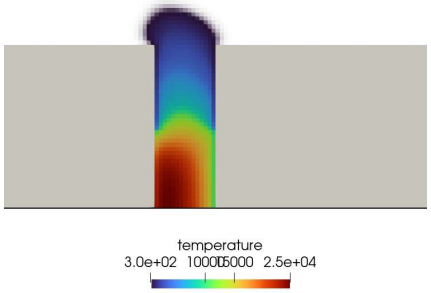 | 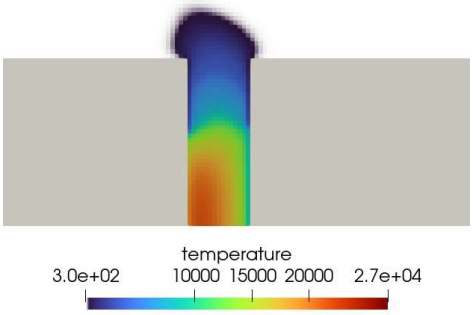 |
| b) $t = 3\ ms$ | |
| 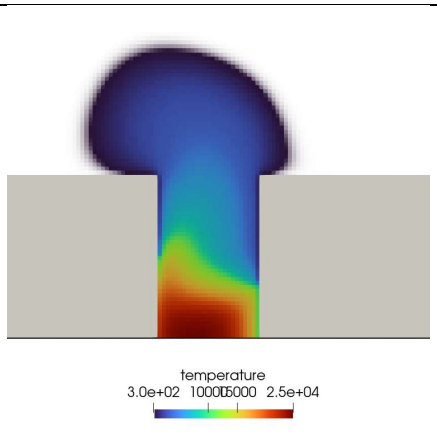 | 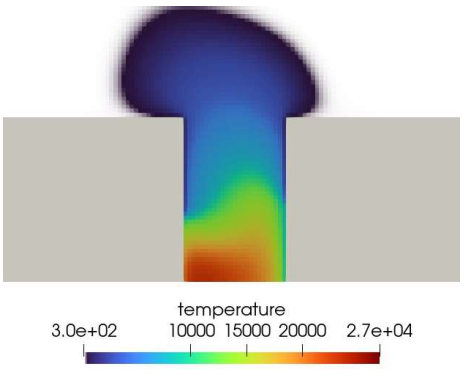 |
| c) $t = 5\ ms$ | |

Figure 85. Distributions of temperature for the Air + Cu case and the Air + Ag case at different times.

| Air + Cu | Air + Ag |
| --- | --- |
| 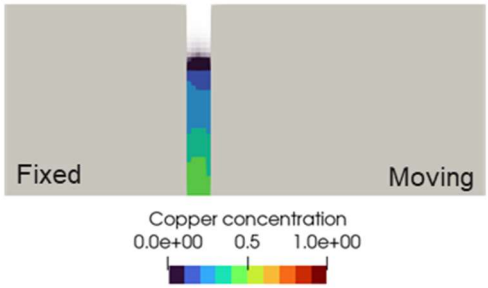 | 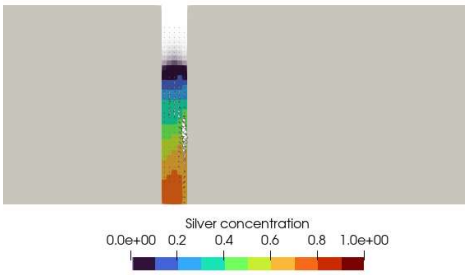 |
| a) $t = 1\ ms$ | |
| 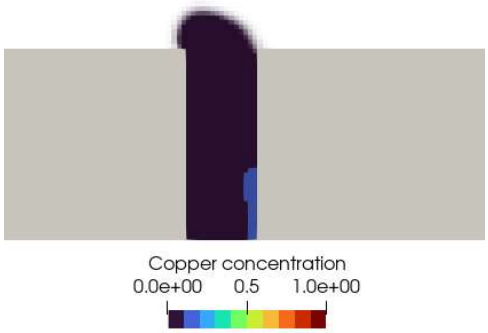 | 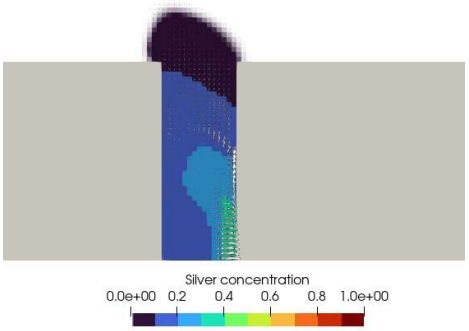 |
| b) $t = 3\ ms$ | |
| 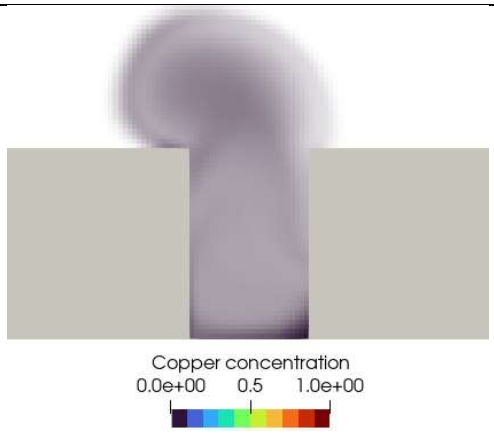 | 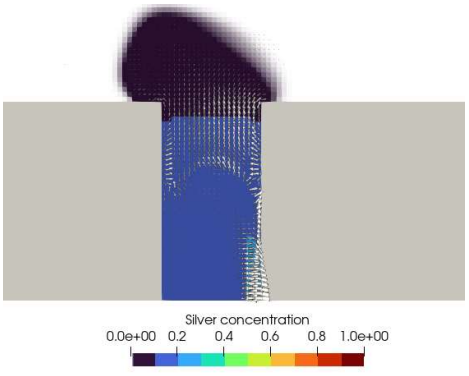 |
| c) $t = 5\ ms$ | |

Figure 86. Distributions of metal concentration for the Air + Cu case and the Air + Ag case at different times.

The next three figures present the effects that the arc had on the copper electrodes and how they compared to the silver ones. Figure 87 shows the temporal evolution of the temperature at the center of both electrode front surfaces. The fixed electrode, acting as anode, showed higher temperatures that the moving electrode (cathode), consistent with the previous cases. When copper is defined as the electrode material, the fixed electrode reached faster the melting temperature than the original case with silver electrodes (3.4 ms for copper electrode vs 4 ms.for silver). The maximum temperature in the fixed electrode was obtained at 4.85 ms with a value of 1429 K, which was lower than the maximum temperature in the fixed silver electrode (1500 K). On the other side, the moving electrode presented higher temperatures in the copper case during all the calculated time, however it was not enough to have melting.

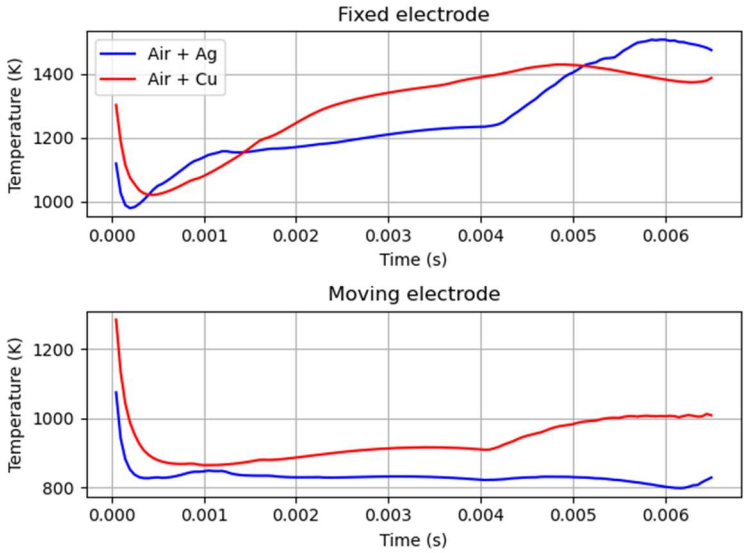


Figure 87. Comparison of the electrode temperature evolution for different materials.

A comparison of the ablated mass rate for copper and silver fixed electrodes is presented in Figure 88. From the graph is evident that the ablate mass rate was notoriously lower in the case of copper electrodes. The maximum reached was $1.25 \cdot 10^{-6}$ kg/s at 4.9 ms, which is two orders of magnitudes lower than the corresponding value for silver electrodes. The total ablated mass at the end of the calculation was $1.96 \cdot 10^{-9}$ kg. Regarding the melted volume in the fixed electrodes, the comparison between the different materials is shown in Figure 89. At around 4.4 ms, the melted volume reached its maximum value of $8 \cdot 10^{-11}\ m^3$. This represents a decrease of 71.7 % with respect to the silver electrode case ($2.83 \cdot 10^{-10}\ m^3$).

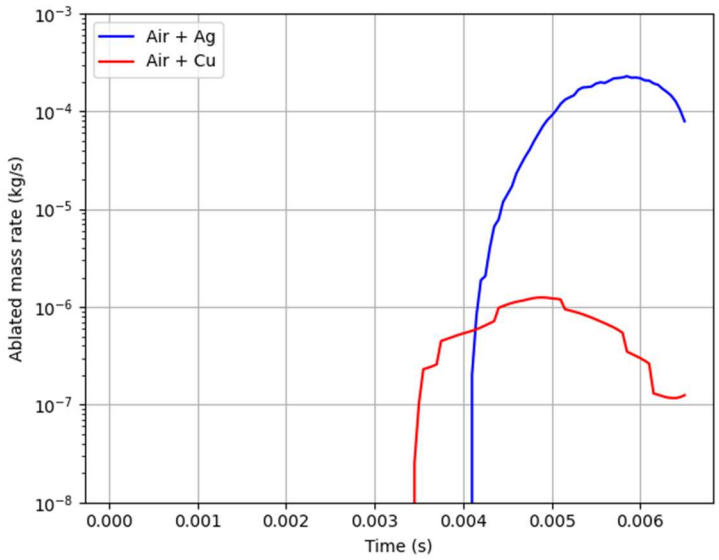


Figure 88. Comparison of the ablated mass rate in the fixed electrode for different materials.

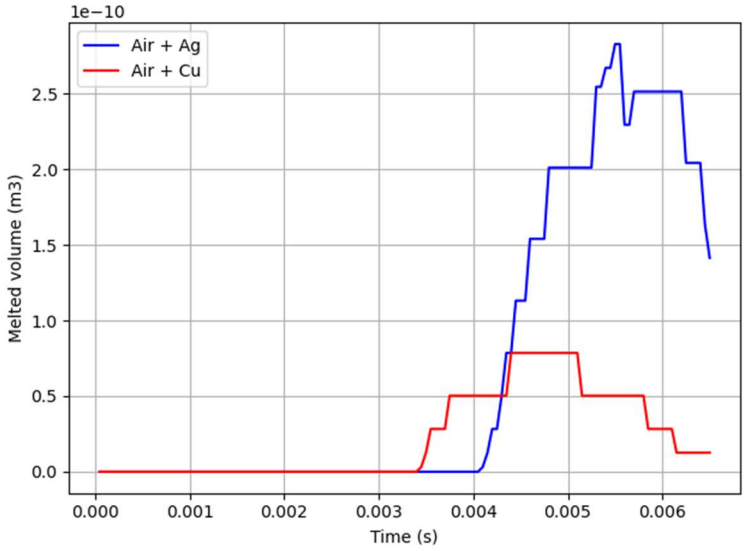


Figure 89. Comparison of the melted volume in the fixed electrode for different electrode materials

## 4.3. SUMMARY

Chapter 4 presented an example of low-voltage switching devices. The case of study consisted of two electrodes initially closed that opened under an AC electrical load, configuration typical of industrial contactors. At first, an experimental setup was used to study the arc behavior and the impact that it has on the electrodes. The measurements and observations made during the tests were also used to compare with the numerical model. Two main cases were noted in the experiments: single arc and multiple arc cases. In the single arc

case, the interruption of the arc current occurred at the first passing through the zero current, without reignition of the arc. It is characterized by a stable arc that stay centered at the electrode face. Microscope images of the electrode surfaces after the operation showed some signs of melting, with a higher impact on the fixed electrode that acted as anode. When reignition of the arc occurred during the tests, a more chaotic behavior was observed after the first arc, with strong plasma jets leaving both electrodes. The damage on the electrode in these cases were also greater with large portions of the surface affected by the arc. Based on the experimental study, a numerical model was prepared where the arc-electrode interaction and the electrode ablation description were included. The results showed good agreement on the arc voltage and arc current when compared to the experimental results. Images of the arc during the experiments were also compared with the numerical results showing a similar pear-like shape. The model also allowed to estimate the electrodes temperature and its evolution in time. Higher temperatures were found in the anode were melting occurred, although the boiling temperature was not exceeded. The results were also compared with a case without electrode ablation model and metal vapors, and with a model where the electrodes are made of copper.

## CONCLUSIONS AND PERSPECTIVES

Numerical simulations of low voltage switching devices have become increasingly available with the growth of computational processing power. They are used to describe the electric arc, that is formed after the contacts separate, and how it interacts with the surrounding elements inside the switching device. One of the aspects that requires special consideration is the treatment of the near-electrode layers since they define the energy and current transfer between the arc and the electrodes. As the arc interacts with the electrodes, it will cause heating, melting, and vaporization of the metal. Also, the presence of metal vapors in the arc will affect its properties and its behavior inside the device.

The thesis main goal was focused on developing a simplified description of the arc-electrode interaction to be used in an LTE arc model for low voltage switching applications. The model therefore had to consider both the energy and current transfer between arc and the electrodes, and the effects of metal vaporization on the arc.

In Chapter 2, the equations that allows to model the electric arc under the LTE bulk assumption were described, together with the zero-dimensional interface approach used to couple the arc column and the electrodes. A particular point of interest was the description of the energy and current transfer on cold cathodes, where the temperature at the surface is not high enough to sustain the arc current only by thermionic electron emission. A well-known model in the literature for thermionic cathodes, the Near-Cathode Plasma Layer or NCPL, was adapted to be used at low cathode temperatures by considering the secondary electron emission. The results of the modified NCPL model applied to a DC Gas Tungsten Arc Welding (GTAW) configuration starting from cold electrodes. It was shown that a transition from high arc voltage to lower values occurs and it is governed by the solution of the heat conduction in the cathode volume: at low cathode temperatures, the main mechanism of current transfer is ionic current leading to high near-cathode voltage drops. Once the temperature at the cathode surface increases to high values (usually around 3500 K), the thermionic emission begins to be significant, and the required cathode fall decreases. This marks the transition stage from cold to hot cathode. Finally, during the arc stage the cathode temperature stabilizes, and the thermionic electron emission remains the dominant mechanism of current transfer. The near-cathode voltage drop at this stage also decreases to typical arc values, ~ 10 V. Several studies were also performed to observe the influence on the cold-to-hot transition of different parameters. It was seen that higher arc currents, sharp edges, or focalized current transfer all led to a faster increase in the cathode surface temperature and therefore accelerated the time at which the transition from cold to hot cathode occurred.

A description of the electrode ablation and the effects that metal vapors have on the arc were also studied in this work. The metal mass injection in the gas as result of the electrode vaporization and the enthalpy associated with it were included in the electric arc governing equations as source terms. To describe the metal vapor behavior in the gas volume a transport equation was added to the system based on the combined diffusion coefficient approach, which allows to simplify greatly the modelling. The ablated mass was estimated based on the Langmuir and the Clausius – Clapeyron equations, which describe the vaporization at vacuum conditions, and thus, overestimate the mass loss in the electrode at high pressures. A parametric study was also performed to understand how the overestimation of the mass losses can affect the temperature calculation in the electrode. For that purpose, a retro-diffusion coefficient was introduced to represent the portion of vaporized mass that returns to the electrode surface. The studied showed that while the retro-diffusion coefficient had a direct impact on the ablated mass calculated, the temperature in the cathode remained mostly unchanged by this coefficient under the different conditions studied. The impact that metal vapors have on the arc plasma properties are also discussed, as is the method used to determine the plasma properties during the calculation.

Finally, a case of two contact separation under an electric load was chosen to apply the models developed in this work. As a first step, an experimental study was conducted to understand the behavior of the arc and then compare with the numerical results. Images taken with a high-speed camera allowed to observe that the arc remained stable and centered between the electrodes after the separation of contacts. Also, microscope images of the electrode surface after one arc confirmed that the electric arc was located at the center of the electrodes, and the arc traces showed signs of melting at the surface with higher effects on the anode. A numerical modeling of this configuration was then studied. A preliminary study of the NCPL model for this scenario showed that even after considering the secondary electron emission, it cannot be used for non-refractory metal such as copper or silver, since it results in either high arc voltages or high cathode temperatures, which contradicted the experimental observations. Several parameters can be altered in NCPL to match the experimental conditions; however, these modifications lacked a physical justification. Therefore, the NCPL model was disregarded for this model and a phenomenological approach was used instead for the arc-cathode interaction by fixing the ratio of electron current density to the total current density. The numerical results of the contact separation showed good agreement with the experimental measurements of arc current and arc voltage. The temperature contours of the arc had a pear-like shape similar to what was observed with a high-speed camera in the tests. Estimation of the electrode temperature showed higher temperatures in the fixed electrode (anode) where the melting temperature was reached, but not the boiling temperature. The effects of removing the metal vapors in the arc was also studied. It was shown that in this case the arc was more constricted and presented higher temperatures in its core. It also resulted in

higher temperatures in the electrodes, with melting occurring in both electrodes. A case with copper electrodes was also modelled. The electrode temperatures were comparable in both cases, but high evaporated mass is obtained for silver electrodes due to lower boiling temperature of silver. Higher vapor diffusion was also observed when the metal in the gas is copper.

## PERSPECTIVES

The modified version of the NCPL model used in this work, while allowing to describe the arc-cathode interaction in a tungsten electrode starting from cold electrodes, did not matched the experimental observations when applied to a case of an arc during the separation of silver electrodes. Therefore, a further study of the NCPL model and its several parameters (secondary electron emission coefficient, field enhancement factor, among others) is necessary in order to be used in non-refractory materials typical of low voltage switching devices.

Another perspective for this thesis is the application of the developed model to study the influence of the metal vapors on the arc movement in a three-dimensional geometry. The contact separation case permitted to observed how the metallic vapors affected the arc temperature, its shape, as well as the heating of the electrodes. However, in this case the arc movement was restricted due to the geometrical characteristics and the axisymmetric condition. An interesting case of study for the future would be an arc that moves along parallel rails. In such a scenario, not only the impact of the metal presence in the arc can be observed, but also the influence that including the different combined diffusion coefficients has on the arc displacement.

As the calculations for the application case performed in this work were done under the assumption of local thermal equilibrium in the arc column, it will be interesting to evaluate the impact of this hypothesis by redetermining the properties in a non-equilibrium state and repeating the calculations without supposing an arc in local thermal equilibrium.

Finally, the arc-electrode description presented in this work should be optimized to be implemented in the comprehensive arc model that have been developed at Schneider Electric for industrial low voltage switching devices.

## REFERENCES


[1] L. van der Sluis, *Transients in power systems*. Chichester ; New York: Wiley, 2001.

[2] A. Fridman, Ed., *Transport phenomena in plasma*, 1. ed. in Advances in heat transfer, no. 40. Amsterdam: Elsevier, 2007.

[3] A. A. Fridman and L. A. Kennedy, *Plasma Physics and Engineering*, 2nd ed. Boca Raton, FL: CRC Press, 2011.

[4] *Thermal Plasmas: Fundamentals and Applications*. Cham: Springer International Publishing.

[5] M. Lisnyak, “Theoretical, numerical and experimental study of DC and AC electric arcs,” Apr. 2018, Accessed: Dec. 10, 2019. [Online]. Available: https://tel.archives-ouvertes.fr/tel-01808258

[6] M. I. Boulos, P. L. Fauchais, and E. Pfender, *Handbook of Thermal Plasmas*. Cham: Springer International Publishing, 2020. doi: 10.1007/978-3-319-12183-3.

[7] P. G. Slade, Ed., *Electrical contacts: principles and applications*, Second edition, First issued in paperback. Boca Raton London New York: CRC Press, Taylor & Francis Group, 2017.

[8] M. S. Benilov, “Understanding and modelling plasma–electrode interaction in high-pressure arc discharges: a review,” *J. Phys. D: Appl. Phys.*, vol. 41, no. 14, p. 144001, Jul. 2008, doi: 10.1088/0022-3727/41/14/144001.

[9] T. E. Browne Jnr, *Circuit Interruption: Theory and Techniques*. Boca Raton: Routledge, 2019.

[10] D. F. N. Santos, M. Lisnyak, N. A. Almeida, L. G. Benilova, and M. S. Benilov, “Numerical investigation of AC arc ignition on cold electrodes in atmospheric-pressure argon,” *J. Phys. D: Appl. Phys.*, vol. 54, no. 19, p. 195202, May 2021, doi: 10.1088/1361-6463/abdf97.

[11] D. F. N. Santos, N. A. Almeida, M. Lisnyak, J.-P. Gonnet, and M. S. Benilov, “Numerical investigation of regimes of current transfer to anodes of high-pressure arc discharges,” *Physics of Plasmas*, vol. 29, no. 4, p. 043503, Apr. 2022, doi: 10.1063/5.0076587.

[12] J. Wendelstorf, “Ab initio modelling of thermal plasma gas discharges (electric arcs),” Universitätsbibliothek Braunschweig, 2000. doi: 10.24355/DBBS.084-200511080100-74.

[13] G. Lister, J. Lawler, W. Lapatovich, and V. Godyak, “The physics of discharge lamps,” *Rev. Mod. Phys.*, vol. 76, no. 2, pp. 541–598, Jun. 2004, doi: 10.1103/RevModPhys.76.541.

[14] J. Heberlein, “New approaches in thermal plasma technology,” *Pure and Applied Chemistry*, vol. 74, no. 3, pp. 327–335, Jan. 2002, doi: 10.1351/pac200274030327.

[15] B. Boulet, G. Lalli, and M. Ajersch, “Modeling and control of an electric arc furnace,” in *Proceedings of the 2003 American Control Conference, 2003.*, Denver, CO, USA: IEEE, 2003, pp. 3060–3064. doi: 10.1109/ACC.2003.1243998.

[16] H.-J. Odenthal, A. Kemminger, F. Krause, L. Sankowski, N. Uebber, and N. Vogl, “Review on Modeling and Simulation of the Electric Arc Furnace (EAF),” *steel research int.*, vol. 89, no. 1, p. 1700098, Jan. 2018, doi: 10.1002/srin.201700098.

[17] A. B. Murphy, “The effects of metal vapour in arc welding,” *Journal of Physics D: Applied Physics*, vol. 43, no. 43, p. 434001, 2010, doi: 10.1088/0022-3727/43/43/434001.

[18] F. Wang, “Study of radiative properties : application to fast determination of temperature and iron concentration for MAG-P Arc (Ar-CO2-Fe mixtures) and to estimation of photobiological hazards for argon GTAW Arc,” PhD Thesis, Toulouse 3. [Online]. Available: http://www.theses.fr/2018TOU30121

[19] D. Shin, “A study of re-ignition phenomena and arc modelling to evaluate switching performance of low-voltage switching devices,” PhD Thesis, University of Southampton. [Online]. Available: https://eprints.soton.ac.uk/423475/

[20] “Private comunication.” Schneider Electric.

[21] B. Murphy, “Metal Vapour in Atmospheric-Pressure Arcs,” *IEEJ Trans. PE*, vol. 134, no. 3, pp. 199–202, 2014, doi: 10.1541/ieejpes.134.199.

[22] J. W. McBride and P. M. Weaver, “Review of arcing phenomena in low voltage current limiting circuitbreakers,” *IEE Proceedings - Science, Measurement and Technology*, vol. 148, no. 1, Art. no. 1, Jan. 2001, doi: 10.1049/ip-smt:20010185.

[23] B. Swierczynski, J. J. Gonzalez, P. Teulet, P. Freton, and A. Gleizes, “Advances in low-voltage circuit breaker modelling,” *J. Phys. D: Appl. Phys.*, vol. 37, no. 4, pp. 595–609, Feb. 2004, doi: 10.1088/0022-3727/37/4/011.

[24] M. Lindmayer, E. Marzahn, A. Mutzke, T. Ruther, and M. Springstubbe, “The process of arc splitting between metal plates in low voltage arc chutes,” *IEEE Transactions on Components and Packaging Technologies*, vol. 29, no. 2, pp. 310–317, Jun. 2006, doi: 10.1109/TCAPT.2006.875902.

[25] “01 - 84 ABB Review 3/2013.” Oct. 04, 2013. [Online]. Available: https://search.abb.com/library/Download.aspx?DocumentID=9AKK105713A9088&LanguageCode=en&DocumentPartId=&Action=Launch

[26] M. Rong, F. Yang, Y. Wu, A. B. Murphy, W. Wang, and J. Guo, “Simulation of Arc Characteristics in Miniature Circuit Breaker,” *IEEE Transactions on Plasma Science*, vol. 38, no. 9, pp. 2306–2311, Sep. 2010, doi: 10.1109/TPS.2010.2050703.

[27] C. Rumpler, H. Stammberger, and A. Zacharias, “Low-Voltage Arc Simulation with Out-Gassing Polymers,” in *2011 IEEE 57th Holm Conference on Electrical Contacts (Holm)*, Minneapolis, MN, USA: IEEE, Sep. 2011, pp. 1–8. doi: 10.1109/HOLM.2011.6034770.

[28] C. Ruempler, A. Zacharias, and H. Stammberger, “Low-voltage circuit breaker arc simulation including contact arm motion,” in *ICEC 2014; The 27th International Conference on Electrical Contacts*, Jun. 2014, pp. 1–5.

[29] L. Ghezzi and A. Balestrero, “Modeling and Simulation of Low Voltage Arcs,” 2010, Accessed: Oct. 22, 2020. [Online]. Available: https://repository.tudelft.nl/islandora/object/uuid%3Addf219d8-5572-45c5-9249-aacbb68683cd

[30] Wu Xi-xiu, Li Zhen-Biao, Tian Yun, Mao Wenjun, and Xie Xun, “Investigate on the simulation of black-box arc model,” in *2011 1st International Conference on Electric Power Equipment - Switching Technology*, Xi’an, China: IEEE, Oct. 2011, pp. 629–636. doi: 10.1109/ICEPE-ST.2011.6123163.

[31] M. Walter and C. Franck, “Improved Method for Direct Black-Box Arc Parameter Determination and Model Validation,” *IEEE Trans. Power Delivery*, vol. 29, no. 2, pp. 580–588, Apr. 2014, doi: 10.1109/TPWRD.2013.2283278.

[32] S.-W. Lim, U. A. Khan, J.-G. Lee, B.-W. Lee, K.-S. Kim, and C.-W. Gu, “Simulation analysis of DC arc in circuit breaker applying with conventional black box arc model,” in *2015 3rd International Conference on Electric Power Equipment – Switching Technology (ICEPE-ST)*, Busan: IEEE, Oct. 2015, pp. 332–336. doi: 10.1109/ICEPE-ST.2015.7368330.

[33] M. S. Benilov, “Modeling the physics of interaction of high-pressure arcs with their electrodes: advances and challenges,” *J. Phys. D: Appl. Phys.*, vol. 53, no. 1, p. 013002, Jan. 2020, doi: 10.1088/1361-6463/ab47be.

[34] “ANSYS Fluent Theory Guide.” Ansys Inc.

[35] M. F. Modest and S. Mazumder, *Radiative heat transfer*, Fourth edition. London: Academic Press, 2022.

[36] A. Gleizes, J. J. Gonzalez, and P. Freton, “Thermal plasma modelling,” *Journal of Physics D: Applied Physics*, vol. 38, no. 9, pp. R153–R183, 2005, doi: 10.1088/0022-3727/38/9/R01.

[37] F. Reichert, J.-J. Gonzalez, and P. Freton, “Modelling and simulation of radiative energy transfer in high-voltage circuit breakers,” *J. Phys. D: Appl. Phys.*, vol. 45, no. 37, p. 375201, Aug. 2012, doi: 10.1088/0022-3727/45/37/375201.

[38] U. S. Inan and M. Gołkowski, *Principles of plasma physics for engineers and scientists*. Cambridge ; New York: Cambridge University Press, 2011.

[39] Y. Cressault and A. Gleizes, “Thermal plasma properties for Ar–Al, Ar–Fe and Ar–Cu mixtures used in welding plasmas processes: I. Net emission coefficients at atmospheric pressure,” *J. Phys. D: Appl. Phys.*, vol. 46, no. 41, p. 415206, Oct. 2013, doi: 10.1088/0022-3727/46/41/415206.

[40] Y. Cressault, A. B. Murphy, P. Teulet, A. Gleizes, and M. Schnick, “Thermal plasma properties for Ar–Cu, Ar–Fe and Ar–Al mixtures used in welding plasmas processes: II. Transport coefficients at atmospheric pressure,” *J. Phys. D: Appl. Phys.*, vol. 46, no. 41, p. 415207, Oct. 2013, doi: 10.1088/0022-3727/46/41/415207.

[41] Y. Cressault, “Basic knowledge on radiative and transport properties to begin in thermal plasmas modelling,” *AIP Advances*, vol. 5, no. 5, p. 057112, May 2015, doi: 10.1063/1.4920939.

[42] P. Tolias and the Euro. M. Team, “Analytical expressions for thermophysical properties of solid and liquid tungsten relevant for fusion applications,” *Nuclear Materials and Energy*, vol. 13, pp. 42–57, Dec. 2017, doi: 10.1016/j.nme.2017.08.002.

[43] “Ansys Granta Selector.”

[44] C. Bonacina, G. Comini, A. Fasano, and M. Primicerio, “Numerical solution of phase-change problems,” *International Journal of Heat and Mass Transfer*, vol. 16, no. 10, pp. 1825–1832, Oct. 1973, doi: 10.1016/0017-9310(73)90202-0.

[45] Y. A. Mayi *et al.*, “Laser-induced plume investigated by finite element modelling and scaling of particle entrainment in laser powder bed fusion,” *J. Phys. D: Appl. Phys.*, vol. 53, no. 7, p. 075306, Feb. 2020, doi: 10.1088/1361-6463/ab5900.

[46] M. Lisnyak, M. D. Cunha, J.-M. Bauchire, and M. S. Benilov, “Numerical modelling of high-pressure arc discharges: matching the LTE arc core with the electrodes,” *J. Phys. D: Appl. Phys.*, vol. 50, no. 31, p. 315203, Jul. 2017, doi: 10.1088/1361-6463/aa76d3.

[47] J. L. Zhang, J. D. Yan, and M. T. C. Fang, “Electrode evaporation and its effects on thermal arc behavior,” *IEEE Transactions on Plasma Science*, vol. 32, no. 3, pp. 1352–1361, Jun. 2004, doi: 10.1109/TPS.2004.827606.

[48] M. Rong, Q. Ma, Y. Wu, T. Xu, and A. B. Murphy, “The influence of electrode erosion on the air arc in a low-voltage circuit breaker,” *Journal of Applied Physics*, vol. 106, no. 2, p. 023308, Jul. 2009, doi: 10.1063/1.3176983.

[49] Y. Yokomizu, T. Matsumura, R. Henmi, and Y. Kito, “Total voltage drops in electrode fall regions of , argon and air arcs in current range from 10 to 20 000 A,” *J. Phys. D: Appl. Phys.*, vol. 29, no. 5, pp. 1260–1267, May 1996, doi: 10.1088/0022-3727/29/5/020.

[50] J. Huo, S. Selezneva, L. Jacobs, and Y. Cao, “Study of wall ablation on low-voltage arc interruption: The effect of Stefan flow,” *Journal of Applied Physics*, vol. 125, no. 21, p. 213302, Jun. 2019, doi: 10.1063/1.5090867.

[51] J. J. Lowke, R. Morrow, and J. Haidar, “A simplified unified theory of arcs and their electrodes,” *Journal of Physics D: Applied Physics*, vol. 30, no. 14, pp. 2033–2042, 1997, doi: 10.1088/0022-3727/30/14/011.

[52] F. Cayla, “Modélisation de l’interaction entre un arc électrique et une cathode,” These de doctorat, Toulouse 3, 2008. Accessed: Apr. 21, 2022. [Online]. Available: https://www.theses.fr/2008TOU30033

[53] M. S. Benilov, “NCPL - On-line tool for evaluation of parameters of non-equilibrium near-cathode plasma layer in high-pressure arc plasmas.” Jul. 22, 2021. [Online]. Available: http://fisica.uma.pt/public/NCPL

[54] M. S. Benilov, M. D. Cunha, and G. V. Naidis, “Modelling interaction of multispecies plasmas with thermionic cathodes,” *Plasma Sources Science and Technology*, vol. 14, no. 3, pp. 517–524, 2005, doi: 10.1088/0963-0252/14/3/014.

[55] N. K. Mitrofanov and S. M. Shkol’nik, “Two forms of attachment of an atmospheric-pressure direct-current arc in argon to a thermionic cathode,” *Tech. Phys.*, vol. 52, no. 6, pp. 711–720, Jun. 2007, doi: 10.1134/S1063784207060060.

[56] M. D. Cunha, H. T. C. Kaufmann, D. F. N. Santos, and M. S. Benilov, “Simulating changes in shape of thermionic cathodes during operation of high-pressure arc discharges,” *J. Phys. D: Appl. Phys.*, vol. 52, no. 50, p. 504004, Dec. 2019, doi: 10.1088/1361-6463/ab4510.

[57] K. Takaki, D. Taguchi, and T. Fujiwara, “Voltage–current characteristics of high-current glow discharges,” *Applied Physics Letters*, vol. 78, no. 18, pp. 2646–2648, Apr. 2001, doi: 10.1063/1.1369612.

[58] M. Baeva, M. S. Benilov, N. A. Almeida, and D. Uhrlandt, “Novel non-equilibrium modelling of a DC electric arc in argon,” *J. Phys. D: Appl. Phys.*, vol. 49, no. 24, p. 245205, Jun. 2016, doi: 10.1088/0022-3727/49/24/245205.

[59] C. Mohsni, M. Baeva, St. Franke, S. Gortschakow, Z. Araoud, and K. Charrada, “Effect of a bidirectional coupling of an LTE arc column to a refractory cathode in atmospheric pressure argon,” *Physics of Plasmas*, vol. 27, no. 7, p. 073514, Jul. 2020, doi: 10.1063/5.0013397.

[60] F. Lago, J. J. Gonzalez, P. Freton, and A. Gleizes, “A numerical modelling of an electric arc and its interaction with the anode: Part I. The two-dimensional model,” *Journal of Physics D: Applied Physics*, vol. 37, no. 6, pp. 883–897, 2004, doi: 10.1088/0022-3727/37/6/013.

[61] M. Schnick, U. Fuessel, M. Hertel, M. Haessler, A. Spille-Kohoff, and A. B. Murphy, “Modelling of gas–metal arc welding taking into account metal vapour,” *Journal of Physics D: Applied Physics*, vol. 43, no. 43, p. 434008, 2010, doi: 10.1088/0022-3727/43/43/434008.

[62] M. Schnick, U. Füssel, M. Hertel, A. Spille-Kohoff, and A. B. Murphy, “Metal vapour causes a central minimum in arc temperature in gas–metal arc welding through increased radiative emission,” *Journal of Physics D: Applied Physics*, vol. 43, no. 2, p. 022001, 2010, doi: 10.1088/0022-3727/43/2/022001.

[63] A. B. Murphy, “Influence of metal vapour on arc temperatures in gas–metal arc welding: convection versus radiation,” *Journal of Physics D: Applied Physics*, vol. 46, no. 22, p. 224004, 2013, doi: 10.1088/0022-3727/46/22/224004.

[64] M. Tanaka *et al.*, “Time-dependent calculations of molten pool formation and thermal plasma with metal vapour in gas tungsten arc welding,” *J. Phys. D: Appl. Phys.*, vol. 43, no. 43, p. 434009, Nov. 2010, doi: 10.1088/0022-3727/43/43/434009.

[65] M. Baeva *et al.*, “Unified modelling of low-current short-length arcs between copper electrodes,” *J. Phys. D: Appl. Phys.*, vol. 54, no. 2, p. 025203, Jan. 2021, doi: 10.1088/1361-6463/abba5d.

[66] P. Freton, J.-J. Gonzalez, A. Harry Solo, F. Reichert, and A. Petchanka, “Influence of Copper Vapors in SF6 Plasma,” *PLASMA PHYSICS AND TECHNOLOGY*, vol. 6, no. 2, pp. 161–164, 2019, doi: 10.14311/ppt.2019.2.161.

[67] P. Freton, J. Gonzalez, F. Reichert, and A. Petchanka, “Proposition for a cu/w ablation model for hvcb electrodes.”.

[68] Y. Mayi *et al.*, “Two-Phase Flow Modelling of Metal Vaporisation under Static Laser Shot using a Double Domain ALE Method - A Feasibility Study,” 2018.

[69] A. Marotta and L. I. Sharakhovsky, “A theoretical and experimental investigation of copper electrode erosion in electric arc heaters: I. The thermophysical model,” *Journal of Physics D: Applied Physics*, vol. 29, no. 9, pp. 2395–2403, 1996, doi: 10.1088/0022-3727/29/9/025.

[70] M. Li, Y. Wu, Y. Wu, and D. Zhao, “Experimental and theoretical investigation on radiation loss for a fault arc between different material electrodes in an enclosed air tank,” *J. Phys. D: Appl. Phys.*, vol. 50, no. 48, p. 485205, Dec. 2017, doi: 10.1088/1361-6463/aa90f8.

[71] A. B. Murphy, “Diffusion in equilibrium mixtures of ionized gases,” *Phys. Rev. E*, vol. 48, no. 5, pp. 3594–3603, Nov. 1993, doi: 10.1103/PhysRevE.48.3594.

[72] A. B. Murphy, “Calculation and application of combined diffusion coefficients in thermal plasmas,” *Scientific reports*, vol. 4, p. 4304, 2014, doi: 10.1038/srep04304.

[73] Y. Cressault and A. Gleizes, “Calculation of diffusion coefficients in air–metal thermal plasmas,” *J. Phys. D: Appl. Phys.*, vol. 43, no. 43, p. 434006, Nov. 2010, doi: 10.1088/0022-3727/43/43/434006.

[74] A. B. Murphy and C. J. Arundell, “Transport coefficients of argon, nitrogen, oxygen, argon-nitrogen, and argon-oxygen plasmas,” *Plasma Chem Plasma Process*, vol. 14, no. 4, pp. 451–490, Dec. 1994, doi: 10.1007/BF01570207.

[75] M. Shibayama, Y. Tanaka, Y. Nakano, and T. Ishijima, “Numerical study of polymer-ablation arc with polyacrylic acid + H 2 O mixture,” *Journal of Physics D: Applied Physics*, vol. 54, no. 14, p. 145203, 2021, doi: 10.1088/1361-6463/abd506.

[76] J. Barrett and C. Clement, “Kinetic evaporation and condensation rates and their coefficients,” *Journal of Colloid and Interface Science*, vol. 150, no. 2, pp. 352–364, 1992, doi: 10.1016/0021-9797(92)90205-Z.

[77] A. Gleizes and Y. Cressault, “Effect of Metal Vapours on the Radiation Properties of Thermal Plasmas,” *Plasma Chem Plasma Process*, vol. 37, no. 3, pp. 581–600, May 2017, doi: 10.1007/s11090-016-9761-y.

[78] Y. Cressault, R. Hannachi, P. Teulet, A. Gleizes, J.-P. Gonnet, and J.-Y. Battandier, “Influence of metallic vapours on the properties of air thermal plasmas,” *Plasma Sources Sci. Technol.*, vol. 17, no. 3, p. 035016, Aug. 2008, doi: 10.1088/0963-0252/17/3/035016.

[79] A. Gleizes, Y. Cressault, and P. Teulet, “Mixing rules for thermal plasma properties in mixtures of argon, air and metallic vapours,” *Plasma Sources Science and Technology*, vol. 19, no. 5, p. 055013, 2010, doi: 10.1088/0963-0252/19/5/055013.

[80] Y. Tanaka and T. Iijima, “Hybrid Thermofluid Simulation with Chemically Non-Equilibrium and Equilibrium Calculations for Decaying $SF_6$ Arcs,” in *2019 5th International Conference*

*on Electric Power Equipment - Switching Technology (ICEPE-ST)*, Kitakyushu, Japan: IEEE, Oct. 2019, pp. 1–6. doi: 10.1109/ICEPE-ST.2019.8928744.

[81] P. G. Slade, “Opening Electrical Contacts: The Transition from the Molten Metal Bridge to the Electric Arc,” *IEICE Trans. Electron.*, vol. E93.C, no. 9, pp. 1380–1386, 2010, doi: 10.1587/transele.E93.C.1380.

[82] M. Lindmayer, “Remarks Concerning Arc Roots in CFD Modeling of Switching Arcs,” *30th International Conference on Electrical Contacts Conference Proceedings (ICEC 2020)*, Jun. 2021, doi: 10.5281/zenodo.4917121.

[83] S. V. Patankar, *Numerical Heat Transfer and Fluid Flow*, 1st ed. CRC Press, 2018. doi: 10.1201/9781482234213.